Nonextensive Statistics Approach to Anomalous Diffusion in Plasmas: Applications and Scaling to Other Models

by

Bradley R. Andrew

A dissertation submitted to the Graduate Faculty of
Auburn University
in partial fulfillment of the
requirements for the Degree of
Doctor of Philosophy

Auburn, Alabama
August 9, 2025

Keywords: plasma physics, dusty plasma, nonextensive statistics, anomalous diffusion, fractional Laplacian, magnetic islands

Approved by

E. G. Kostadinova, Chair, Assistant Professor of Physics
Hong Zhao, Assistant Professor of Physics
Eric Burkholder, Assistant Professor of Physics
Raphael Bernardi, Associate Professor of Physics
Selim Sukhtaiev, University Reader, Assistant Professor of Mathematics
George Flowers, Dean of the Graduate School

Abstract

Plasmas, known for their multiscale physics phenomena and rich dynamics, often exhibit anomalous diffusion that deviate from classical models, challenging the assumptions of locality, linearity, and Gaussianity. This dissertation investigates anomalous diffusion in two distinct plasma regimes—microgravity dusty plasmas and magnetically confined fusion plasmas—through the unified lens of nonextensive statistics and fractional spectral models. We first establish formal connections between nonextensive statistical mechanics and fractional derivative operators, showing how q-Gaussian distribution functions relate to Lévy flights and how the nonextensive index q maps to the fractional Laplacian exponent s. These scaling relations are used to connect a spectral transport model based on an Anderson-type Hamiltonian with a fractional Laplacian to the nonextensive statistical behavior often observed in complex systems, such as plasmas.

The nonextensive framework is first applied to video data from the PK-4 dusty plasma experiment aboard the International Space Station. The PK-4 experiment uses video cameras to track individual dust particles suspended in low temperature plasma, which allows the collection of large amounts of statistical information on the dust particle positions and velocities. These statistics are used to study anomalous dust diffusion caused by anisotropies in the plasma-mediated dust-dust interactions in PK-4. Using q-Gaussian fits to histograms of particle displacements and velocities, we define an anisotropic kinetic temperature and identify inverse correlations between the nonextensive parameter q and local diffusivity, thus quantifying deviations from thermal equilibrium. A spatial disorder metric and analysis of particle jumps are further used to identify microscopic processes contributing to the observed anisotropic anomalous diffusion of the dust particles.

To further understand how the interplay between nonlocality and stochasticity leads to different regimes of anomalous diffusion, we introduce a Fractional Laplacian Spectral Method (FLSM) that calculates probability for diffusive transport at different scales in Hilbert space from the spectrum of the discrete random fractional Schrödinger operator. We perform a large-scale parameter sweep across 55,000 realizations of the operator that represent different combinations of nonlocality, stochastic disorder and Hilbert space vector scales, including all combinations of parameters extracted from PK-4 data using scaling relations. The spectral simulations reveal "islands of enhanced transport" in Hilbert space—regions where transport is amplified due to constructive interplay between nonlocality and stochasticity. We compare the predictions from the spectral model to the dust dynamics observed in the PK-4 experiments.

Finally, nonextensive statistics the framework is applied to simulations of magnetic island topology in the NSTX-U tokamak. Of specific interest are cases where the island structure undergoes successive bifurcations under the action of coil perturbations. The reconstruction of magnetic field line diffusion in NSTX-U is used to understand how changes in magnetic topology will alter electron diffusion in magnetized plasmas. By treating the normalized poloidal magnetic field flux Ψ_N as a statistical distribution, we extract non-Gaussian signatures via q-Gaussian fits to histograms of magnetic field line displacements and apply a spatial KD-tree disorder metric to quantify field-line divergence. Both metrics increase monotonically with applied perturbation coil current, tracing the emergence of bifurcations, stochasticity, and topological complexity in the magnetic geometry. We find that increasing the perturbation leads to a crossover from subdiffusion, to classical diffusion, followed by superdiffusion, and eventually, Lévy flights. These measures provide potential tools for diagnosing magnetic field instability and precursor activity for plasma instabilities and disruptions in fusion devices. Together, the investigations presented here offer a unified statistical-spectral approach to modeling anomalous diffusion in plasmas.

Acknowledgments

To Alexis and Lily whom I love dearly,
and are my greatest blessing from The LORD.

Soli Deo Gloria

This material is based on work supported by NSF grant numbers 2308742, 2308743, 2440328, EPSCoR FTPP OIA2148653, 1903450, and 1740203, NASA grant number 80NSSC21K0381, DOE grant numbers DE-SC0023061, DE-SC0023476. All authors gratefully acknowledge the joint ESA - Roscosmos "Experiment Plasmakristall-4" onboard the International Space Station.

We acknowledge the Auburn University Easley Cluster for support of this work.

I would like to sincerely thank my advisor, Evdokiya Kostadinova, for her guidance and inspiration throughout this research, and all those who are part of the IPL team for their support. I also gratefully acknowledge Dmitri Orlov, Lorin Matthews, Truell Hyde, Luca Guazzotto, and Eric Howell for their contributions as collaborators. Special thanks as well to the DIII-D team and the MPRL team.

Table of Contents

List of Figures

List of Tables

Chapter 1

Introduction

1.1 Background

Plasma, often referred to as the fourth state of matter, represents the majority of the visible universe and is fundamental to understanding a wide range of natural and laboratory systems—from stellar atmospheres and solar winds to fusion devices and dusty plasma experiments. Characterized by collective behavior, long-range electromagnetic interactions, and complex nonlinear dynamics, plasmas present unique challenges in understanding transport processes. Unlike simple fluids or gases, plasmas often exist far from thermodynamic equilibrium, exhibiting fluctuations and structures across many scales, both spatial and temporal.

In such conditions, transport in plasma systems frequently defies the assumptions of classical diffusion theory. Rather than following Gaussian statistics and simple Brownian motion, particle motion in many plasmas exhibits *anomalous diffusion*, or a process where the mean squared displacement (MSD) of the particles scales nonlinearly with time. This nonclassical behavior has been observed across a wide range of plasma environments, including magnetically confined fusion plasmas, astrophysical plasmas, and complex (or dusty) plasmas. Traditional kinetic theories, particularly those rooted in Boltzmann-Gibbs statistics, struggle to capture anomalous diffusion, as they rely on assumptions of locality, short-range interactions, and equilibrium conditions. Despite its many limitations, classical statistics are still the traditional baseline of kinetic theories for plasmas.

Both experimental and simulation studies have highlighted the presence and importance of long-range correlations, memory effects, and heavy-tailed velocity and step-size

distributions—hallmarks of non-Gaussianity and non-locality, often linked to anomalous diffusion. These characteristics suggest the need for theoretical frameworks that extend beyond Boltzmann models of classical kinetics. In response, this dissertation aims to promote nonextensive statistical mechanics, particularly the framework introduced by Tsallis [2], as a more accurate and physically meaningful approach for describing anomalous diffusion in plasmas. By generalizing entropy and modifying assumptions of statistical independence, nonextensive statistics provides a basis for modeling systems with multiscale dynamics, memory effects, and strong coupling—features commonly found in turbulent and instability-dominated plasma regimes.

An equally critical, yet underutilized, lens is the spectral approach to diffusive transport, which investigates how microscopic processes (such as nonlocality and stochasticity) yield changes in global dynamics and stability. Spectral methods study the spectra of operators in Hilbert space using the tools of linear algebra. While agnostic to the physical system, these methods are standard to condensed matter physics, but very rare in plasma physics. The spectral approach used here, first introduced by Liaw [3] , is focused on the energy spectrum of Hamiltonian operators, specifically studying the existence of continuous spectrum leading to energy mixing and extended states. The existence of continuous spectrum is key in understanding complex phenomena, such as turbulence, energy cascades, and structure formation, thereby illuminating the mechanisms that drive deviations from classical transport laws. Here we argue that when paired with statistical tools, the spectral approach can enable the identification of scaling laws and anomalous diffusion regimes across different plasma systems.

A further goal of this dissertation is to discuss and test scaling relations that provide connections across multiple frameworks, namely nonextensive statistics, nonlinear diffusion equations, fractional derivative operators, and spectral methods, thus offering a comprehensive overview of tools that can be used to investigate anomalous diffusion in plasmas. As these frameworks have often been developed in isolation, their integration and application to

real plasma systems remains an open and promising area of research. The results presented here aim to advance the understanding of anomalous diffusion in plasmas and demonstrate the value of unified statistical-spectral frameworks in modern plasma physics.

1.2 Objectives and Contributions

This dissertation aims to promote better utilization of nonextensive statistics as applied to anomalous diffusion in plasma physics, while also bridging it to the spectral approach. Both frameworks are first used to analyze anomalous dust diffusion in dusty plasma experiments and test cross-model scaling relations proposed in literature. Then, nonextensive statistics is applied to simulations of magnetized plasma to investigate anomalous diffusion of magnetic field lines during magnetic island bifurcations. The main contributions of the present work are summarized below.

Theoretical Framework: We summarize scaling relations proposed in literature that aim to provide connection between nonextensive q-statistics, non-linear diffusion equations, fractional diffusion models, and Lévy flights. Specifically, we discuss how each scaling relation was derived and what assumptions are needed for validity. In several cases, we identify new scaling relations by overlapping ranges of validity for two or more models. These results allow for scaling of parameters from probabilistic transport theory to spectral operator theory.

Statistical and Diffusion Analysis of Dusty Plasma: We analyze data from the PK-4 microgravity experiments where micron-sized spherical particles were suspended in low temperature DC plasma discharge with the help of a polarity switched external electric field. Dust particle trajectories are used to calculate various statistical parameters, including histograms of displacements and velocties, mean squared displacements, and autocorrelation functions for different background plasma conditions. Tsallis q-Gaussian fits to the histograms are used to obtain the corresponding distribution functions and assess the diffusion regime for each experiment. Directional anisotropies in the diffusion properties (such as diffusion coefficient and kinetic temperature) are identified and quantified. We propose that

these effects can be linked to the external electric field which causes anisotropies on the ion-wakefield-mediated dust-dust interaction potential. Our analysis provides experimentally measurable way to study how changes in the microscopic ion dynamics affect the dust diffusion, thus keeping the dust cloud ensemble in a nonequilibrium state.

Disorder and Step-Size Scaling in Dusty Plasma: We introduce a spatial disorder metric to assess the role of stochastic fluctuations in the dust particle positions. We also develop a classification of dust displacements (or step-wise jumps) into "mean jumps", "large jumps", and "clusters of large jumps" categories. Clusters of large jumps are shown to drive superdiffusive transport and correlate with higher disorder regions. Based on this analysis, we conjecture that the combination of stochastic disorder and rare nonlocal events drive anomalous diffusion in dusty plasma experiments. These behaviors are interpreted as manifestations of Lévy flight–type dynamics within a bounded domain.

Fractional Laplacian Spectral Method (FLSM): The FLSM works with Hamiltonian operators that model nonlocal effects (via a fractional Laplacian kinetic term) and stochasticity (via random disorder potential term). Of special interest is the existence of continuous energy spectrum, which suggests energy mixing and transport. A large-scale parameter sweep FLSM calculation was performed to study the energy spectrum resulting from 55,000 combinations of fractional exponent s, random disorder c, and reference scale ν in Hilbert space. The resulting spectral plots reveal both expected and unexpected results such as "islands of transport" in at certain reference scales of Hilbert space. We interpret these islands as constructive combinations of nonlocality and stochasticity that will yield enhanced transport at key spatial scales.

Magnetic Island Complexity and Fusion Plasmas: Simulations of the NSTX-U tokamak using the M3D-C1 code with applied 3D coil current perturbations are analyzed statistically. The normalized poloidal magnetic field flux Ψ_N is used to reconstruct the topology of magnetic field lines in the poloidal plane and identify regions of magnetic islands. Histograms of magnetic field displacements are constructed for different values of the coil

current perturbation. The histograms are fitted with q_p-Gaussians to capture the field line diffusion regime in each case. A KD-tree–based spatial disorder metric is applied to field-line trajectories to assess the role of stochasticity as the increasing perturbation cases the magnetic islands to bifurcate. Both the nonextensive parameter q and the stochasticity increase monotonically with perturbation current, tracking the onset of island bifurcation, sub-structure formation, and stochastization of magnetic surfaces. The analysis reveals that increasing coil current causes a crossover from subdiffusion, to classical diffusion, followed by superdiffusion, and eventually a Lévy process for the magnetic field lines. Since electrons in the NSTX-U tokamak (and other fusion devices) are highly magnetized, it is expected that the observed changes in the field line diffusion will have measurable impact on the corresponding electron cross-field diffusion. We propose that the statistical tools developed here can be used as diagnostics for the onset of topological instability instability of the magnetic field, which is a precursor of plasma instability and disruptions in fusion devices.

1.3 **Organization of the Dissertation**

The remainder of the dissertation is organized as follows. Chapter 2 introduces the mathematical foundation of anomalous diffusion models, including nonextensive statistics, fractional Laplacians, and cross-model scaling relations. Chapter 3 reviews existing literature on q-statistics and anomalous diffusion, with a focus on plasma applications and theoretical robustness. Chapter 4 analyzes PK-4 data using q-Gaussians statistics to quantify nonequilibrium effects and anisotropic anomalous diffusion. Chapter 5 introduces disorder metrics and analyzes step-size clustering, with implications for Lévy flight dynamics and scale-resolved transport and introduces the FLSM framework. Chapter 5 also applies FLSM to parameter spaces informed from PK-4 experiments, thus connecting spectral results to PK-4 statistical analysis. Chapter 6 extends the statistical analysis to NSTX-U simulations, demonstrating how the model can be used to study anomalous diffusion of magnetic field

lines in magnetized plasma. Chapter 7 concludes the dissertation with a summary of results, a discussion of limitations, and suggested avenues for future research.

Chapter 2

Analytical Approaches to Anomalous Diffusion

2.1 Diffusion

In the absence of long-range interactions or correlations, the particle diffusion can be described by Brownian motion and the model differential equation is the well-known diffusion equation

$$\frac{\partial p(x,t)}{\partial t} = \Delta(Dp(x,t)), \tag{2.1.1}$$

where $\Delta = \frac{\partial^2}{\partial x^2}$ is the Laplacian operator, D is the diffusion constant, and $p(x,t)$ is the distribution function. Equation (2.1.1) is also the linear Fokker-Planck equation with no drift. The one-dimensional solution to the diffusion equation has a Gaussion distribution functional form given by

$$p(x,t) = \frac{1}{\sqrt{4\pi Dt}} e^{-\frac{(x-x_0)^2}{4Dt}}. \tag{2.1.2}$$

The mean squared displacement (MSD) is the second moment of this equation

$$\langle (x-x_0)^2 \rangle \equiv \int (x-x_0)^2 p(x,t) dx = 2Dt. \tag{2.1.3}$$

As can be seen, the classical diffusion equation yields MSD that grows linearly with time. Assuming discrete particle positions, the MSD expression for N particles can be generalized in two or three dimensions to

$$\langle |r(t) - r_{t=0}|^2 \rangle = \frac{1}{N} \sum_{i=1}^{N} |r^{(i)}(t) - r^{(i)}(t=0)|^2 = 2dDt \tag{2.1.4}$$

where d is the spatial dimension. This can be further generalized using a time delay τ to

$$\langle |r(t+\tau) - r_{t=0}|^2 \rangle = \frac{1}{N} \sum_{i=1}^{N} |r^{(i)}(t+\tau) - r^{(i)}(t=0)|^2 = 2dD\tau^{\alpha} \quad \alpha \geq 0, \tag{2.1.5}$$

where α is an exponent that quantifies deviations from a linear dependence in time (i.e., the presence of anomalous diffusion). When $\alpha = 1$ (linear MSD), the diffusion is classical, while $\alpha \neq 1$ implies anomalous diffusion. While anomalous diffusion is ubiquitous in nature [4, 5, 6, 7, 8, 9], its mathematical description is challenging and requires different mathematical models than Eq. 2.1.1.

One way to study anomalous diffusion is with the nonlinear version of the Fokker-Planck diffusion equation, which leads to solutions such as the Barenblatt solution (see page 249 of [10]) and the Tsallis q-Gaussian distributions [2] (also known as Kappa distributions or Student's t distributions). Anomalous diffusion can also be studied using fractional version of the Laplace operator [11, 12] which can lead to solutions such as Lévy distributions. We note that it is not well understood if universal scaling relations exist that link the different analytical formulations used to model anomalous diffusion. There are some direct scaling relations between the nonlinear exponents in the Fokker-Planck equation and the nonextensive q parameter in the q-Gaussian solutions. However, scaling relations between nonlinear exponents and exponents on the fractional Laplace operator are not straightforward, even though both frameworks aim to describe similar regimes of anomalous diffusion. One goal of this dissertation work is to provide further clarity on the validity of such scaling relations for different anomalous diffusion regimes. We start by discussing the connection between nonlinear diffusion equations and Tsallis' nonextensive statistics.

2.2 Connecting Nonlinear Diffusion to Tsallis' Nonextensive Statistics

We start with a nonlinear diffusion equation, specifically, the nonlinear Fokker-Planck equation with no drift

$$\frac{\partial p(x,t)}{\partial t} = D\frac{\partial^2 [p(x,t)]^\nu}{\partial x^2}, \tag{2.2.1}$$

where the exponent ν makes the equation nonlinear. This equation is sometimes referred to as the porous medium equation. Eq. 2.2.1 has the following explicit solution derived under the assumption of self-similarity and mass conservation, and typically corresponds to the so-called Barenblatt–Pattle solution of the porous medium equations known to be unique within the family of self-similar spreading profiles for given initial conditions and exponent ν [13, **?**] and also given in [10] page 249

$$p(x,t) = A_\nu^{-1}\left[2D(\nu+\nu^2)(t-t_0)\right]^{\frac{-1}{1+\nu}} \cdot \left[1 + \frac{(1-\nu)(x-x_0)^2}{\left((2D(\nu+\nu^2)(t-t_0)A_\nu^{1-\nu})^{\frac{2}{1+\nu}}\right)}\right]^{\frac{-1}{1-\nu}}, \tag{2.2.2}$$

where A_ν^{-1} is a normalization factor dependent on ν. This form assumes an initially localized distribution with compact support and no-flux boundary conditions at infinity. The derivation often involves a similarity transformation that reduces the nonlinear partial differential equation to an ordinary differential equation. This solution can be rewritten using Tsallis's nonextensive q parameter using the scaling relation $\nu \equiv 2 - q$ introduced in [2]

$$p(x,t) = A_q^{-1}\left[2D(6-5q+q^2)(t-t_0)\right]^{\frac{-1}{3-q}} \cdot \left[1 + \frac{(q-1)(x-x_0)^2}{\left((2D(6-5q+q^2)(t-t_0)A_q^{q-1})^{\frac{2}{3-q}}\right)}\right]^{\frac{-1}{q-1}} \tag{2.2.3}$$

where A_q is a normalization factor given by

$$A_q = \begin{cases} \sqrt{\frac{\pi}{(1-q)}}\frac{\Gamma(\frac{2-q}{1-q})}{\Gamma(\frac{q}{2-2q})} & \text{if } q < 1 \\ \sqrt{\pi} & \text{if } q = 1 \\ \sqrt{\frac{\pi}{(q-1)}}\frac{\Gamma(\frac{3-q}{2q-2})}{\Gamma(\frac{q}{q-1})} & \text{if } 1 < q < 3. \end{cases} \tag{2.2.4}$$

The probability distribution function in equation 2.2.3 is called the q-Gaussian. When $q = 1$ and $t_0 = 0$ this solution becomes equation 2.1.2. The parameter q can also be related to the distribution kurtosis κ, through the following relationship: $\kappa = \frac{15-9q}{7-5q}$, for $q < 7/5$ [14] where $\kappa = \frac{\langle x^4 \rangle}{\langle x^2 \rangle^2}$. Here we use the standard notation $\langle x^n \rangle$ to be the n^{th} moment of the probability distribution. The parameters ν, q, and κ can be used to quantify the deviations from a Gaussian distribution and the related anomalous diffusion (e.g., as discussed in [15]). The primary interest of the present work is the range $-1 < q < 3$, though mathematically the entire range is $-\infty < q < 3$. For $1 < q < 3$ the distributions exhibit leptokurtic or 'fat-tail' behavior. This regime is also where anomalous diffusion is superdiffusive (and the MSD exponent $\alpha > 1$). For $-\infty < q < 1$ the distributions exhibit platykurtic or 'flat peaks' and weak tails. This regime corresponds to subdiffusion where the MSD exponent $\alpha < 1$ (see Figure 2.1 for example distributions representing each regime). The scaling relation between q and α can be obtained by taking the second moment of Eq. 2.2.2, which yields a non-linear relation between the MSD and time

$$\langle (x - x_0)^2 \rangle = B_q (D\tau)^{\frac{2}{3-q}}, \quad \tau = t - t_0 \tag{2.2.5}$$

where

$$B_q = \frac{2^{\frac{1-q}{q-3}} \pi^{\frac{3(1-q)}{2(q-3)}} (q-1)^{\frac{q}{2(q-3)}} \Gamma\left(\frac{4-3q}{2q-2}\right)}{(q-3)^{\frac{2}{q-3}} (q-2)^{\frac{2}{q-3}} \Gamma\left(\frac{1}{q-1}\right) \left(\frac{\Gamma\left(\frac{2-q}{2q-2}\right)}{\Gamma\left(\frac{q}{q-1}\right)}\right)^{\frac{4q-6}{q-3}}}. \tag{2.2.6}$$

Comparison of equation 2.2.5 and 2.1.5 yields the scaling relation $\alpha = 2/(3-q)$. While this shows us how nonextensive statistics can be linked to solutions of nonlinear diffusion equations, nonextensive statistics is a much richer theory.

Nonextensive statistics was proposed by Tsallis initially in [16] and is fully described in his textbook [2]. Nonextensive entropy is a generalization of Boltzmann–Gibbs entropy that incorporates long-range interactions, memory effects, or fractal space-time constraints. It is defined using the q-logarithm, where the parameter q quantifies the degree of nonextensivity in the system:

$$S_q = k_B \frac{1 - \sum_{i=1}^{W} p_i^q}{q - 1}. \tag{2.2.7}$$

In the special case where all W microstates are equally probable (i.e., $p_i = 1/\Omega$ for all i), this expression reduces to

$$S_q = k_B \ln_q(\Omega) = k_B \frac{\Omega^{1-q} - 1}{1 - q}, \tag{2.2.8}$$

where Ω is the total number of accessible microstates. This entropy is nonadditive when $q \neq 1$, meaning that $S_q(A + B) \neq S_q(A) + S_q$ (B). Instead, $S_q(A + B) = S_q(A) + S_q(B) + (1 - q)S_q(A)S_q(B)$. In the case $q > 1$, this system is called subadditive since $S_q(A + B) \leq S_q(A) + S_q(B)$. The motivation for this theory stems from the fact that the thermodynamic limit within Boltzmann statistics does not seem to work in a system of particles interacting via long-range forces, which makes the statistical description of plasmas challenging. This is especially challenging for low-temperature plasmas or complex plasmas, such as a dusty plasma. To see this mathematically, consider integrating a potential energy of the form

$$U(r) = -\frac{A}{r^{\xi}}, \quad A > 0; \ \xi \geq 0, \tag{2.2.9}$$

where ξ determines the range of the interactions. Finding the total potential energy per N number of particles in d dimensions can be obtained by integration

$$U(N)/N \propto A \int_1^{N^{\frac{1}{d}}} \frac{1}{r^{\xi}} r^{d-1} dr. \tag{2.2.10}$$

Then, in the limit as the number of particles increases $N \to \infty$

$$\lim_{N\to\infty} \frac{U(N)}{N} \to \begin{cases} -\frac{A}{\xi - d} & \text{if } \frac{\xi}{d} > 1 \\ ln(N) \to \infty & \text{if } \frac{\xi}{d} = 1 \\ \frac{N^{1-\frac{\xi}{d}}}{1-\frac{\xi}{d}} \to \infty & \text{if } 0 < \frac{\xi}{d} < 1. \end{cases} \tag{2.2.11}$$

The term $\frac{\xi}{d}$ is called the microscopic ratio and is greater or equal to 1 for short range potentials, such as the Lennard-Jones potential ($\xi = 6$) in $3D$ space. Also, in the case where $\frac{\xi}{d} > 1$, the potential depends on the dimension d and is therefore extensive. However, for the long-range interactions $0 < \frac{\xi}{d} < 1$, equation 2.2.10 blows up to infinity as $N \to \infty$. In this case, the potential energy does not depend on the system size and is nonextensive. To better understand this, consider a large system Σ with $U(\Sigma)$ being the potential energy of Σ. If we try to calculate how scaling the the potential energy scales for a large system $\lambda\Sigma$, with λ being a scaling parameter ($\lambda > 1$), and using the fact that the number of particles is an extensive quantity, i.e., $N(\lambda\Sigma) = \lambda N(\Sigma)$, then for $N >> 1$ we get

$$\frac{U(\lambda\Sigma)}{U(\Sigma)} = \lambda \frac{(\lambda N)^{1-\frac{\xi}{d}} - 1}{(N)^{1-\frac{\xi}{d}} - 1} \approx \begin{cases} \lambda & \text{if } \frac{\xi}{d} \geq 1 \\ \lambda^{2-\frac{\xi}{d}} & \text{if } 0 < \frac{\xi}{d} < 1. \end{cases} \tag{2.2.12}$$

The result does not depend on the microscopic ratio $\frac{\xi}{d}$ for short-range interactions, but it does for long-range interactions. This is why Tsallis generalizes Equation 2.2.7, now called Tsallis entropy [2], to extend beyond the Boltzmann-Gibbs entropy S_{BG}, so that no matter the range of interaction it preserves its extensivity. The theory has, in the years since its creation, been referred to as nonextensive statistics, though it's purpose is to preserve the extensivity. That is the purpose to which Tsallis created his entropy equations, now called Tsallis entropy [2]. A more detailed discussion on nonextensive thermostatics and a generalized H-theorem can also be found in [17]. The nonextensivity feature of the formulation makes it independent of initial conditions and suitable for modeling many-body complex

systems with long-range interactions, such as plasma. Systems with this nonextensive behavior can no longer be characterized by additive entropies, $S_q(A+B) \neq S_q(A)+S_q(B)$, and the different microstates are not in equilibrium. Quantifying the nonextensivity is needed to make rigorous statistical claims and understand equilibrium properties of systems with long-range interactions and correlations. In this formulation, q can be understood as a parameter quantifying the strength of correlations or non-local interactions causing the system to move away from equilibrium. The q-Gaussian distribution of the velocity can be found by extremizing the Tsallis entropy S_q with Lagrange constraints, such as normalization and moment of the distribution. Essentially, the q-Gaussian can be thought of as a generalization of the Maxwellian distribution, with normalization A_q, kinetic energies E, potential energy U_q, and inverse temperature β_q. This results in the following probability distribution function for the kinetic energy

$$p(E) = \frac{\beta_q}{A_q} e_q^{(-\beta_q(E-U_q))} = \frac{\beta_q}{A_q}[1-(1-q)\beta_q(E-U_q)]^{\frac{1}{(1-q)}}. \tag{2.2.13}$$

The relationship between the Maxwellian kinetic temperature T_M and the q-Gaussian kinetic temperature T_q is discussed in [18] and given by

$$T_q(\frac{5q-3}{2}) = T_M \; ; \quad q < 5/3. \tag{2.2.14}$$

Equation 2.2.14 helps to relate the q-Gaussian variance fits (i.e. σ_q^2, D_q, v_{qth}^2, or T_q) to the corresponding Gaussian or Maxwellian values. This step is necessary as the kurtosis of a distribution affects the variance, which should be taken into account to find a more appropriate variance value. Note that in the limit where $q \to 1$, the Maxwellian distribution is recovered from equation 2.2.13. This is accomplished by letting the potential energy $U_q = 0$, $\beta_q = 1/(v_{qth}^2)$, where v_{qth} is the q-Gaussian thermal velocity, and $E = \frac{1}{2}mv^2$, recalling the fact that $e^x = \lim_{n\to\infty}\left(1+\frac{x}{n}\right)^n$ and letting $n = \frac{1}{1-q}$

$$\lim_{q\to 1}\frac{1}{v_{qth}A_q}[1-(1-q)\frac{mv^2}{2v_{qth}^2}]^{\frac{1}{(1-q)}} \to \sqrt{\frac{m}{2\pi v_{th}^2}} * e^{-\frac{v^2}{2mv_{th}^2}}. \tag{2.2.15}$$

We now look at the plots of q-Gaussian distributions for particular values of q and in different dimensions. A simple expression for the q-Gaussian in one dimension, as is plotted in Figure 2.1, is given by

$$p_q(x) = \frac{1}{\sqrt{\pi A_q}}\left(1+\frac{(q-1)x^2}{A_q}\right)^{\frac{-1}{q-1}} \tag{2.2.16}$$

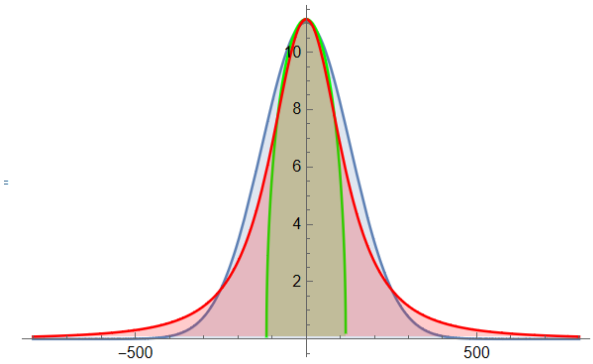

Figure 2.1: Analytical plot of the q-Gaussian distribution for three cases. $q=-1$(Green), $q=1$(Blue), and $q=5/3$(Red).

Figure 2.1 shows different q-Gaussian distributions scaled to the same height to exemplify how the distribution shape deviates from a Gaussian ($q=1$) for different values of the nonextensive parameter q. Of course, the case of one dimension is the simplest. For three dimensions, the expression for a velocity distribution with a q-Gaussian is given by

$$f_q(\mathbf{v}) = nA_q\left(\frac{m}{2\pi k_B T_q}\right)^{3/2}\left[1+(q-1)\frac{m(\mathbf{v}-\mathbf{u})^2}{2k_BT_q}\right]^{\frac{-1}{q-1}} \tag{2.2.17}$$

where m is the mass of the species, $\mathbf{u}$ is the macroscopic velocity flow, k_B is the Boltzmann constant, and T is the temperature.

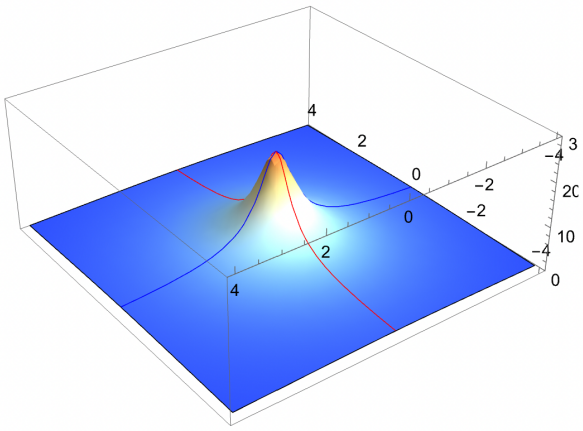

Figure 2.2: Two dimensional plot with $q = 2.5$

For the case of anisotropic q-Gaussian distributions, meaning that q is different for each direction, such as x and y, one cannot just substitute $q = \sqrt{q_x^2 + q_y^2}$, as might be assumed. When such substitution is made, the resulting incorrect distribution will look like the one shown in Fig. 2.3.

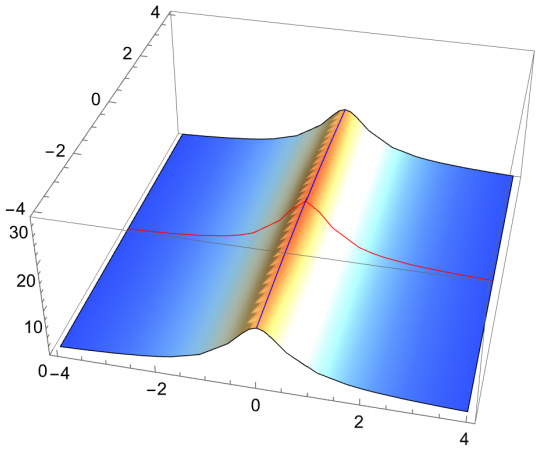

Figure 2.3: Incorrect plot of an anisotropic q-Gaussian distribution.

Here $q_x = 2.5$, which is shown along the red line marking the x-axis, while $q_y = 1$ is shown along the blue line marking the y-axis at the top of the distribution's ridge. Instead,

the correct form is obtained by multiplying q-Gaussians of each directional component as shown in Fig. 2.4. The equation describing this distribution is the following

$$f_q(\mathbf{v}) = nA_q \left(\frac{m}{2\pi kT}\right) \left[1 + (q_x - 1)\frac{m(\mathbf{v_x} - \mathbf{u_x})^2}{2kT_x}\right]^{\frac{-1}{q_x - 1}} \left[1 + (q_y - 1)\frac{m(\mathbf{v_y} - \mathbf{u_y})^2}{2kT_y}\right]^{\frac{-1}{q_y - 1}}. \tag{2.2.18}$$

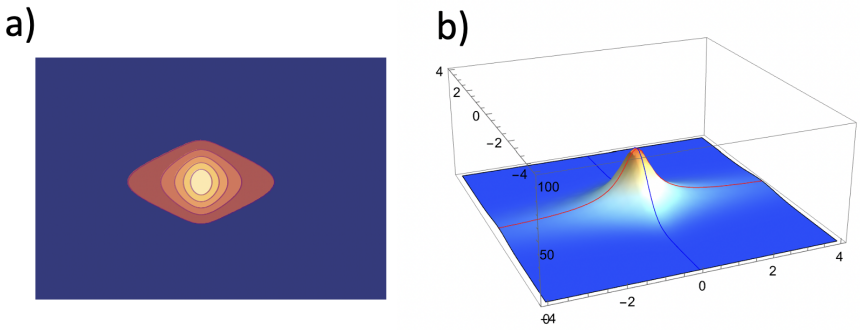

Figure 2.4: Anisotropic q-distribution with $q_x = 2.5$ along the red x-axis and $q_y = 1$ along the blue y-axis shown as a) contour plot and b) surface plot.

The importance of the anisotropic q-Gaussian distribution will be seen in section 4.3. Current literature typically discusses a single q parameter to describe the whole system. Although a single q parameter is commonly used, different authors often express it using alternative forms, such as $q' = 2 - q$ or $q' = 1/q$, depending on the context or formulation. This notational variation can lead to confusion when comparing results across studies unless the transformation is explicitly stated. In this work, we argue that a distinction should be made between the q's found from position distributions and the q's found from velocity distributions, as each of them describe different physical phenomena related to anomalous diffusion. For example, Eq. 2.2.2 and Eq. 2.2.13 have the same functional form, but have different variables, coefficients, and exponents as the former is in position space, while the latter is in velocity space. Since one provides particle position information and the other particle velocity information, we will refer to the different q's as q_p and q_v later in the text. A possible way to unite the two may be an equation similar to the Einstein relation, which

connects the diffusion and the temperature with mobility μ with charge e_α of species α is $D_\alpha = \mu_\alpha \cdot \frac{k_B T_\alpha}{e_\alpha}$. However, we are not aware of a nonextensive equivalent of this extension that connects q_p with q_v.

2.3 Connecting the Statistical Approach to the Spectral Approach

Next, we connect nonextensive statistics to a spectral approach to anomalous diffusion that uses fractional derivative operators. To do this, we first discuss the connections between q distributions and Lévy distributions. A Lévy distribution arises as a solution to the following fractional partial differential equation [19] [Eq. (34), p. 15]; [20] [Eq. (58), p. 26]

$$\frac{\partial p(x,t)}{\partial t} = D \frac{\partial^\gamma p(x,t)}{\partial |x|^\gamma}, \quad 0 < \gamma < 2. \tag{2.3.1}$$

The solution in one dimension is known as a Lévy distribution $L_\gamma(x)$ [19, Eq. (61), p. 33] and is given by

$$p(x,t) = (Dt)^{1/\gamma} L_\gamma \left(\frac{x}{(Dt)^{1/\gamma}} \right). \tag{2.3.2}$$

Typically, α is used as exponent in Equations 2.3.1 and 2.3.2, and these are called α-stable Lévy processes. However, since we use α for the power-law exponent in the mean squared displacement (MSD), here we adopt the symbol γ instead. The exponent γ relates to the order s of the fractional Laplacian operator by the following scaling relation $\gamma = 2s$ for $0 < s < 1$ [20] [Chapter 5, pp. 222–224]. The MSD of a Lévy process is described by the relation $\langle x^2 \rangle \propto t^{2/\gamma}$ in the asymptotic limit of large t, which implies the scaling relation $\alpha = 2/\gamma$. Since γ is defined in the range $0 < \gamma < 2$, the corresponding MSD exponent is $\alpha > 1$, which is classified as superdiffusive process. A Lévy distribution does not obey the classical central limit theorem, as it has infinite variance. Instead, it arises from the generalized central limit theorem, which applies to sums of independent identically distributed (i.i.d.) random variables with heavy tails. If the individual variables are instead constrained to

have finite variance, their sum converges to a Gaussian distribution by the classical central limit theorem. Thus, one of the unique properties of Lévy distributions is that the random variables do not need to have a finite variance. The variance of q-Gaussian distributions are finite for $q < 5/3$ but diverge and approach a Lévy distribution for $5/3 \leq q < 3$ in 1D. For this range of validity, the exact connection between the Lévy parameter γ and the nonextensive parameter q is $\gamma = \frac{3-q}{q-1}$ [2]. The threshold value of q for which this scaling relation holds depends on the dimensionality d by $q > \frac{4+d}{2+d}$. Thus, for example, for $d = 1$, $q > \frac{5}{3}$, the process can be called Lévy. For $q < \frac{5}{3}$ (implying the mathematical variance is finite), there are no Lévy processes. Here we make a distinction between position and velocity distributions characterized by $q_p > 5/3$. For position distributions with $q_p > 5/3$, the diffusion is a Lévy process and yields very large particle displacements called Lévy flights. For velocity distributions with $q_v > 5/3$, we call a process 'energetic' or 'suprathermal'.

Infinite variance would seem to imply an infinite temperature or diffusion, which is of course not physical. The solution lies in taking a closer look at the step size of the random walk that yields the Lévy distribution. During a Lévy process, a "Lévy flight" is an occasional occurrence of a very large step size, or "flight", while most step sizes are still small. In the mathematical definition of Lévy distributions, there is no restriction to the size of this jump, i.e. no boundary conditions. In a standard random walk that leads to a Gaussian distribution, the step size is proportional to the mean free path λ_{mfp}. However, we expect that when a system exhibits superdiffusion, there will exist another subset of step sizes $\lambda_q > \lambda_{mfp}$, where λ_q represents the characteristic scale of a jump driven by nonlocal interactions. If $\lambda_q \ggg \lambda_{mfp}$, then Lévy flights occur. To avoid infinite jumps, we impose $\lambda_q \ll L$, where L is the system size. Based on this picture, here we define a Lévy process as a sub-regime of superdiffusion - one in which some step sizes are much greater than the mean free path step size.

Lévy processes are also known in the context of the Fractional Laplacian $(-\Delta)^s$, which can be used to rewrite Eq. 2.3.1 in the following way

$$\frac{\partial p(x,t)}{\partial t} = D(-\Delta)^s p(x,t), \tag{2.3.3}$$

where we made the substitution $s = \gamma/2$. Notice that, while Eq. 2.3.1 is nonlinear, Eq. 2.3.3 is linear, which is one major reason for using fractional operators. In Eq. 2.3.3, values of $0 < s < 1$, describe a superdiffusive process, while $1 < s < 2$ models a subdiffusive process. However, the upper cutoff on the validity of this is not certain, especially since $s = 2$ yields the Bi-harmonic operator.

For finite-variance q-distributions in 1D, i.e., for $q < 5/3$, the scaling relation between Tsallis's q and the nonlocality fraction s on the Laplacian can be obtained from the shared nonlinear relationship with the Mean Squared Displacement $MSD \propto \tau^{\alpha} \propto \tau^{1/s} \propto \tau^{2/(3-q)}$

$$\frac{1}{\alpha} = s = \frac{3-q}{2} \text{ for } q < 5/3. \tag{2.3.4}$$

The scaling relation in Eq. 2.3.4 is valid in the long time delay limit $\tau \to \infty$. For q-distributions in the infinite-variance regime, i.e., $q \geq 5/3$, a scaling relation can be obtained using the shared relation with the γ exponent from the Lévy distribution $\gamma = (3-q)/(q-1)$ and $\gamma = 2s$

$$s = \frac{3-q}{2q-2} \text{ for } q \geq 5/3. \tag{2.3.5}$$

These scaling relations and connections across models are further discussed in [2]. These relations are plotted in Figure 2.5.

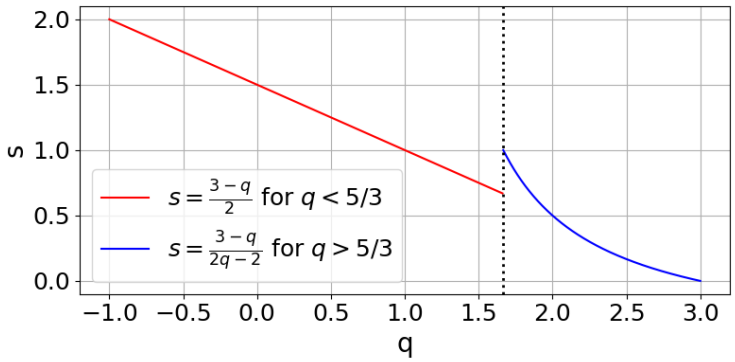

Figure 2.5: Scaling relations between the nonextensive parameter q and the fraction s on the Laplacian for two distinct regimes. The critical value separating the regimes is $q = 5/3$.

The discontinuity at $q = 5/3$ means that there is not a bi-jective mapping between s and q. The difference between the two scaling relations at $q = 5/3$ raises questions on which model is more valid in the range $2/3 < s < 1$ where the plot in Fig. 2.5 shows discontinuity. If one measures the MSD of a system and uses $\alpha = 1/s$ to find s, then either $s = \frac{3-q}{2}$ or $s = \frac{3-q}{2q-2}$ can be used to solve for q in the range $2/3 < s < 1$. However, if q is obtained first then there is only one s it maps onto. To understand better the region of convergence between the fractional Laplacian and the q-Gaussian approach, a fast Fourier Transform (FFT) numerical solution (p_s)of Equation 2.3.3 is compared to the q-Gaussian 2.2.16 (p_q) with a sufficiently long time-delay after the initial condition for three representative cases. The results are shown in Figure 2.6.

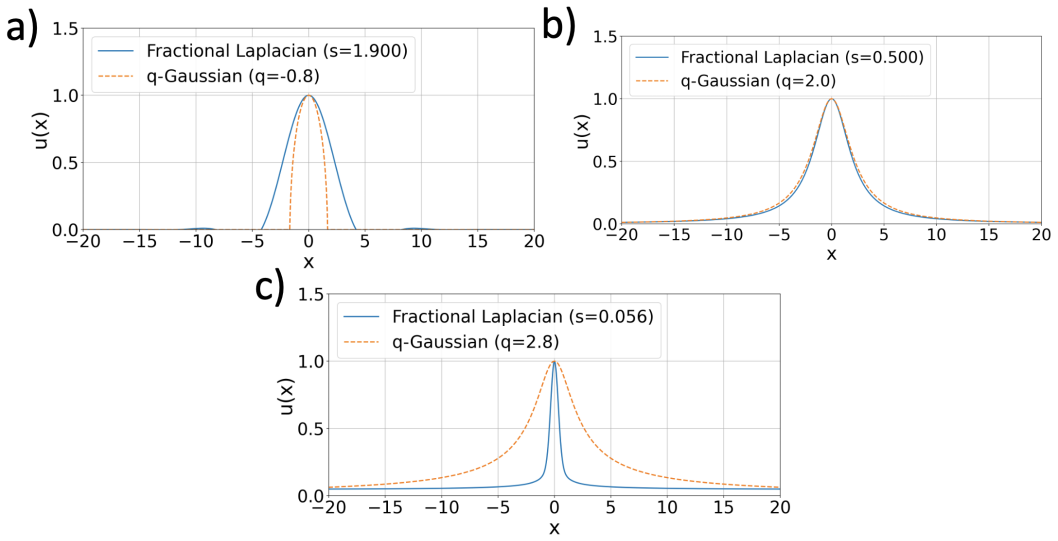

Figure 2.6: Fractional Laplacian diffusion solution (solid) and q-Gaussian distribution (dashed) for a) $q = -0.8$ (subdiffusion case, $s = 1.9$), b) $q = 2.0$ (Lévy flight case, $s = 0.5$), and c) $q = 2.8$ (Lévy flight case, $s = 0.056$).

The three figures are representative of two extremes: $q = -0.8, s = 1.9$ and $q = 2.8, s = 0.056$ and the intermediate case of $q = 2, s = 0.5$, where the case $s = 0.5$ has been well studied mathematically. As can be seen in Figure 2.6, the two solutions converge well for the intermediate case and substantially differ for the extreme cases. To assess the similarity between the numerical solution $p_s(x)$ and the q-Gaussian profile $p_q(x)$, we computed two key metrics: the Jensen-Shannon divergence (JSD) and the pointwise residual across x and q. The JSD is a symmetric and bounded variant of the Kullback–Leibler (KL) divergence, useful for comparing two probability distributions

$$D_{\mathrm{JSD}}(p_s \| p_q) = \frac{1}{2} D_{\mathrm{KL}}(p_s \| m) + \frac{1}{2} D_{\mathrm{KL}}(p_q \| m), \quad \text{where } m = \frac{1}{2}(p_s + p_q). \tag{2.3.6}$$

The Kullback–Leibler (KL) divergence for continuous probability density functions is defined as

$$D_{\mathrm{KL}}(P \| Q) = \int P(x) \log\left(\frac{P(x)}{Q(x)}\right) dx, \tag{2.3.7}$$

and it measures the information lost when $Q(x)$ is used to approximate $P(x)$, where $P(x)$ and $Q(x)$ are continuous probability density functions over the variable x. It is asymmetric and can diverge if $Q(x_i) = 0$ while $P(x_i) > 0$, but the JSD overcomes these limitations by symmetrization and smoothing of the distributions. In our case, the JSD quantifies how much the numerical PDF $p_s(x)$ diverges from the theoretical q-Gaussian $p_q(x)$. JSD is typically bounded between 0 and $\ln(2)$, but we rescale to a percentage between 0% and 100%. High values of JSD for $q < 1$ indicate poor agreement between the two (e.g., due to cutoff behavior or long tails), while its sharp decrease near $q = 1$ reflects strong similarity. As shown in Figure 2.7, the JSD is under 10% for $0 < q < 2.7$, indicating close agreement in these anomalous diffusion regimes.

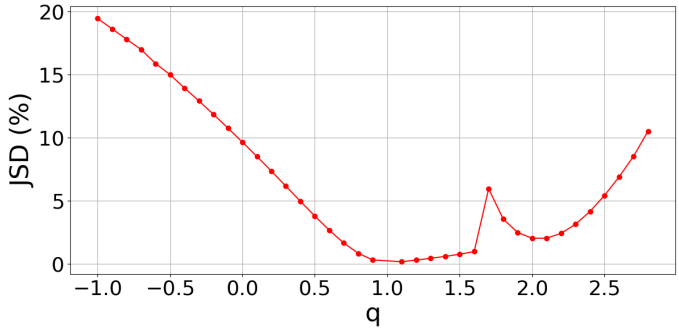

Figure 2.7: Jensen–Shannon Divergence across a range of q values. JSD drops rapidly near $q = 1$

To understand the spatial nature of the error, we computed a residual:

$$\Delta(x, q) = p_s(x) - p_q(x), \tag{2.3.8}$$

and plotted it across x and q. The contour map, shown in Figure 2.8, highlights for which q values the deviations are most significant.

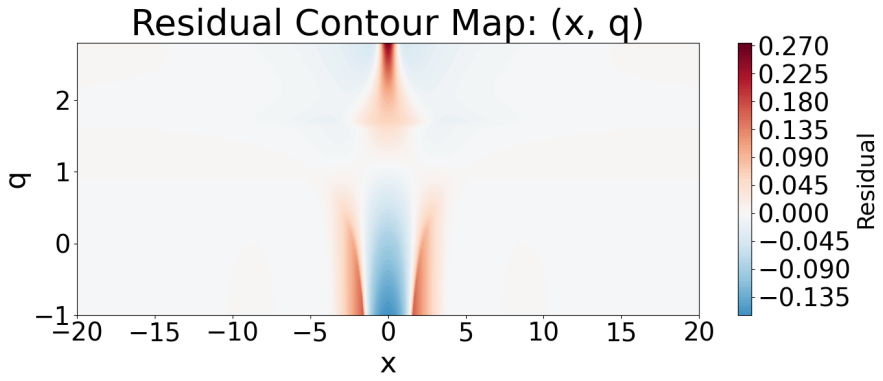

Figure 2.8: Residual contour plot showing the point-wise difference $\Delta(x, q) = p_s(x) - p_q(x)$ across the spatial domain x and parameter q. Blue regions indicate excess in the fractional Laplacian solution, red regions indicate excess in the q-Gaussian.

The q-Gaussian solution corresponds to the nonlinear diffusion Equation 2.2.1, while the $p_s(x)$ solution corresponds to the fractional diffusion Equation 2.3.3. There seem to be parameter spaces where the two agree both in the bulk and tails of the distribution. These are the white regions of in Figure 2.8. This brings the argument that one may model systems with nonlinear dynamics with fractional operators if the appropriate scaling is known. For the above example, it seems that the range $0.5 < q < 2.1$ or $0.41 < s < 1.25$ exhibits small enough differences between the solutions of the two diffusion equations, suggesting that scaling between q and s can be used to connect nonextensive statistics to the spectral model, which will be discussed next.

Before moving to the spectral approach to anomalous diffusion, we conclude this section by summarizing the scaling relations between nonextensive statistics with the q-Gaussian, the nonlinear Fokker-Planck equation, and the fractional diffusion equation with a diagram (Fig. 2.9) inspired by Griffith's introductory text to electricity and magnetism.

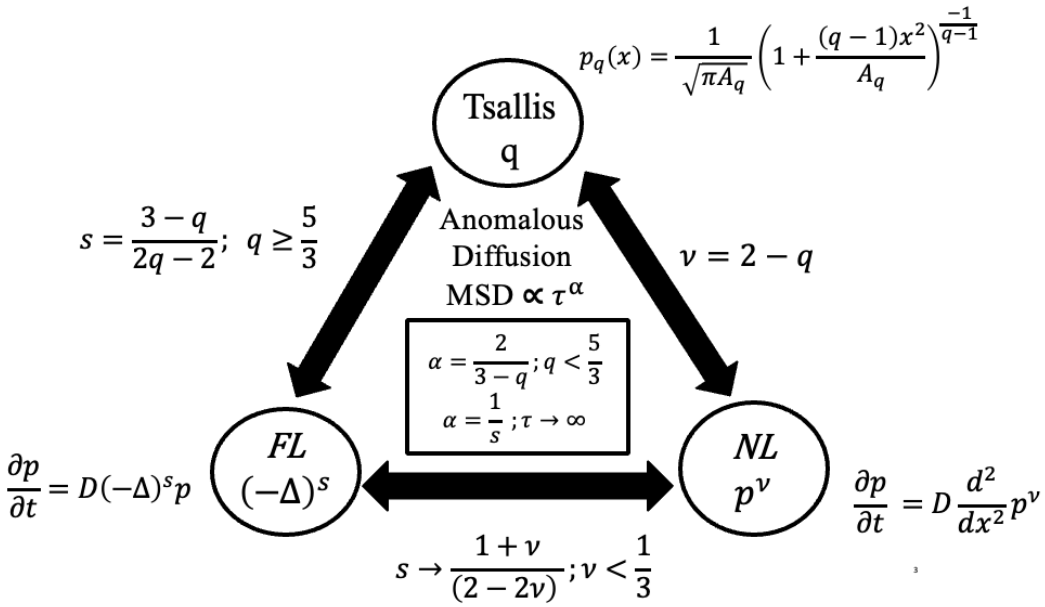

Figure 2.9: Triangle of scaling relations between nonextensive statistics, nonlinear diffusion equations, and fractional diffusion equations, which all can be used to model anomalous diffusion.

2.4 Spectral Approach

In addition to nonlocal interactions and correlations, anomalous diffusion can be affected by stochastic processes, such as random fluctuations of the potential energy across the spatial domains. This is especially true for strongly coupled systems, like dusty plasmas, where the electrostatic interaction potential is sensitive to both fluctuations in the dust charging and the relative position of each dust grain in space. Here we combine the effects of nonlocality and stochasticity by studying a discrete random fractional Schrodinger operator. This Anderson-type Hamiltonian has a fractional Laplacian kinetic energy term and a stochastic disorder potential energy term. The energy spectrum of this Hamiltonian has been recently used by Kostadinova et al. to determine the onset of turbulence in dusty plasma monolayers [12]. As discussed in the previous sections, here we use the series representation of the Fractional Laplacian, first introduced by Padgett et al. [11] and study the energy spectrum of the Hamiltonian using the extended states conjecture derived by Liaw [3].

The discrete random fractional Schrodinger (DRFS) operator has the following form

$$H_{s,\epsilon} \equiv (-\Delta)^s + \sum \epsilon_i \langle \cdot, \delta_i \rangle \delta_i, \tag{2.4.1}$$

where the fractional Laplacian $(-\Delta)^s, s \in (0,2)$ is defined as

$$(-\Delta)^s u_n \equiv \sum_{m \in \mathbb{Z}}^{m \neq n} K_s(n-m)(u_n - u_m) \tag{2.4.2}$$

$$K_s(m) \equiv \begin{cases} \frac{4^s \Gamma(1/2+s)}{\sqrt{\pi}|\Gamma(-s)|} \frac{\Gamma(|m|-s)}{\Gamma(|m|+1+s)} & \text{if } m \in \mathbb{Z}/\{0\} \\ 0 & \text{if } m = 0 \end{cases}. \tag{2.4.3}$$

The kernel $K_s(m)$ in the above expression serves as a weight that quantifies the range and strength of the nonlocal interaction (i.e., interaction beyond the nearest neighbors). The potential energy term in Eq. 2.4.1 consists of independent variables ϵ_i, identically distributed according to a uniform (flat) distribution on the interval $[-c/2, c/2]$, where $c > 0$ is a dimensionless disorder parameter. In equation 2.4.1, δ_i is the i^{th} standard basis vector of the 1D integer space $\mathbb{Z}$ and $\langle \cdot, \cdot \rangle$ is the $l^2(\mathbb{Z})$ inner product in the space.

The nonlocal interaction modeled by the discrete Fractional Laplacian can be visualized with a matrix representation. In this context, the matrix form refers to the discretized operator acting on a vectorized field, where each matrix entry represents the strength of interaction between two points. For the classical Laplacian, the resulting matrix is sparse, with nonzero elements only for nearest neighbors (i.e., a tridiagonal structure), as shown in Figure 2.10 b). In contrast, the matrix representation of the fractional Laplacian (here for $s = 0.5$, shown in Fig. 2.10 a)), contains nonzero off diagonal terms for all matrix elements, which represents the nonlocal nature of the interaction. It can also be seen that the off diagonal terms of the fractional Laplacian matrix rapidly fall off with nonlocal range m.

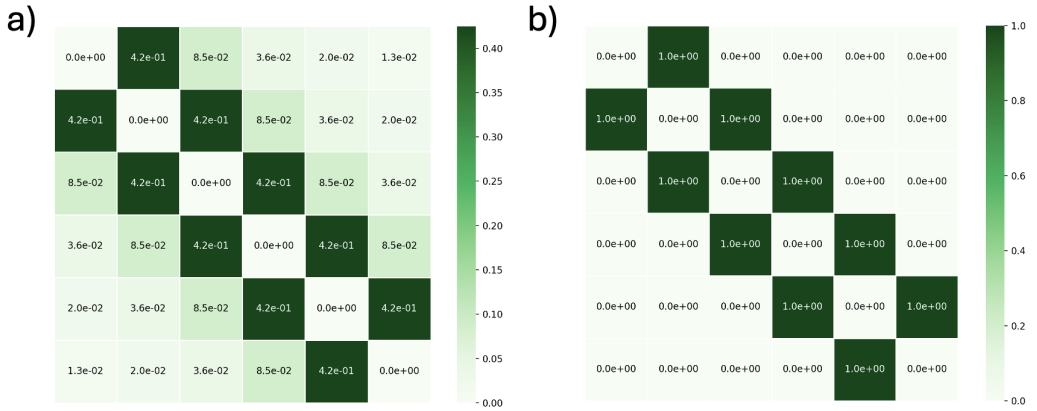

Figure 2.10: Matrix representation of (a) the fractional Laplacian with $s = 0.5$ and (b) the classical Laplacian. The color bar represents interaction strength.

In the spectral approach, the Hamiltonian in equation 2.4.1 iteratively operates on an initial basis vector δ_0, which results in propagating the energy state in Hilbert space. The sequence of energy states obtained after N iterations of the Hamiltonian is given by

$$\{\delta_0, H^1_{s,\epsilon}\delta_0, H^2_{s,\epsilon}\delta_0, \ldots, H^N_{s,\epsilon}\delta_0\} \rightarrow \{H^k_{s,\epsilon}\delta_0\}^N_{k=0}. \tag{2.4.4}$$

A Grahm-Schmidt orthogonalization (without normalization) is performed on this sequence to obtain a new sequence

$$\{\varphi'_0, \varphi'_1, \varphi'_3, \ldots, \varphi'_N\} \rightarrow \{\varphi'_k\}^N_{k=0}. \tag{2.4.5}$$

Each of the vectors φ'_k represents the new information obtained by the k^{th} iteration of the Hamiltonian. The orthogonalization of the sequence also allows the definition of a mathematical distance equation in the Hilbert space (i.e., the generalization of the Euclidean vector distance to infinite-dimensional space). For any vector in the Hilbert space ν, such that $\nu \neq \delta_0$, the mathematical distance between ν and the k^{th} element of the orthogonalized sequence $\{\varphi'_k\}^N_{k=0}$ is given by

$$D_{s,c}^{N} \equiv \sqrt{1 - \sum_{k=0}^{N} \left(\frac{\langle \nu, \varphi_k' \rangle}{\|\nu\| \|\varphi_k'\|} \right)^2}. \tag{2.4.6}$$

This distance in Hilbert space can be interpreted as the probability of transport away from the initial state. Mathematically, the extended states conjecture states that $\lim_{N\to\infty} D_{s,\epsilon}^{N} \neq 0$ implies the existence of a continuous spectrum for the Hamiltonian, i.e., the existence of extended states. The opposite statement, $\lim_{N\to\infty} D_{s,\epsilon}^{N} = 0$, implying, increased probability for localization, is less rigorous since, in the absence of extended states, the remaining spectrum can consist of both a singular part (i.e., eigenvalues) and a poorly-behaved singular-continuous part. The calculation of Equation 2.4.6 and the analysis on the limiting value of $D_{s,c}^{N}$ will be referred to as the Fractional Laplacian Spectral Method (FLSM).

In chapter 5, we will use the FLSM to calculate the probability for the existence of extended states for Hamiltonian operators that correspond to the nonlocality and stochasticity measured in dusty plasma experiments from the Plasmakristall-4 (PK-4) facility on board the ISS. The changes in the calculated spectra will be used to understand changes in the stability and dynamics of the observed global structural states of the dusty plasma clouds. In addition, we will investigate how high probability for extended states at characteristic scales in Hilbert space can be linked to the characteristic scales of dust particle jumps observed in the PK-4 experiments. The dust particles in these experiments are mostly confined within self-organized structures reminiscent of liquid-crystalline filamentary states. However, examination of the video data reveals that, occasionally, individual dust particles can escape from the lattice-like filamentary structures and perform big jumps. These are similar to Lévy flights, which may quickly take such particles outside the field of view. However, these jumps are not scale-free and infinite, but can be quantified. Thus, while such jumps are larger than the typical scale of displacements in the system, they are not larger than the scale of the system. Therefore, these jumps are classified as intermediate between Lévy flights and mean free path displacements. These are of the proposed scale $\lambda_{mfp} \ll \lambda_q \ll$ *Lévy*. In

5.2, we present quantitative analysis of particle jumps from particle tracking data and study anomalous diffusion in dusty plasma using the spectral approach.

The theoretical framework described so far allows for a connection between the experimentally-extracted nonextensive statistical parameter q_p and the nonlocality fraction s on the fractional Laplacian kinetic term of the Hamiltonian in FLSM. With this connected approach, we will analyze dusty plasma experiments in chapter 5 and magnetized plasma simulations in chapter 6. First, however, we will discuss the current state of research applying nonextensive statistics to plasma physics, henceforth called nonextensive plasmas. The next chapter aims to show the applicability of nonextensive statistics to a breadth of plasma regimes. In addition to providing a comprehensive literature review, we discuss future work that can be done in the field of nonextensive plasmas.

Chapter 3

Nonextensive Statistics in Plasma Physics

Tsallis' nonextensive statistics offers a valuable framework for studying plasma systems far from equilibrium, where traditional Boltzmann-Gibbs approaches often fail. Its utility lies in capturing anomalous diffusion, long-range correlations, and the emergence of power-law tails in velocity and spatial distributions. However, the plasma physics literature applying nonextensive theory remains somewhat fragmented and inconsistent, with several studies exhibiting algebraic discrepancies and divergent definitions that underscore the need for clearer theoretical standards and consensus. As an example, one often finds redefinitions like $q' = 2 - q$ or $q' = 1/q$, which does not change underlying physics, but can lead to confusion and error when comparing results. In addition, most studies adopt a single entropic index q; however, in the present work we see that, in complex systems like dusty plasmas, there may be a more nuanced picture, where different q-values may characterize spatial versus velocity-based processes, such as diffusion and temperature evolution. This distinction between q_p from position distributions and q_v from velocity distributions reflects underlying anisotropies and direction-dependent transport properties that are often neglected in simplified models.

Work done in [21, 22, 23] provides a theoretical equation for what the nonextensive parameter q would be in terms of temperature gradients, Lorentz forces, and inertial forces. A wide body of work has examined how nonextensive distributions modify fundamental plasma transport parameters. Studies have derived expressions for diffusion coefficients, mobility, thermal and electrical conductivity, Hall and Nernst effects, and heat flux under both suprathermal and subthermal q- or κ-distributions [24, 23, 25, 26, 27]. These effects extend to viscosity, thermal diffusion, and related anisotropies [28, 29], especially in the

presence of magnetic and inertial forces. Theoretical advances in this area have supported a deeper understanding of transport in weakly and fully ionized plasmas. Theoretical studies have also explored how nonextensivity influences wave dynamics, including electrostatic wave breaking and instability growth rates in anisotropic whistler mode dispersion [18, 30]. These models introduced q-dependent scaling laws for plasma beta, temperature, and wave damping behavior, distinguishing between superextensive ($q < 1$) and subextensive ($q > 1$) regimes. Generalizations of the plasma dispersion function have been developed [31], alongside derivations of q-dependent dispersion relations, growth rates, and normalization factors for electrostatic waves [32, 33]. Constraints from experimental data have supported values near $q_e = 0.77$, where q_e is the is the electron q_v parameter quantifying nonequilibrium, suggesting measurable deviations from Maxwellian assumptions in real plasmas.

Complementary studies have examined dielectric response, relativistic dispersion relations [34, 35], and suprathermal wave behavior in nonextensive plasmas. The dielectric function and wave dispersion were analyzed in both relativistic and non-relativistic regimes [36, 37], while suprathermal corrections to wave penetration depth were captured through q-dependent skin-depth models [38]. Nonextensive effects on Langmuir wave propagation, modulational instability, and collapse dynamics were similarly explored in relativistic plasmas [39, 40]. Landau damping of ion-acoustic waves, particularly under hybrid Cairns–Tsallis distributions, was shown to be highly sensitive to both nonextensivity and nonthermality [41]. Modeling of nonlinear structures in pair plasmas, ion-acoustic solitons, and streaming plasmas further expanded the framework. Kinetic studies on acoustic-like modes in nonextensive pair plasmas showed that deviations from Maxwellian distributions significantly affect dispersion and phase velocities [42], while ion-acoustic soliton dynamics and modulational stability were found to depend strongly on the nonextensive index and electron temperature ratios [43]. Broader ion energy spectra resulting from the expansion of collisionless plasmas with q-distributed electrons were derived in [44], with implications for laser-plasma interaction and astrophysical outflows. Additional models demonstrated that electron-acoustic solitary

waves governed by q-modified Korteweg–de Vries equations evolve based on both the nonextensive index and background streaming conditions [45]. Some of the relevant equations capturing how nonextensivity modifies plasma parameters in these regimes are collected in Appendix A.

Application to plasma turbulence and quantum plasmas have also found use for nonextensive statistics. Early foundational studies applied Tsallis entropy to two-dimensional plasma turbulence, uncovering meta-equilibrium states and modified radial profiles inconsistent with classical models [46, 47]. More recently, simulation studies using particle-in-cell models and analytical treatments of wave–particle resonances have shown how non-Maxwellian features alter instability growth and structure formation in turbulent and magnetospheric plasmas [48, 49]. In the context of quantum and high-energy plasmas, nonextensive Tsallis distributions have been used to model electron trapping and potential modification in degenerate regimes [50], while hydrodynamic models incorporating time-dependent q-parameters in quark-gluon plasmas revealed strong sensitivity of bulk pressure evolution to nonextensive effects despite similar temperature and energy density evolution to the Boltzmann limit [51].

In the past decade, important contributions to the fundamentals of nonextensive plasma were published. Davis and Laming (2019) [52] provided a theoretical justification for the emergence of nonextensive distributions in steady-state, collisionless plasmas. They showed that such systems inherently exhibit superstatistical behavior, where fluctuations in intensive variables like temperature naturally lead to Tsallis-like distributions. Silveira and Benetti (2021) [53] proposed a physical interpretation of the deformation parameter q in nonextensive statistics by analyzing a nonextensive plasma. Their study suggests that the parameter q can be understood as a generalized expression of the number of degrees of freedom in the system. Later Davis et al. (2023) [54] investigated how kappa distributions arise from particle correlations in nonequilibrium steady-state plasmas using simulations. Their results provided a microscopic justification for using nonextensive statistics in plasma environments

with persistent fluctuations and constrained dynamics. McComas and Livadiotis (2025) [55] conducted numerical experiments to explore how correlations between particles give rise to kappa-like distributions in plasma systems. Their study deepens the physical understanding of how nonextensive behavior emerges from underlying interaction mechanisms in long-range coupled systems.

Nonextensive effects have also been explored in low-temperature and sheath plasmas. Hatami and Tribeche [56] generalized the Bohm criterion, while Qiu et al. [57, 58] reported the first experimental measurement of the electron q-parameter and analyzed its effects on sheath potentials. Sharma et al. [59] and Kikuchi [60] emphasized the influence of anisotropy and non-Maxwellian statistics on boundary behavior, and El Bojaddaini and Hatami [61] studied electronegative sheaths with ion sources, showing strong departures from classical sheath models. In dusty plasmas, nonextensive models have been both experimentally validated and theoretically extended. Liu and Goree [8] observed superdiffusive transport and heavy-tailed velocity distributions, while subsequent works [62, 63, 64] explored dust charging and nonlinear wave propagation using q-distributions. Recent work [65, 66, 67] explored secondary emission and nonlinear dynamics in complex sheath regions, illustrating how nonextensive statistics enhances the modeling of charged dust behavior and wave steepening.

In space plasmas, the emergence of kappa-distributions—empirical precursors to q-Gaussians—began with Vasyliunas [68], who modeled suprathermal populations in the solar wind and magnetosphere. Later work by Leubner, Treumann, Burlaga, and Livadiotis [69, 70, 71, 72, 73, 74, 75] expanded these ideas, showing that nonextensive distributions accurately describe multiscale fluctuations, long-range interactions, and statistical features of heliospheric data. Liu and Du [76], Tribeche [77], and Pierrard and Lazar [78] extended these ideas to wave dynamics and solar wind modeling. This extends to solar turbulence, where Pavlos and Karakatsanis [79, 80] modeled sunspot and solar flare dynamics using nonextensive frameworks, capturing the interplay between turbulence, self-organized criticality, and

chaos. More recently, Pierrard, Mushtaq, and Ourabah [81, 82, 83] refined exospheric models, explored Landau damping, and linked observed power-law tails to entropy-preserving temperature fluctuations, solidifying the role of q-distributions in space plasma research.

Despite the prominence of fusion plasmas in research and funding, nonextensive frameworks have only recently been applied in this area. Bouzat, Pain, and Haubold [84, 85, 86] introduced foundational models incorporating Tsallis statistics into transport and fusion yield calculations. More recently, Qiu and colleagues [87, 88, 89] applied nonextensive geodesic acoustic mode (GAM) theory to interpret turbulence, measure the ion nonextensive parameter ($q_i = 1.565$), and even predict disruptions in tokamak plasmas. These studies suggest that even in fusion plasmas, nonextensive statistics may offer powerful new tools for diagnosing and controlling fusion plasma behavior.

In total, to the best of our knowledge, there are currently 74 publications over the 34 years that use nonextensive statistics for plasma physics. Considering the complication of plasma kinetics at the fundamental level in the presence of long range collisional effects and particle correlations, we argue that Tsallis statistics can offer a relatively simple, fundamental, and analytical method to help incorporate these effects in various plasma models.

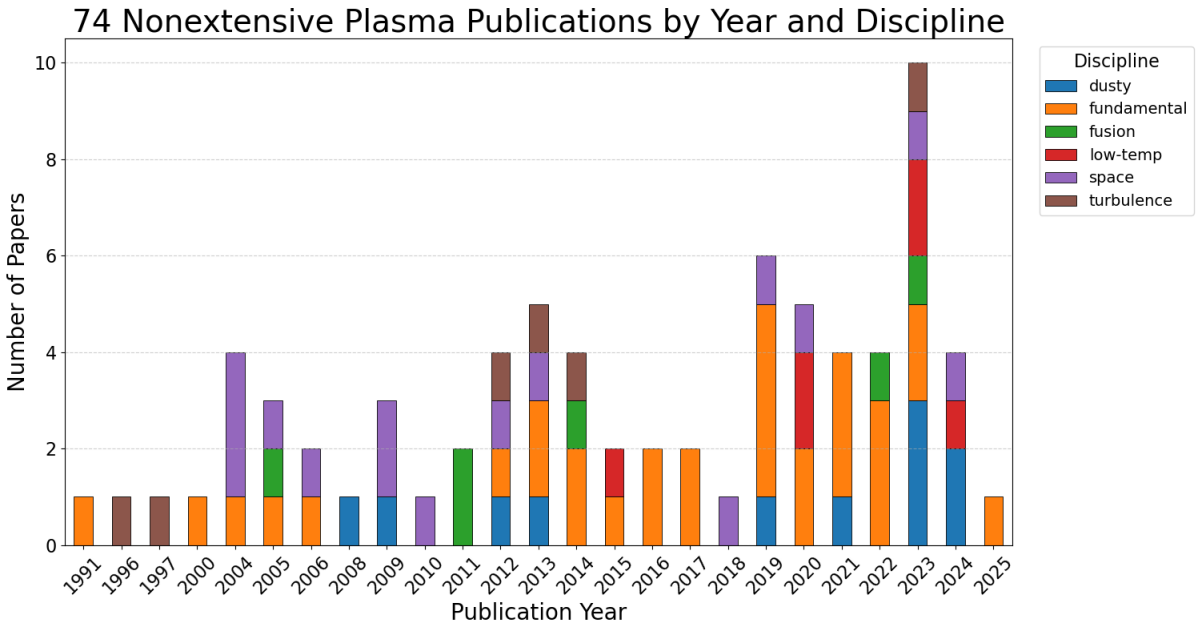

Figure 3.1: Bar plot of papers published over the years that use nonextensive statistics in plasmas.

Figure 3.1 shows how nonextensive statistics has been used in plasma physics research since its inception to the time of writing this dissertation. Different sub-disciplines have also been added to provide even more clarity to the reader on how the theory has been used thus far. These publications have shown both the validity of using nonextensive statistical theory with plasmas, such as in [33, 37, 78, 8] and later in this dissertation in chapter 4, as well as, theoretical phenomena that may exist in plasma such as [66, 56, 89]. While research into applying nonextensive theory to plasma physics exists and has produced great results, the wide range of plasma phenomena and the consideration and application of this fundamental theory imply that there is so much more that can be studied regarding this topic. Here are more examples of theoretical work that could be done to better understand plasma kinetics with nonextensive statistics:

- Preliminary 1D kinetic simulation results show that the two-stream instability may, after a long time, relax to a steady-state q-Gaussian distribution, showing memory in the system after turbulent mixing.

- Using a q-Gaussian distribution as the input for a background electron population to see how atomic line spectroscopy changes and comparing how much the line emission intensity deviates from that of a Maxwellian. This could also be experimentally tested.
- Finding a relation between q-Gaussians and correlation distributions in the BBGKY Hierarchy.
- Analyzing the Balescu-Lenard kinetic equation with assumption of the q-Gaussian distribution function.
- Discovering if a possible derivation of q-Gaussians in both spatial q_p and velocity q_p space can be done from the full phase-space Fokker-Planck equation with collisions.

Also in Appendix B, connections between Deuterium-Tritium plasma resonant wave heating and nonextensive statistics are shown. More possible theories and applications could be listed out, as many as there are plasma phenomena, but with the added nonextensive effect where applicable. In summary, nonextensive statistical theory has been applied to plasma physics with 74 publications in 36 years. However, the application of this theory to plasma physics has shown to be very fruitful. With the introduction of the q_v parameter a greater understanding of the kinetics of a plasma can be achieved by being able to quantify and describe the nonequilibrium properties. This can give better matching with theory and experiment on plasma parameters such as wave dispersion relations, temperature, and even as a possible predictive tool of disruptions in magnetically confined plasmas to help achieve nuclear fusion. We move now to modeling anomalous diffusion via application of nonextensive statistics and the Fractional Laplacian Spectral Method (FLSM) for the Plasmakristall-4 (PK-4) dusty plasma experiment on the International Space Station (ISS) and for the magnetic field line structure from simulations of NSTX-U equilibria.

Chapter 4

Application of Nonextensive Statistics to Anisotropic Anomalous Diffusion in Microgravity Dusty Plasma

Complex (or dusty) plasmas are a collection of electrons, ions, neutral particles, and dust grains (typically micro- to nano-meter in size). Dusty plasma is ubiquitous in astrophysical and space environments, as well as in laboratory settings, both on Earth and in microgravity. Dusty plasma is a unique analogue system for the study of complex phenomena such as phase transitions, anomalous diffusion, and metastability. The particles in these systems are visible at the kinetic level, thus allowing for a reconstruction of the entire phase space. In addition, particle tracking or velocimetry techniques can be used to obtain statistically significant amount of data. Finally, dusty plasma experiments are reasonably simple to build (table-top) and highly controlled, which makes them ideal for deployment in space. Due to the complex interactions among the different charged species involved, dusty plasmas are observed to exhibit various waves, instabilities, and nonlinear structures [90, 91]. Dusty plasmas are also ideal for studying solid-liquid phase transitions [92, 93, 94], electroheology [95, 96, 97], strong interparticle coupling and long-range interactions [98, 99, 100], kinetic theories and diffusion properties [101, 102, 8, 103, 104], critical phenomena such as melting and crystallization [94, 104, 105], and turbulence [12, 106, 107]. As they exhibit many-body effects, dusty plasmas are useful analogue systems for the study of complex systems such as condensed matter [108, 12] and smart materials [109, 95, 110]. Many other physical aspects and applications of dusty plasma have been summarized in several recent overview papers [111, 112, 113]. With all the characteristics described above, dusty plasmas are ideal for testing new analytical models, especially nonequilibrium or nonextensive statistics,

anomalous diffusion, and stochasticity [12, 114, 115, 116, 8, 103]. Recently the Fractional Laplacian Spectral Method model using an Anderson Type Hamiltonian with a long-range Fractional Laplacian operator was developed and adapted for studying structure formation and dynamics in dusty plasma [12].

Here we investigate dusty plasma experiments conducted in the Plasmakristall-4 (PK-4) facility on board the International Space Station, where the microgravity environment allows to neglect gravity and confinement forces, thus, focusing on plasma-mediated dust-dust interactions. Recent studies using the PK-4 facility [117] have investigated various dynamical phenomena, including dust ionization waves [118, 119, 120], ion density waves [121], dust acoustic waves [122], unsteady shear flows and flow patterns fluctuations [123], and liquid-crystal structural states [**?**, 93]. Additionally, analysis of PK-4 data has inspired a breadth of numerical studies, including particle-in-cell simulation of PK-4 predicting the formation of ionization waves [124] and molecular dynamics simulations of dust and ions investigating how such ionization waves can cause anisotropies in the ion wakefields around the dust grains [125, 126]. Finally, non-Maxwellian distributions of the dust velocities have been observed in PK-4 experiments with RF discharge configuration [103].

In this dissertation, we explore anomalous dust diffusion in PK-4 experiments in a pure DC discharge, where a polarity-switching external electric field causes anisotropies on the dust-dust interaction potential and the resulting dust diffusion. We examined nine combinations of pressure-current experimental conditions, each resulting in a slightly different structural state of the dust cloud. We use two approaches for analyzing this anisotropic anomalous diffusion: a statistical and a spectral approach. In this chapter, we use nonextensive statistics to quantify the diffusion regime in the directions along and across the external electric field by calculating mean squared displacements and obtaining non-Maxwellian distribution fits to the histograms of dust displacements and velocities. In chapter 5, we quantify stochastic disorder for each dust cloud structure and use scaling relations between the nonextensive statistics and the fractional Laplacian to obtain input parameters for the

Fractional Laplacian Spectral Method. The predictions from the spectral approach are then compared against the observations of experiment to identify the characteristic spatial scales where transport is enhanced due to the combination of nonlocal and stochastic effects. This dissertation builds on the spectral work done in [12, 114, 115, 116] by providing the first validation of the FLSM against dusty plasma experimental data through direct scaling between the statistical and the spectral approach to anomalous diffusion.

Here we investigate nine pressure-current datasets from PK-4 experiments conducted in DC neon discharge. The negatively-charged dust particles are kept stationary in the field of view of the particle observation cameras by switching the polarity of an externally-applied electric field. As the frequency of the polarity switching (500Hz) is higher than the typical dust response frequency, the dust experiences net zero force due to the electric field. This, however, results in an anisotropy in the ion wakefields surrounding the dust, which in turn causes anisotropic dust interactions and diffusion. Particle tracking techniques [127] were used to obtain the dust positions and velocities from video data. The dust MSD, the displacement histograms, and the velocity histograms were reconstructed using a modified version of the open-sourced `@msdanalyzer` code [4]. Table 4.1 below provides a summary of the pressure-current conditions and dust density for each case.

Data Set	1	2	3	4	5	6	7	8	9
P [Pa]	28.5	28.5	28.5	46.1	46.1	46.1	70.5	70.5	70.5
I [mA]	0.35	0.7	1	0.35	0.7	1	0.35	0.7	1
n [mm^{-3}]	81.8	88	85.3	123.6	93.4	93.3	55.1	93.3	69.3

Table 4.1: Pressure, current, and dust density for each examined data set from the PK-4 experiments.

Fits to the MSDs plots reveal a non-linear relation with time delay τ^{α}, which is indicative of anomalous diffusion. Fits to both the position and velocity histograms for the direction along the external electric field are best described by a q-Gaussian distribution function,

where the non-extensive exponent q quantifies how the distribution deviates from a standard Gaussian or a Maxwellian one. The dust displacements and velocities in the direction perpendicular to the external electric field are best described by a Bi-q-Gaussian distribution, which is a sum of two q-Gaussian distributions. These findings suggest that these microgravity dusty plasma clouds exhibit anisotropic anomalous diffusion with distinct properties in the directions along and across the externally applied electric field. These anisotropies become more prominent as the neutral gas pressure is increased. As the neutral gas pressure in dusty plasma mediates the dust-neutral collisions, increasing pressure in these experiments acts as decreasing temperature, which is why the observed thermodynamics is sensitive to pressure changes. This was also seen by [**?**], which conducted a structural analysis of the same set of experiments using pair correlation function techniques. This paper confirmed that the anisotropies on the dust interaction potential also increase with pressure, leading to a structural transitions from an isotropic crystalline state to a liquid crystalline state. The remainder of this chapter is dedicated to the qualitative and quantitative description of the observed anisotropic anomalous diffusion and equilibrium properties of microgravity dusty plasma clouds in PK-4.

4.1 Experimental Setup

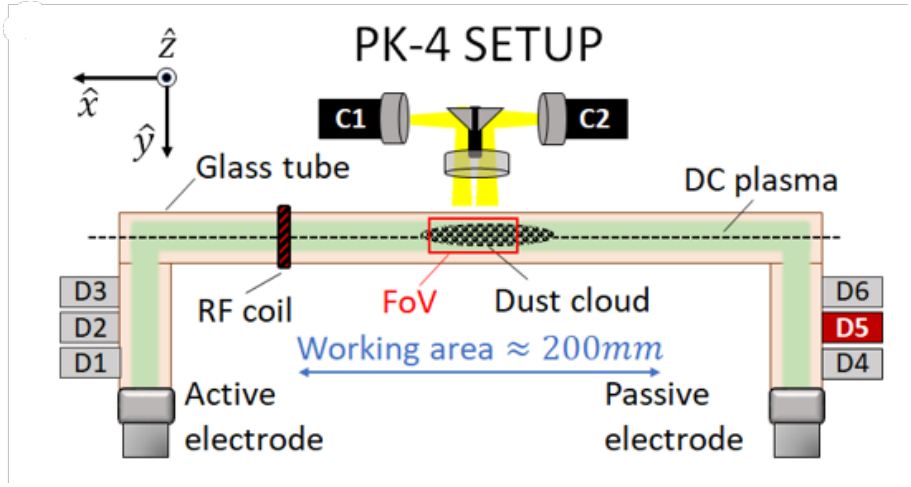

Figure 4.1: PK-4 Experimental Setup. Dust from Dispenser 5 (D5) is suspended in a DC neon discharge and trapped in the camera field of view using polarity switching of the DC electric field.

Here we briefly discuss the PK-4 experimental apparatus [117], and the specifics of the Campaign 7 (C7) data that were used for the analysis. The core of the PK-4 facility is comprised of an integrated baseplate housing the diverse components, including a glass plasma chamber with electrodes and microparticle dispensers (injecting melamine-formaldehyde dust spheres), vacuum and gas supply systems, plasma generation and diagnostic tools, microparticle manipulation devices, a microparticle observation system with cameras, and an illumination laser, see Figure 4.1. The main vacuum vessel is a cylindrical glass chamber, where plasma can be created using a direct current (DC) discharge power supply or using radio frequency (RF) coils. The present experiments were conducted in pure DC neon discharge. Polarity switching of the DC current at different frequencies and variable duty cycles can be used to transport the dust particles (using an asymmetric duty cycle) and capture them in the cameras field of view (FoV) (using a symmetric duty cycle). Several microparticle manipulation options and on-board plasma diagnostics, such as a plasma glow observation system and a mini spectrometer, are also available. Here we label the axial direction in PK-4

(x direction in Figure 4.1) as $\parallel$ since it is parallel to the direction of the dc electric field. The radial, or cross-field, direction in the camera's field of view (z direction in Figure 4.1) is labeled $\perp$.

The DC discharge plasma is generated by two electrodes within the π-shaped glass chamber. A custom-made bipolar high-voltage (HV) power supply serves as a current source, providing a stabilized output current of up to 3.1 mA at a maximal overall voltage of 2.7 kV. The current is regulated on the active side, with return current measurement on the passive side. Steady-state deviations from the set current value remain below 5%. When a symmetric duty cycle is used with a fast polarity switching of the current (500 Hz in the experiments analyzed here), the dust microparticles are unable to respond as the dust response frequency is close to 10 Hz. This results in overall stationary negatively charged microparticles suspended within a 'sloshing' stream of ions that form anisotropic ion wakefields surrounding the dust grains. The Particle Observation (PO) system facilitates microparticle imaging, employing a 532 nm diode laser and two PO cameras with CCD chips of 1600 px 1200 px. The cameras are movable and can cover the entire volume of the working area. The camera frame rate used in the present study is 70.1 fps, yielding 0.014 s time intervals in between successive frames.

The PK-4 Campaign 7 experiments discussed here were conducted on July 26, 2019. Our analysis uses the video data from nine sets of pressure-current conditions. The polarity switching frequency was 500 Hz with a duty cycle of 50%. The dust microparticles used were melamine formaldehyde spheres of diameter 3.38 μm. In each case, the dust cloud was allowed to settle for 50 s, after which a scan of the laser sheet was performed across the dust cloud (along the y-axis in Figure 4.1). These y-scans allow for obtaining information on the 3D structure of the cloud. The statistical analysis presented here uses particle tracking data collected over a period in which the dust cloud had settled. The cameras and laser sheet are focused on the mid-plane of the cloud. We use the dust particle positions and

velocities to study the probability distribution functions, anomalous diffusion, temperature, and nonequilibrium properties as a function of pressure-current conditions.

4.2 Analysis Techniques

In this section, we discuss the techniques used for the statistical analysis of PK-4 data. Those include particle tracking, drift subtraction, and techniques for fitting functions to MSD plots and velocity/displacement histograms reconstructed from experimental data.

4.2.1 Particle Tracking and Drift Subtraction

Here we consider PK-4 particle observation camera videos in which the laser sheet was fixed in the central region of the cloud for extended periods of time (about 20 s). The camera frame rate used was 71 fps resulting in a 0.014 s time step in between successive frames. The region of interest in the videos was a rectangular section in the center of each cloud with size 14 mm by 2 mm. The typical number of particles detected per frame was 470. This yields statistically significant datasets with $20,000$ data points or more in each set. The particle positions in the xz-plane were obtained using the open source particle tracking Mosaic Suite plugin of Fiji, which is a distribution of ImageJ [128]. The dust positions were converted from pixels to μm assuming a pixel resolution of 14.20 μm [117]. The particle trajectories imported from ImageJ include trajectories that do not start at the same time and do not last for the same duration. As shorter tracks can correspond to particles that move in and out of the plane illuminated by the laser sheet, we discarded tracks where the particles appear in fewer than 10 frames (or shorter than 0.14 s). The remaining trajectory data were used as inputs in the `@msdanalyzer` code to subtract drift, compute velocity autocorrelation functions and MSDs, and construct histograms of particle displacements and velocities. The nine pressure-current cases considered here use identical particle tracking datasets as those in [**?**], where the anisotropic structure of the PK-4 clouds was investigated using pair correlation analysis. Thus, we expect that the results obtained here and in [**?**] are directly comparable.

The open-sourced code `@msdanalyzer` [4] was used to analyze the data. The developers of `@msdanalyzer` also developed the Mosaic Suite in Fiji, providing good compatibility between the code and the particle tracking data to construct the MSD (with options to provide the standard deviation and check for localization error) and to create the histograms of dust displacements and velocities. The `@msdanalyzer` code was also used to calculate the velocity autocorrelation, detect directed motion, and subtract drift. Those steps were necessary to ensure that the statistical analysis is performed on the diffusion portion of the dust motion, subtracting the convective motion. In addition, motion along the direction of the external electric field E (the x-axis or the $\parallel -$ direction) is considered separately from motion across the direction of E (the z-axis or the $\perp -$ direction). This was necessary due to the anisotropic coupling of the dust particles discussed in [**?**].

Each PK-4 dataset used in our analysis was extracted from a large field of view, encompassing a large portion of the dust cloud. As a result, we could break up the field of view into smaller sections and calculate different drifts in different domains or sections of the cloud. This was necessary as nonhomogeneous drift was observed for several datasets. To address this issue, a method of nonhomogeneous drift subtraction (NHDS) was developed. In this method, the large field of view is separated into 12 smaller regions, as shown in Figure 4.2 a), and homogeneous drift subtraction is performed for each region. The number of smaller regions was selected to balance accuracy in drift subtraction and reasonable computation times. The NHDS method was validated against cases where the normal homogeneous drift subtraction worked, such as the case at 70 Pa pressure and 0.7 mA dc current. We found the two methods produced show agreement for uniform drift, but NHDS is much more successful in the nonhomogeneous drift case.

Figure 4.2 shows the case where the most pronounced nonhomogeneous drift was observed for 70 Pa pressure and 0.35 mA dc current. As can be seen in Figure 4.2 b), in the presence of nonhomogeneous drift, applying the drift subtraction to the large region of interest produces particle trajectories that exhibit some coordinated motion (instead of

showing random diffusive motion). The NHDS method seems to work better as shown in 4.2 c), though some small areas still exhibit coordinated motion instead of the desired diffusive behavior. The drifts for each smaller domain region are shown in 4.2 d). While the total drift simply implied that the dust particles were linearly drifting to the left, the domain drifts show a spread of drift directions.

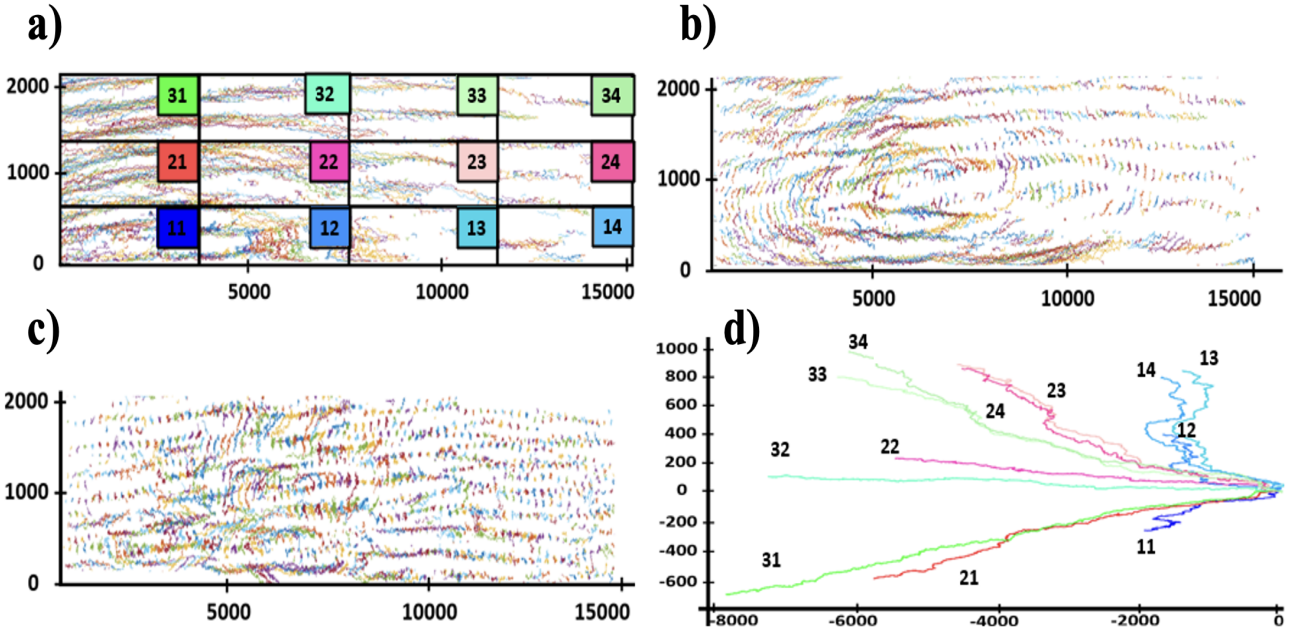

Figure 4.2: a) Dust particle tracks (μm) found using `@msdanalyzer` broken into 12 domains. a) Dust tracks (μm) after normal drift subtraction. c) Dust tracks (μm) after nonhomogeneous drift subtraction (NHDS). d) Average drift trajectories found in each domain in a). Experimental conditions were 70 Pa neutral gas pressure and 0.35 mA DC current.

As a quantitative check of the NHDS application of drift correction for the 70 Pa 0.35 mA case, we calculated the velocity autocorrelation of all domains before and after, shown in Figure 4.3. While the velocity autocorrelation before subtraction (red) showed a nonzero value, after the NHDS subtraction (blue), the total autocorrelation dropped to zero. Using these drift-subtracted particle trajectories, we proceeded to find the values of α from a fit to the MHD plots and the values of q_p and q_v from fits to the position and velocity histograms.

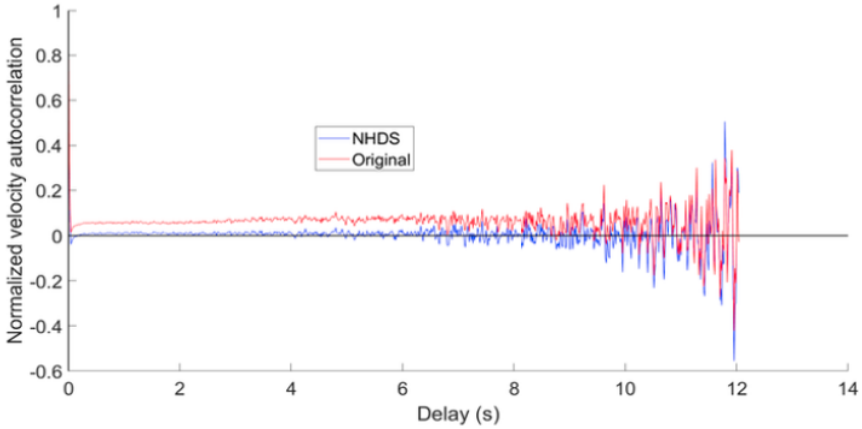

Figure 4.3: Velocity autocorrelation function calculated for the 70 Pa, 0.35 mA case before drift subtraction (red) and after NHDS (blue).

4.2.2 Fitting Techniques

In-house codes were developed to obtain nonlinear fits to the MSDs at different time delay intervals τ and distribution fits to the histograms. Fits to the displacement and velocity histograms were obtained using a Maxwellian (Eq. 2.2.15), a single q-Gaussian, and a Bi-q-Gaussian distributions of the form

$$\frac{A}{\sqrt{\pi v_{th}^2}}\left[1+(q_v-1)\frac{(v-v_0)^2}{v_{th}^2}\right]^{\frac{-1}{q_v-1}} \qquad 1 \le q_v < 3 \tag{4.2.1}$$

$$\begin{aligned}&\frac{A}{\sqrt{\pi v_{th1}^2}}\left[1+(q_{v1}-1)\frac{(v-v_0)^2}{v_{th1}^2}\right]^{\frac{-1}{q_{v1}-1}} \\ &+\frac{A}{\sqrt{\pi v_{th2}^2}}\left[1+(q_{v2}-1)\frac{(v-v_0)^2}{v_{th2}^2}\right]^{\frac{-1}{q_{v2}-1}}\end{aligned} \qquad 1 \le q_{v1,v2} < 3. \tag{4.2.2}$$

Here A, v_{th}, v_0, and q are the fitting parameters for the velocity histograms. The fits to the position histograms used the same distributions where v_{th} was replaced by D and $(v-v_0)^2$ was replaced by $(r(\tau)-r_0)^2$. To minimize fitting errors, the normalization in Eq. 2.2.4 was set to 1 and the fitting function from Eq. 2.2.13 from [2] was used. Dropping this normalization has a negligible effect. For all cases, it was found that the axial component

of the velocities (displacements) is best approximated by a single q-Gaussian, while the radial component is best approximated by a Bi-q-Gaussian. The value of q found from the position and velocity histogram fits are denoted as q_p and q_v, respectively. Data obtained from particle displacements/velocities along the axial direction is labeled by a subscript $\|$, while cross-field direction data have a subscript $\perp$. The kinetic temperature was calculated from the velocity distribution function using the following equation

$$T = \frac{m}{3k_B}\int (v - v_0)^2 f(v) dv = \frac{m}{3k_B}\langle (v - v_0)^2 \rangle. \tag{4.2.3}$$

The distribution $f(v)$ is not assumed to be Maxwellian but is found from the velocity histogram fit in each case. Another (faster) way is to calculate temperature from the fitted variance which is proportional to the thermal velocity. Both methods were compared and the result was a small difference of a few Kelvin for the temperature fits. Once fits were performed and the temperatures were extracted from the q-Gaussian fits, Equation 2.2.14 was used to convert the q-temperature T_q to a Maxwellian-like temperature T_{Mq}. While this expression is formally valid for $q < 5/3$, no closed-form equivalent exists for $5/3 \leq q < 3$ due to the divergence of the theoretical variance in that range. However, in practice, the empirical histograms and fitted distributions retain finite variance within this interval. Therefore, for consistency and comparative purposes, we continue to apply Equation 2.2.14 as an effective approximation in these cases, while acknowledging the formal limitations of this extension.

4.3 Statistical Analysis Results

In this section, the MSD exponents α and nonextensive parameters q_p and q_v are given subscripts corresponding to the directions parallel and perpendicular to the electric field in the PK-4 experiment. The cross-field position histograms are best approximated by Bi-q-Gaussian with a mostly Gaussian "sub-population" ($q_{\perp 1} \approx 1$) and a 'halo-tail' ($q_{\perp 2} > 1$). Table 4.2 provides the fitted parameters α, q_p, and q_v quantifying anomalous dust diffusion

and nonequilibrium in the parallel and perpendicular direction for the different pressure-current cases.

Pressure-Current		$\alpha_{\parallel}$	$\alpha_{\perp}$	$q_{p\parallel}$	$q_{p\perp 1}$	$q_{p\perp 2}$	$q_{v\parallel}$	$q_{v\perp 1}$	$q_{v\perp 2}$
70 Pa	1 mA	2.01	1.05	1.81	1.40	1.60	1.14	1.20	2.21
	0.7 mA	1.68	1.13	1.70	0.98	1.25	1.13	1.30	1.63
	0.35 mA	2.05	1.45	1.55	0.96	1.38	1.17	1.23	1.38
46 Pa	1 mA	2.40	0.925	1.44	0.98	1.27	1.31	1.12	2.12
	0.7 mA	1.54	1.10	1.41	0.95	1.20	1.24	1.27	1.82
	0.35 mA	2.03	1.40	1.47	0.95	1.21	1.18	1.17	1.60
30 Pa	1 mA	1.68	1.18	1.33	0.99	1.22	1.41	1.22	2.10
	0.7 mA	1.50	1.04	1.25	0.94	1.28	1.28	1.11	2.31
	0.35 mA	1.67	0.88	1.34	1.07	1.10	1.23	1.19	1.60

Table 4.2: Values α from MSD, q_p from displacement histogram, and q_v from velocity histogram for each of the nine sets of pressure-current conditions.

Fits to MSD Plots

Figure 4.4 shows the MSD plots obtained from dust positions within a 2D plane for all cases after drift subtraction. A nonhomogeneous drift subtraction was necessary for the two of the cases: (70 Pa, 0.35 mA) and (46 Pa, 1 mA). For all three pressure regimes, the results indicate that the highest current (1 mA) leads to the largest slope of the MSD plots, suggesting an enhanced superdiffusive behavior (see dark red, dark blue, and dark green line on the plot). Normally, in the presence of linear drift in the dust motion, the MSD plot will resemble superdiffusivity. An increased DC current is expected to result in an increased electric field strength which would enhance the drift of all charged particles. However, in this case, the fast switching of the DC polarity should still prevent dust response. In addition, examination of the velocity autocorrelation suggests that drift has been successfully subtracted from the particles trajectories, leaving only random motion. Thus, it is likely that the enhanced superdiffusive trend is related to the effect that DC current has on the ion stream velocity, charge on the dust, and the resulting ion wakefield structure surrounding each dust particle.

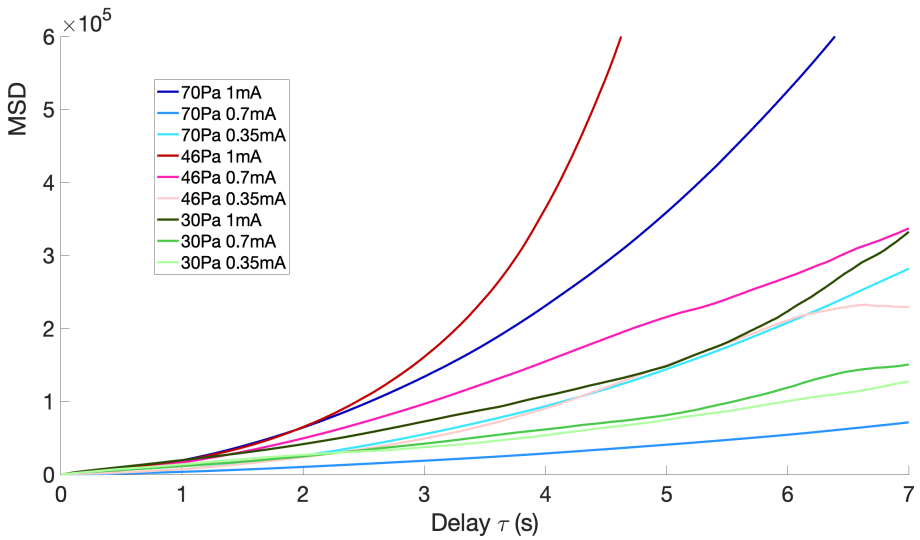

Figure 4.4: MSD plots for all cases after drift subtraction zoomed in to help distinguish different curves. The y-axis is the mean squared displacement ($\mu m/s$) and the x-axis is time delay in seconds.

To better understand the role of directional anisotropy, we calculated MSDs from particle displacements along $\parallel$ and across $\perp$ the direction of the external electric field. Separate fits were performed at different time delays to assess the role of distinct physical processes. Only data corresponding to time delays smaller than $10s$ was used for the fits. At larger time delays, the standard deviation from the mean MSD increases considerably due to decreasing number of data points. Figure 4.5 shows representative plots of $MSD_{\parallel}$ and $MSD_{\perp}$ for the 70Pa, 1mA case. For all pressure-current conditions the $MSD_{\parallel}$ has a magnitude much greater than $MSD_{\perp}$ and the plots of $MSD_{\parallel}$ look almost identical to those of the combined MSDs in Figure 4.4. The $MSD_{\parallel}$ for all conditions has a positive concavity at all time delays, suggesting superdiffusion. The one exception is the (30 Pa, 0.35 mA) case, which has a brief negative concavity at its start. This dataset had the most noisy trajectories and the least number of data points at long time delays. Thus, the deviation in observed behavior may be due to the poorer quality of the data. The $MSD_{\perp}$ for all cases exhibits a brief negative concavity for a delay period of about two seconds, followed by a positive concavity at lager time scales. This suggests that there may be a trapping mechanism causing sub-diffusive behavior at time scales smaller than $2s$. These effects are showcased in the plots in Fig 4.5.

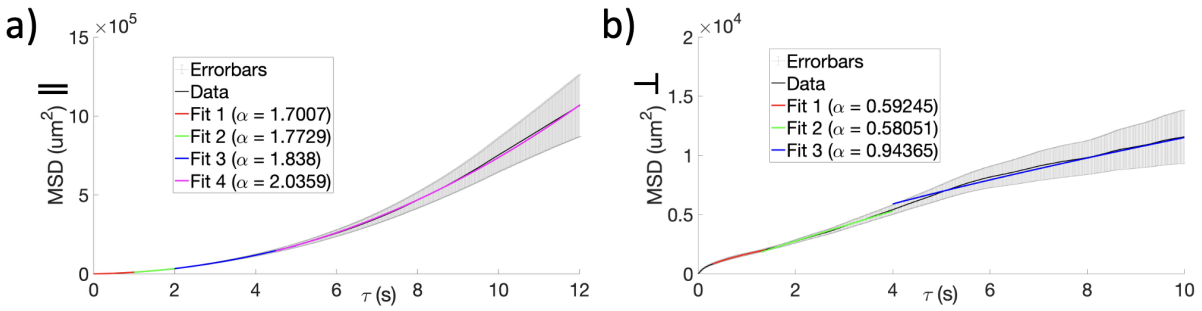

Figure 4.5: Fits to mean square displacement for different time delays for the 70Pa, 1mA case. a) MSD plot representative of the axial motion and b) MSD plot representative of the radial motion. The scale of the y axis differ by an order of magnitude between a) and b). This shows that most of the diffusion is dominated by the axial direction.

Figure 4.5 is representative of the MSD curves in the parallel and perpendicular directions across all the pressure-current cases. Key features to notice are the larger y-axis scale for the parallel case, the distinct superdiffusive $\alpha > 1$ curve for the parallel direction, and the transition from subdiffusive $\alpha < 1$ for $0.1 < \tau < 1$ to linear shape $\alpha \approx 1$ for $\tau > 5$ for the perpendicular direction. These are consistent across all pressure-current cases.

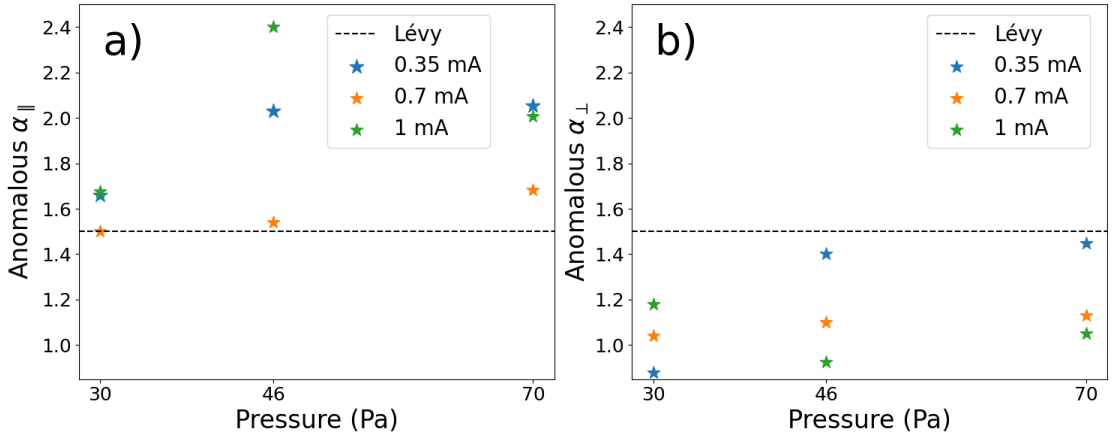

Figure 4.6: $\alpha_{\parallel}$ and $\alpha_{\perp}$ at time delay between 4 s and 5 s for all pressure-current cases.

The exponent α extracted from $MSD_{\parallel}$ and $MSD_{\perp}$ at time delay between 4 s and 5 s is plotted for all cases in Figure 4.6. This time period was chosen as it has the most consistent slope fitting while not being too short of a time delay. Recall that Tsallis' theory claims that the diffusion is a Lévy process when $q > 5/3$. Using the scaling relation $MSD = \langle r^2 \rangle \propto \tau^{\frac{2}{3-q_p}}$

[2] yields the criterion $\alpha > 3/2$ for a Lévy process. Note that this scaling is valid only for q_p obtained from the displacement distributions. A dashed line on Figure 4.6 marks the location of $\alpha = 3/2$, indicating that almost all distributions for the parallel cases are a Lévy processes, while the perpendicular direction are not. Later we compare these values of α to that found from the q_p values.

Fits to Displacement Histograms

Representative histograms of the displacements are shown in Figure 4.7 for 70 Pa, 0.7 mA case. The histograms of displacements parallel to the electric field are best approximated by a single q-Gaussian distribution, while the histograms of cross-field displacements are best approximated by a Bi-q-Gaussian distribution in most cases. These are displacements of all particles at time delay $\tau = 5$. The directional dependence of the distributions type implies anisotropic diffusion. The nonextensive q_p parameters extracted from the displacement histograms are plotted in Figure 4.8.

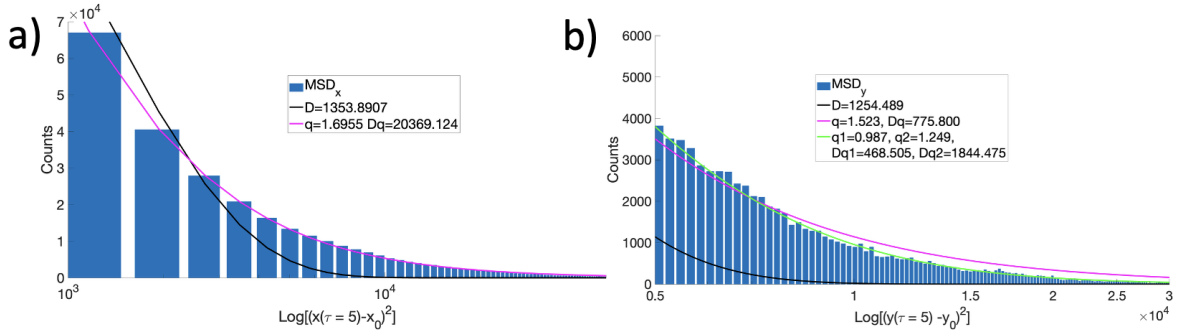

Figure 4.7: Position distribution fit example from case 70 Pa, 0.7 mA for displacements in a) parallel direction and b) cross-field direction plotted in logarithmic scale and shifted horizontally to accentuate the difference in tail behavior. The data for the position distributions is the positive squared value of $(r(\tau) - r_0)^2$. Since the data of $(r(\tau) - r_0)^2$ is already squared we fit it to a q-exponential instead of a q-Gaussian.

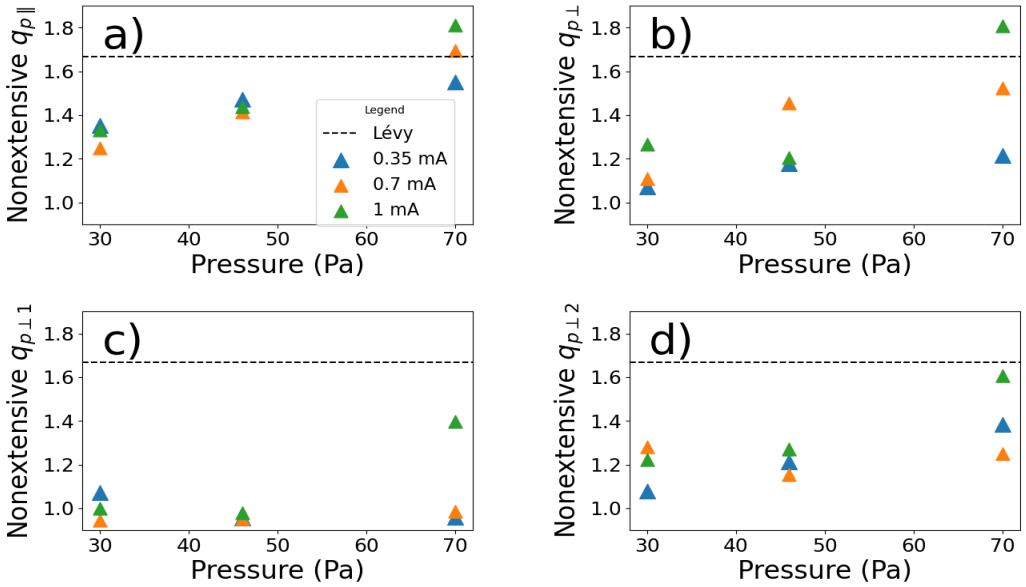

Figure 4.8: Coefficients extracted from nonextensive q_p fits: a) parallel $q_{p\parallel}$, b) perpendicular single q-Gaussian $q_{p\perp}$, c) perpendicular from Bi-q-Gaussian with Gaussian-like subpopulation $q_{p\perp 1}$, and d) perpendicular 'tail-halo' $q_{p\perp 2}$.

Notice that the coefficients for the parallel direction are again larger than for the perpendicular direction. Dashed line indicates a Lévy process. The coefficients extracted from the histogram of parallel displacements suggest that two of the 70 Pa cases are consistent with a Lévy process. A crossover to a Lévy process is also seen for the cross-field direction in the 70 Pa, 1 mA case if a single q-Gaussian is fitted to the histogram of cross-field displacements. However, the more accurate Bi-q-Gaussian fit to the cross-field displacement histograms suggest that the process is likely superdiffusive but not Lévy. These results are in qualitative agreement with the conclusions drown from the α coefficients extracted from the MSD fits at time delay $\tau = 5$ shown in Figure 4.6. It seems that higher pressures create larger spread in the coefficients and exhibit a larger difference between the parallel and perpendicular directions suggesting a more pronounced anisotropic effect. The values for the diffusion coefficient $D\left(\frac{\mu m^2}{s}\right)$ are calculated using Eq. 2.2.14, since Eq. 2.2.14 fundamentally comes from how the variance change with q and here the diffusion coefficient is taking the

place of the variance in these fits. These are shown in Figure 4.9. Here we can see that, in the direction parallel to the field, an increase in pressure causes diffusion to increase. However, in the cross-field direction, the interpretation is less straightforward. $D_{\perp 1}$ and $D_{\perp}$ generally decrease with pressure with some exceptions. $D_{\perp 2}$ does not show a clear trend with pressure or current.

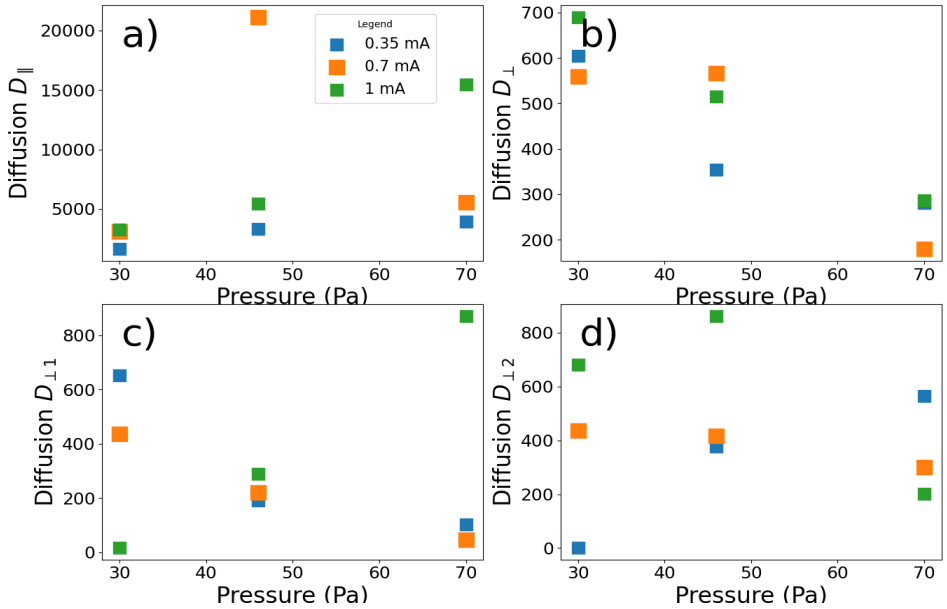

Figure 4.9: Diffusion coefficients ($\mu m^2/s$) obtained from fits to the displacement histogram using a q-Gaussian and a Bi-q-Gaussian for the directions a) parallel $D_{\parallel}$, b) perpendicular $D_{\perp}$, c) perpendicular from Gaussian-like sub-population $D_{\perp 1}$, and d) perpendicular from 'tail-halo' population $D_{\perp 2}$.

Next, we examined how the exponent α found directly from MSD fits compares to α calculated from the displacement histogram fits using the scaling relation in Eq. 2.2.5. Figure 4.10 shows the percent difference $\frac{\alpha_{MSD}-\alpha_{qp}}{\alpha_{qp}}$. We can see that, on average, the error is lower, indicated by the dashed line at 20%, for the cases where a Bi-q-Gaussian fit was used rather than a single q-Gaussian. This seems to be in agreement with findings from [8, 103].

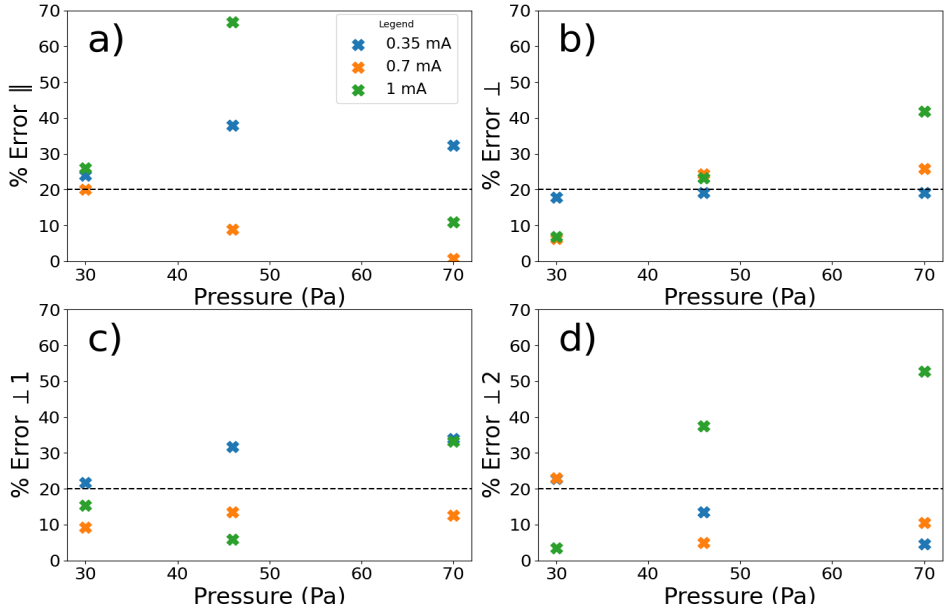

Figure 4.10: Percent difference between α found from MSD curves and α found from q_p using Eq. 2.2.5. a) parallel component, b) perpendicular component from a single q-Gaussian, c) Gaussian-like 'sub-population', and d) 'tail-halo'. A dashed line at 20% is used to help compare the figures.

Velocity Distribution Plots

Next we examine Figure 4.11, which shows representative histograms and distribution fits for the velocity components parallel and perpendicular to the direction of the external electric field. These plots show that a Gaussian or a Maxwellian distribution (black line) does not approximate the 'fat' tails of the histograms, while a q-Gaussian (magenta line) and a Bi-q-Gaussian (green line) provide good fits to the $\parallel$ and the $\perp$ velocity histograms, respectively. It is again observed that the distribution features change substantially with direction, suggesting anisotropic dust diffusion caused by the external electric field. Similar to the displacement data, we observe that the velocity histograms in the cross-field direction are best approximated by a Bi-q-Gaussian fit, suggesting a superposition of two distinct diffusion processes. These trends in histogram shapes are observed for all pressure-current cases. This will be further discussed in Sec. 4.4.2.

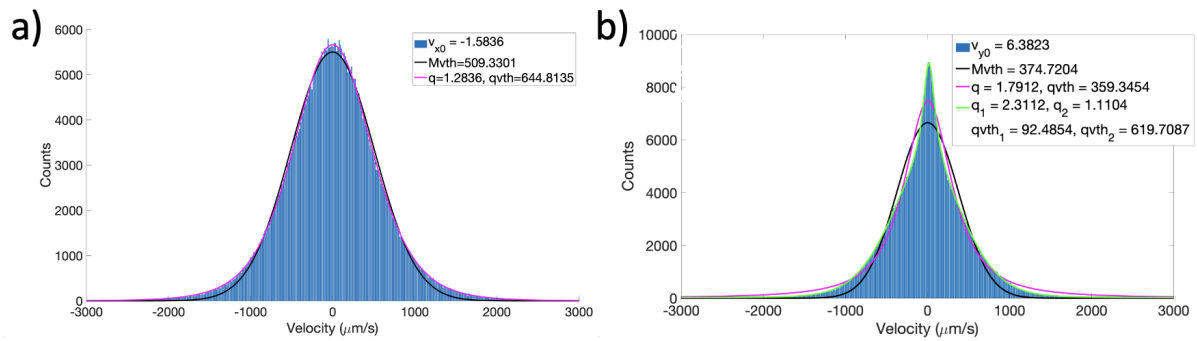

Figure 4.11: Velocity component histograms and distribution fits for the 30 Pa, 0.7mA case. a) Velocity components along the direction of the electric field. b) Velocity components in the cross-field direction.

Figure 4.12 shows the parallel and perpendicular nonextensive q parameters obtained from the velocity histograms for each pressure-current case. A slight negative slope is observed for increasing pressure for $q_{v\parallel}$ and none of the coefficients are above the $q \geq 5/3$ 'Lévy' or suprathermal line. The single q-Gaussian fits for the cross field velocity histograms had an $R^2 = 0.973$ and a normalized root mean square error $NRMSE = 0.027$ while the Bi-q-Gaussian fit had $R^2 = 0.993$ and $NRMSE = 0.013$. A larger value of R^2 and lower value of $NRMSE$ imply better fit thus the single q-Gaussian fits for the cross field velocity histograms are not as representative of the system as the Bi-q-Gaussian fits. With the Bi-q-Gaussian fits, the $q_{\perp 1}$ values show little change with plasma conditions (most of them are $q_{v\perp 1} \approx 1.2$), while $q_{v\perp 2}$ values seem to decrease with increasing pressure, except for the 1 mA case. The parameter q_v provides information on the equilibrium of the system, suggesting that in the direction parallel to the electric field, the dust ensemble is closer to an equilibrium as seen in Figure4.12 a), despite the strong superdiffusion observed in Figure 4.8 a).The trends in the cross-field direction are opposite, suggesting that the identification of the two distinct diffusion patterns drive the system away from equilibrium. This will be further discussed in Sec. 4.4.3.

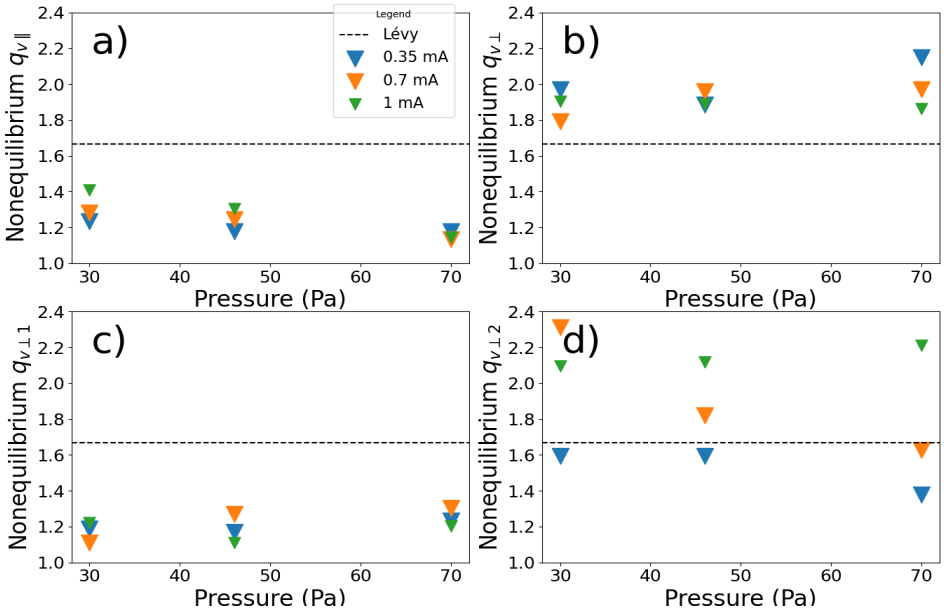

Figure 4.12: Nonequilibrium coefficients for all pressure-current cases obtained from fits to the velocity histograms using a q-Gaussian and a Bi-q-Gaussian for the directions a) parallel $q_{v\parallel}$, b) perpendicular $q_{v_\perp}$, c) perpendicular from Gaussian-like sub-population $q_{v_\perp 1}$, and d) perpendicular from 'tail-halo' population $q_{v_\perp 2}$.

The velocity distribution fits were used to extract dust temperatures for the directions parallel and perpendicular to the electric field. Figures 4.13 and 4.14 show the temperatures found using a Maxwellian fit, and a q-Gaussian fit, respectively.

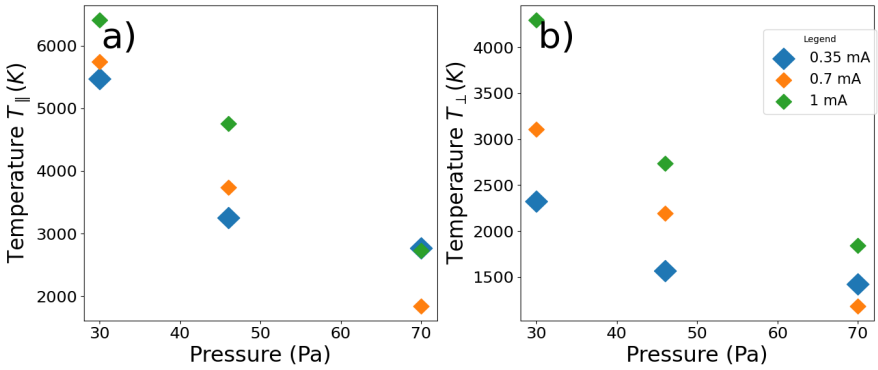

Figure 4.13: Temperatures for all pressure-current cases found using a Maxwellian fit to the a) parallel and b) perpendicular components of the velocity histograms.

Kinetic temperature is typically defined as the variance of a Maxwellian distribution. Since the velocity histograms for the dust in the PK-4 experiment are best approximated

by a non-Maxwellian, the notion of "temperature" here is not well defined. The range of kinetic temperatures found from the Maxwellian fits (Figure 4.13) is $2000K - 6500K$, or about $0.2eV - 0.6eV$, suggesting that the majority of the dust particles have very high kinetic energy even though the experiment is at room temperature and the plasma is collisional due to the neutral atom background. Anomalously high dust temperature is a known phenomena that is caused by electrostatic fluctuations [129]. In Figure 4.14, we used Eq. 2.2.14, $T_q(\frac{5q-3}{2}) = T_{Mq}$ (from [18]), since it provides a relation between the temperature or thermal velocity found from a q-Gaussian and a 'Maxwellian-like' temperature.

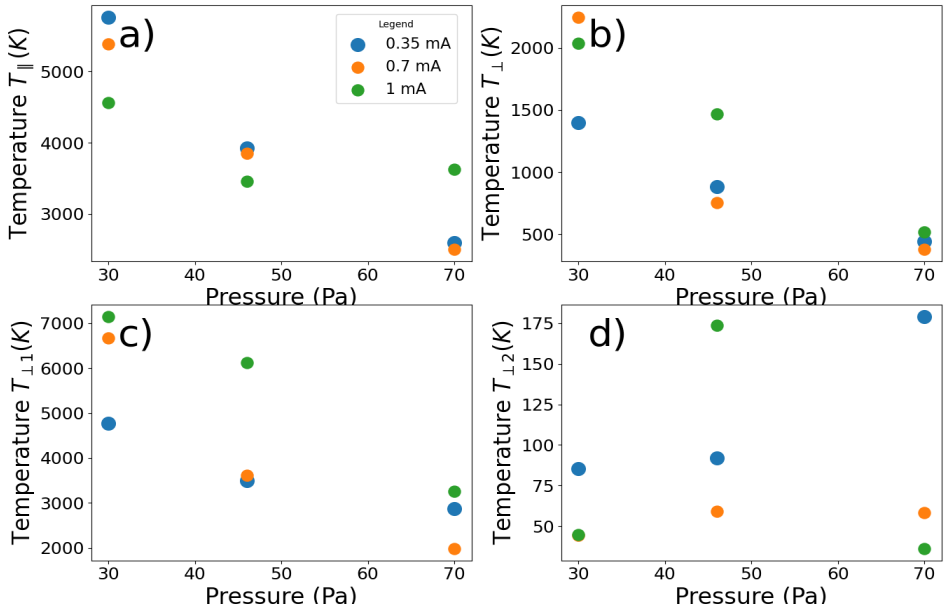

Figure 4.14: Temperatures T_{Mq} for all pressure-current cases found using non-Maxwellian fits to the parallel and perpendicular components of the velocity histograms. Temperature in the parallel direction a) was obtained using a single q-Gaussian fit. Temperatures in the perpendicular direction was found using a q-Gaussian b) and a Bi-q-Gaussian with a Gaussian-like sub-population fit c) and perpendicular 'tail-halo' fit d).

As shown in Figure 4.11 b), the perpendicular velocity histograms are best approximated by a Bi-q-Gaussian fit, where the the bulk distribution (the one with the larger variance and smaller q_v value) more closely resembles a Gaussian and, thus, can be used to extract the thermal velocity. The second distribution in the Bi-q-Gaussian accounts for the "fat tails". Thus, in Figure 4.14, $T_{\perp 1}$ is extracted from a Gaussian-like sub-population distribution, while

$T_{\perp 2}$ is obtained from fitting to a 'tail-halo' distribution. It may seem unintuitive why the Gaussian sub-population would have higher temperature values, while the 'halo-tails' have lower temperature values. This will be discussed in 4.4.2. Essentially we convert a variance from a distribution which has some 'tailed-ness' to a variance which does not have any, so that we can use the same definition of temperature. We argue that this is not a different treatment of temperature in dusty plasma, but an attempt at calculating temperature more carefully with nonextensive statistics. This allows us to derive more accurate dust temperatures for the PK-4 dusty plasma with values in the range $2500K - 5500K$, or about $0.2eV - 0.5eV$, which is smaller than the typically calculated values of $10 - 300eV$ [129].

Finally, for velocity q-distributions, Jiulin and Haining [21, 22] have derived the following expression for q_v in terms of the thermophoretic force and the Lorentz force in the presence of both electric and magnetic fields

$$q_v = 1 - \frac{k_B}{e} \frac{\nabla T_s}{(\nabla \phi + \vec{v} \times \vec{B})}. \tag{4.3.1}$$

T_s is the temperature for each species: electron, ion, or dust. In the PK-4, there is no magnetic field, thus, $\vec{v} \times \vec{B} = 0$. In the absence of a temperature gradient, $q_v = 1$ and the system is in equilibrium, i.e., the velocity histograms should be best described by a Maxwell-Boltzmann distribution. Equation 4.3.1 has has not yet been verified against any experimental measurements, though we will give a qualitative argument for its possible credibility.

Domain Velocity Distribution Plots

Here we provide physical arguments why the Bi-q-Gaussian fit for the perpendicular histograms is needed. First, we consider the domain separation on Figure 4.2 a) which was made for the NHDS method and reconstruct the velocity histogram in each domain. Figure 4.15 shows the velocity distribution for domain 11 (dark blue in Figure 4.2 a) in both the parallel and perpendicular directions for from the 30 Pa, 0.7 mA case.

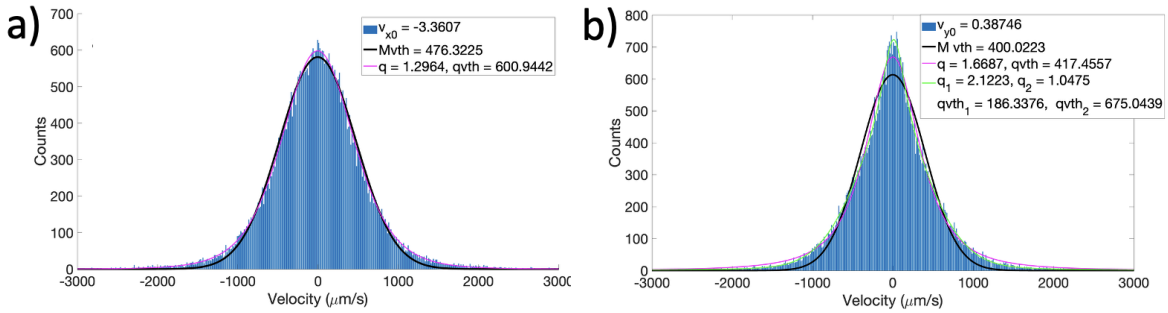

Figure 4.15: Velocity distributions for a) $\parallel$ and b) $\perp$ directions obtained from histogram fits of domain 11 for the case 30 Pa 0.7 mA. Notice that the q-Gaussian (magenta) curve provides a much closer fit than the one shown in Figure 4.11.

Although the Maxwellian fit still underpredicts the tails of the distribution, the single q-Gaussian fits the perpendicular histogram data much more closely than in Figure 4.11, though the Bi-q-Gaussian is also a reasonable fit. This phenomenon is apparent in all of the other domains and for all pressure cases with current $0.7mA$. Other current cases were not analyzed. We attribute these differences to the transition between local and global dynamics as the system size increases. The nonextensive Tsallis parameter can be used to assess the nonequilibrium state of the system with equilibrium represented by $q = 1$ and nonequilibrium by $q \neq 1$. The different local domains in a system may be more or less in equilibrium depending on the properties of the corresponding local distribution functions. As the sample of velocities used to create the histogram is increased to include multiple domains with varying equilibrium properties, the conclusions about global diffusion and thermodynamics may be significantly altered by the averaging process. A smaller domain size is more likely to provide accurate information on the nonextensive parameter q_v, whether the particles in the small region are in equilibrium or not. Of course, this requires that the number of data points in the smaller domain is sufficient to yield statistically significant results. Table 4.3 provides the values of all the nonequilibrium q_v parameters in each domain with each table entry representing the domain location in the field of view of the particle tracks, (Figure 4.2 a). This yields a spatial map of the equilibrium properties at different pressure of the PK-4

dust cloud. Table 4.3 shows that regions near the outer part of the dust cloud are typically further away from equilibrium than regions within the central region.

Nonequilibrium $q_{v\perp}$ in each domain

1.57	1.63	1.47	1.45
1.51	1.51	1.45	1.44
1.66	1.71	1.79	1.55

30 Pa 0.7 mA

1.98	2.05	2.01	1.83
1.63	1.68	1.68	1.58
1.63	1.66	1.62	1.60

46 Pa 0.7 mA

1.57	1.63	1.47	1.45
1.51	1.51	1.45	1.44
1.66	1.71	1.79	1.55

70 Pa 0.7 mA

4.3: The three tables show q_v placed in the table at the corresponding domain showing a spatial map of the equilibrium.

We use these domain q-Gaussian fits to calculate temperature in each domain using Eq. 2.2.14. Figure 4.16 a) $T_{\|}$ and b) $T_{\perp}$ show temperatures in units of Kelvin for 20 domains calculated for the 30 Pa 0.7 mA case. Each domain contained about 500 dust tracks, a minimum of 10 time frames per trajectory, which yields statistically significant amount of data for the velocity fits. The data indicates that temperature gradients exist in the PK4 clouds. As seen from Eq. 4.3.1, the temperature gradient and and the gradient in potential are related through the q_v parameter. Molecular dynamics (MD) simulations of ions and dust in the PK-4, with conditions closely resembling the 70 Pa 0.7 mA case, have previously demonstrated gradients in the electric potential surrounding each dust particles, as shown in Figure 4.17 [125]. Examination of Figures 4.16 and 4.17 suggests that the dust clouds in PK-4 exhibit both temperature and electric potential gradients, in addition to q-Gaussian velocity distribution functions. This provides a qualitative argument for applying Eq. 4.2.2, which is dependent on the ratio of the thermophoretic force over the electric field force. Providing a quantitative validation for Eq. 4.3.1 is beyond the scope of the present study and will be explored in future work.

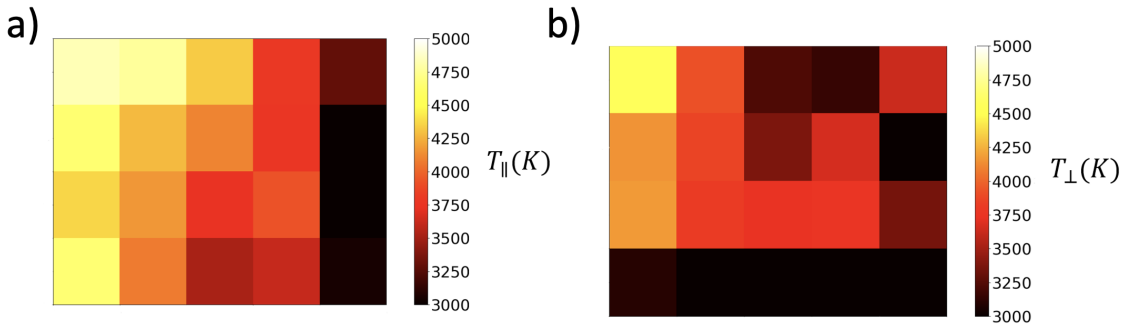

Figure 4.16: (a) $T_{\parallel}$ and (b) $T_{\perp}$ calculated in each domain showing temperature gradients for the 30 Pa, 0.7 mA case.

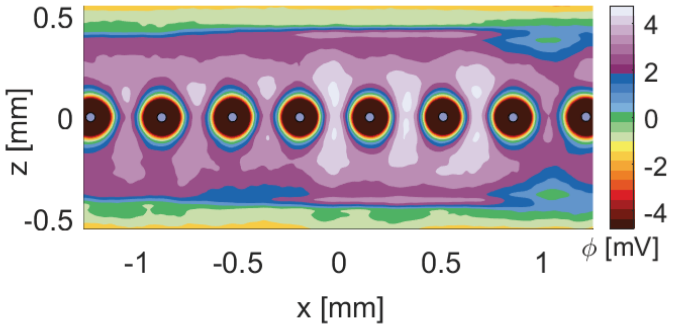

Figure 4.17: Electric potential in the vicinity of dust particles calculated by the DRIAD simulation. The simulation conditions closely reflect the 70 Pa, 0.7 mA case.

4.4 Statistical Analysis Discussion

In this section, we compare of anomalous diffusion determined from fits to the MSD plots versus fits to the displacement histograms. We further discuss the possible physical mechanisms leading to the anisotropy observed when comparing the displacement and velocity distributions in the directions parallel and perpendicular to the electric field. Finally, we consider the nonequilibrium temperatures found from the velocity distribution fits.

4.4.1 MSD and Displacement Histograms

When analyzing the MSD plots fitting (Figure 4.6), it seems like both $\alpha_{\parallel}$ and $\alpha_{\perp}$ increase with pressure for dc currents 0.35 mA and 0.7 mA. The trends are less obvious at 1 mA. These

fits also indicate that none of the extracted $\alpha_\perp$ exponents correspond to a Lévy process, while all data for $\alpha_\parallel$ suggest a Lévy processes. Meanwhile, the q_p coefficients extracted from the position histogram fits (Figure 4.8) also suggest that $q_{p\parallel}$ increases with pressure (i.e., enhanced superdiffusion), in agreement with the $\alpha_\parallel$ trends. However, only the highest pressure-currents case (70 Pa, 1 mA) in Figure 4.8 indicates a Lévy processes (i.e., $q > 5/3$). The $q_{p\perp}$ values extracted from single q-Gaussian fits show similar trends for the same currents as $\alpha_\perp$ but the 70 Pa, 1 mA case suggests a Lévy process, unlike $\alpha_\perp$. The Bi-q-Gaussian fits yield $q_{p\perp 2}$ values that exhibit closer similarity to the $\alpha_\perp$ trends. We can also see from Figure 4.10 that the fits for $q_{p\perp 2}$ and $q_{p\perp 1}$ yield lower percent error between the predicted and measured $\alpha_\perp$, strengthening the argument that the Bi-q-Gaussian is a more appropriate fit. The calculated diffusion constants (Figure 4.9) show an overall increase in parallel diffusion with pressure, while the perpendicular diffusion seems to decrease with pressure when a single q-Gaussian fit is used. These trends are not as clear for $D_{\perp 1}$ and $D_{\perp 2}$ which were obtained from a Bi-q-Gaussian fit. Both the MSD fits and the displacement histogram fits indicate a pronounced difference in the diffusion regime when comparing the direction along the electric field versus the cross-field direction, which can be attributed to an anisotropy in the ion wake-mediated dust-dust interaction potential.

The statistical analysis suggests that at high pressure-current conditions, a transition from superdiffusion to a Lévy process is expected in the axial direction. In the cross-field direction, the Bi-q-Gaussian fits suggest that the observed behavior is a superposition of a classical diffusion and superdiffusion, but no crossover to Lévy process is expected. These observations can be explained when considering the physical mechanisms causing the dust particles in the PK-4 experiments to organize into field-aligned filamentary structures. The alignment and the strong coupling of dust grains along the direction of the electric field is caused by enhancement of the ion wakefield focusing and elongation of the wakefield structure surrounding the dust grains (as discussed in [125]). The formation of positive space charge regions due to ion focusing will cause a negatively charged dust grain to drift locally towards

a nearby concentration of ions. This local drift is a nondeterministic microscopic effect, which is why it affects the microscopic motion by causing pronounced superdiffusion. The elongated ion wakefield structure surrounding the dust grains also causes a restoring force in the cross-field direction that keeps the individual dust particles aligned within the filament. This can explain the subdiffusive (or trapping) trends observed at small time scales in the cross-field MSD plots. Finally, if a dust particle escapes the confining potential that otherwise keeps it within a crystal-like filamentary structure, it cannot easily find force balance in between filaments. Instead, the dust particle makes large-scale jumps across the cloud until force balance is found within another filament. These jumps are frequently observed in video data from PK-4.

4.4.2 Histogram Shape in the Cross-field direction

Both the position and velocity histograms obtained for the $\perp$ direction (Figure 4.7, 4.11) were best fit by a bimodal distribution, i.e., the complex shape of the distribution can be viewed as a superposition of two simpler distributions. The single q-Gaussian which yielded the best results and fewest errors in the parallel direction, does not fit well in the perpendicular direction. We concluded that a Bi-q-Gaussian provided the best fit. Liu and Goree [103] showed that the dust velocity histogram in the PK-4 experiments with RF discharge can be described by what they called a Maxwellian 'core' and a Kappa distribution 'halo',

$$f_{M+\kappa}(v) = Ae^{\frac{-v^2}{v_t h^2}} + \frac{B}{(1+\frac{v^2}{\kappa v_{th}^2})^{\kappa}}. \tag{4.4.1}$$

Equation 4.4.1 is very similar to the Bi-q-Gaussian as the Maxwellian 'core' is recovered by setting $q = 1$ for one of the q-Gaussian distributions, while the Kappa 'halo' is identical to the q-distribution when one uses the known scaling relation $q = 1 + 1/\kappa$ in the other q-Gaussian. In addition, Liu and Goree concluded that the cloud exhibited liquid-like coupling as evidenced by the calculated pair correlation function. The dust cloud in these experiments was confined in RF plasma produced by an RF coil and the observed cloud

structure was homogeneous. In contrast, the present experiments were conducted in a pure DC discharge and the observed cloud structure was found to exhibit anisotropic coupling, suggesting both liquid and crystalline properties [?]. In both cases, the distributions consist of two terms, which implies a superposition of two distinct diffusion processes. Figure 4.18 shows a decomposition of the Bi-q-Gaussian into individual q-Gaussians.

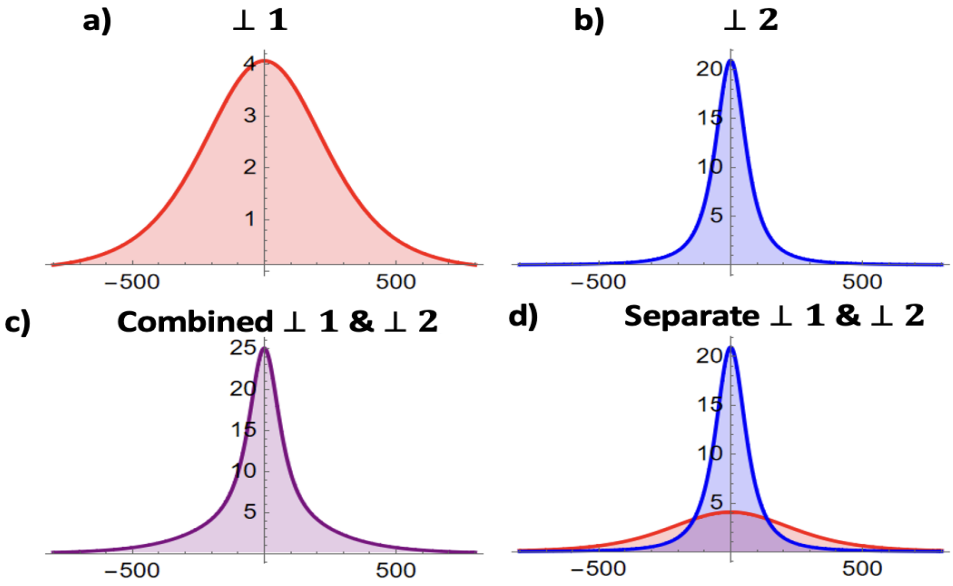

Figure 4.18: Components of the Bi-q-Gaussian illustrating two distinct populations: a) red $q_1 = 1.3$ and variance $\sigma_1 = 330$, while b) blue $q_2 = 1.63$ and $\sigma_2 = 63$. These are the same as the q_v values found for the cross-field velocity distribution in the 70 Pa, 0.7 mA case.

The superposition of the two q-Gaussian distributions shown in Figure 4.18 d) shows that one diffusion process (in red) is characterized by a small peak but large variance, while the other one (in blue) has both a large peak and large tails. The variance (and the corresponding temperature) of the blue distribution, however, is much smaller. Thus, the observed diffusion in the cross-field direction can be viewed as a superposition of two processes - one with higher temperature close to equilibrium and a second one with a lower temperature but farther from equilibrium.

This distribution shape is also called a 'knee and ankle' distribution, shown in Figure 4.19.

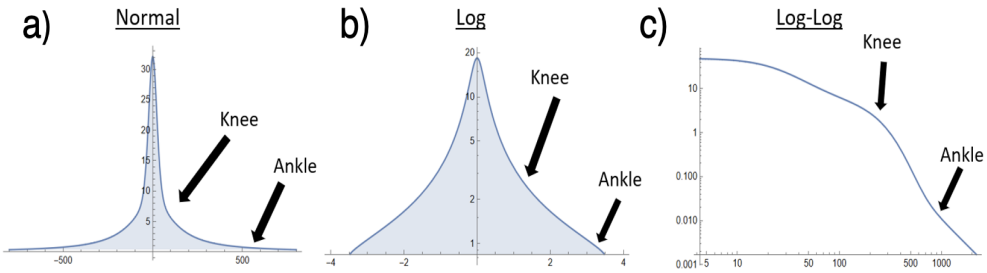

Figure 4.19: Analytical plot of the "knee and ankle" distribution a) with a normal axis, b) a log scale, and c) a log-log scale.

The 'knee and ankle' distribution has also been observed in solar wind ion and electron velocities and magnetic field fluctuations δB [70, 130, 131] as well as in fluxes of cosmic rays [132]. In [131], a bi-kappa distribution was proposed to explain the scale-dependent changes in the solar wind PDFs obtained from spacecraft measurements. It was pointed out that small scale PDFs are highly non-Maxwellian, while Maxwellian is recovered for large scales. In PK-4, the dust particles seem to exhibit similar disparity between small and large scales as evident from the distribution fits. As the dust diffusion is highly dependent on ion-wake-mediated interaction potential, small time fluctuations in the ion wakefield can be the reason for the highly non-Maxwellian features in the PDFs. Such fluctuations are expected to result from high-frequency ionization waves that were recently discovered in PK-4 [124].

In space physics, it is common to describe the non-Maxwellian velocity distributions using the kappa-distribution which is related to the q-Gaussian by $\kappa = \frac{1}{q-1}$. In [130], three physical mechanisms for generating a Kappa distribution were proposed: (i) Debye shielding, (ii) magnetic field biding, and (iii) temperature fluctuations. It was proposed that κ has a negative correlation with the Debye number N_D (number of particles in the Debye sphere). As κ is inversely related to q, we expect a positive correlation between N_D and q. In other words, increasing number of ions in the Debye spheres surrounding the dust should lead to enhancement of the superdiffusion. It was also proposed in [130] that κ is positively correlated with magnetic field fluctuations δB, which would imply negative correlation between q and

δB. While there is no magnetic field in PK-4, the charged dust particles are aligned to the external electric field. Thus, we conjecture that an increase in electric field fluctuations should randomize the dust motion, thus, leading to classical diffusion. Finally, the negative correlation between κ and the magnitude of temperature fluctuations δT^2 proposed in [130] suggests a positive correlation between q and δT^2. The role of temperature and temperature fluctuations in PK-4 will be further discussed int he next section. According to [133], the magnetic field fluctuations, δB, nearer the Sun around 6.9–9.7 AU, or even 43.6–47.2 AU, remain in a non-Gaussian, meta-equilibrium state. However, farther out between 80–87 AU, where the system has had more time ($\approx$ 1 year) to relax, the magnetic field fluctuations reach a Gaussian distribution suggesting an equilibrium in magnetic field fluctuations. In other words, at these distances the solar-wind relaxes back to an equilibrium after going through a transition in the diffusion regime from $q > 5/3$ to $q < 5/3$ between $\sim$ 47 AU and $\sim$ 80 AU. Similar nonequilibrium-to-equilibrium regime transitions can be explored more easily and cost-effectively in laboratory settings with a dusty plasma experiment.

4.4.3 VDFs and Temperature

As shown in Figure 4.14, temperature decreases with increasing pressure for $T_\parallel$ and $T_\perp 1$, aligning with the conclusions presented in [**?**], where it was seen that dust 'cooled off' due to the increased role in dust neutral collisions. The temperatures $T_\perp 2$, however, seem to show the opposite trend of increasing with increased pressure. The Tsallis coefficients $q_{v\parallel}$, never exhibit values greater than 5/3, which suggests that there is no Lévy processes for this direction. We also notice that $q_{v\parallel}$ tends to decrease with increasing pressure (thus, improving equilibrium), while increasing current slightly increases $q_{v\parallel}$ (thus, driving the system away from equilibrium). This is reasonable as an increase in pressure causes an increase in neutral collisions, meaning that the random collision process brings the dust motion to equilibrium. Meanwhile, the current provides an electric field which affects the ion streaming and focusing

surrounding the dust, which can cause local attractive interactions among dust particles and macroscopic regions of positive space charge.

While the coefficients $q_{v\perp}$ and $q_{v\perp 2}$ suggest Lévy processes, the trends are not as simple to interpret. To visualize this, we look at Figure 4.18 a), which shows a hot population, more so in equilibrium, while the cold, shown in blue, has much lower kinetic energy. This is most likely due to the trapping potential that creates the observed filamentary structures within the dust cloud. However, the blue population is far from equilibrium. This population is confined in the cross-field direction and much of its kinetic energy is in the parallel direction. When this energy transitions to the cross-field direction, it may do so suddenly, resulting in the larger tails of the distribution, or big jumps of the dust particles in space. In other words, Fig. 4.18 illustrates one population that is highly peaked with significant tails (kurtosis), giving a small variance (i.e., temperature), and another distinct population that exhibits high variance but less kurtosis. Based on this interpretation, increasing pressure appears to drive the first population $q_{\perp 1}$ away from equilibrium, while improving equilibrium for the second population $q_{\perp 2}$ for all but the 1 mA case. The confining forces keep the dust particles in a crystal-like structure, mostly aligned in the parallel direction, but these forces do not always succeed in maintaining this configuration. Similar to slipping out between tight tweezers, particles that escape these confining forces become energetic in the perpendicular direction. Once the particles escape, their movement is primarily dictated by the ion wakefield caused by the electric field, leading to increase in parallel diffusion. In other words, the forces confining the dust must act in the parallel direction; otherwise, the particles would accelerate due to the electric field.

An examination of the domain velocity distributions at 0.7 mA reveals that $q_{v\perp}$ tends to be higher on the edges of the cloud and smaller in the center at low pressure, but larger on the top and smaller on the bottom for the 46 Pa and 70 Pa pressure cases. We also see that for 30 Pa at 0.7 mA there exist clear gradients in both the $T_{\parallel}$ and $T_{\perp}$. (We remind the reader that there is only one $T_{\perp}$ here since a single q-Gaussian fits well the individual

domain data in the cross-field direction.) Unexpected high dust temperature has been a point of contention in the dusty plasma community because the experiments are always in a room temperature setting. This high dust temperature is better understood when considering all forms of energy in strongly coupled systems. We propose that, in addition to the kinetic temperature of the dust, the additional apparent energy comes from variation of the electrostatic potential. Typically one calculates temperature as $E = k_B T = 1/2 m v_{th}^2$. However, we propose $E + U = k_B T + Q_{dust} \langle \Delta \phi_{float}^2 \rangle$, meaning that room temperature of the dust particles can be recovered by employing the following expression

$$T = \frac{1}{2} \frac{m}{k_B} v_{th}^2 - \frac{e}{k_B} \langle N_{dust} \rangle \langle \Delta \phi_{float}^2 \rangle. \tag{4.4.2}$$

An order of magnitude calculation using this equation reveals that variation in the floating electric potential on the order of 10^{-5} Volts could explain this temperature discrepancy. This conclusion is explained more rigorously in [129].

4.4.4 Energy Dissipation

The energy dissipation and thermal state of PK-4 dusty plasma clouds was studied in detail by McCabe, et al. [134]. It was found that the onset of polarity switching of the electric field in PK-4 (used for trapping the cloud in the camera's field of view) causes an initial expansion in the dust cloud leading to an increase in thermal energy. Simulation results from that paper suggest that the onset of polarity switching causes a modification in the effective dust screening length due to reconfiguration of the dust during the expansion. The present work uses the same set of PK-4 experiments discussed in McCabe, et al., which allows for a meaningful comparison of results across the two studies. An important distinction is that McCabe, et al. used data obtained at and immediately after the onset of polarity switching, while the analysis here was performed on data collected later in the experiment. However, one of the main findings in McCabe, et al. is that an extended time (much greater than the Epstein drag decay) is required to dissipate thermal energy in these dusty plasma

clouds. Thus, it is reasonable to expect that the clouds do not have enough time to come to an equilibrium state for the duration of these experiments.

This is confirmed by the statistical analysis presented here. Specifically, the velocity distributions for all cases were found to be non-Maxwellian with high energy tails, which is evident from the $q_v > 1$ shown in Fig. 4.12. Here we further build on the study by McCabe et al. by identifying differences in the non-Maxwellian distributions obtained for velocities parallel versus perpendicular to the direction of the electric field. Parallel to the direction of the field, the $q_{v\parallel}$ values are only slightly greater than 1, which suggests that the thermalization, or energy dissipation, along this direction should be close to classical. However, in the perpendicular direction, the $q_{v\perp}$ values suggest a crossover from a superdiffusive to a Lévy process. In other words, a small sub-population of the particles has an order of magnitude higher energy than the bulk particles, which leads to inefficient energy dissipation. Physically, the polarity switching of the electric field causes a modification of the ion wakefield surrounding the dust grains, which in turn leads to the observed self-organization of the dust particles into field-aligned chains. If a dust particle escapes a chain, it is likely to experience big jumps in the cross-field direction until it finds force balance as part of another chain. These jumps are clearly observable in the video data.

In addition to the onset of polarity switching, changes in the discharge conditions are another mechanism that can cause anisotropic interaction potential and slow energy dissipation in the PK-4 dusty plasma clouds. Hartmann, et al. [135] used a 2D particle-in-cell with Monte Carlo collisions discharge simulation to investigate inhomogeneities in the PK-4 plasma. It was found that, on μs-scale, the structure of the positive column is characterized by the propagation of ionization waves. This prediction was experimentally validated in the PK-4 replica at Baylor University, though for pressure and current conditions slightly higher than those considered in this study. In the presence of ionization waves, the electric field and ion/electron densities can reach amplitudes up to 10 times larger than their average values with important implications to the ion-wakefield mediated dust-dust interaction potential.

Numerical work by Matthews, et al. [136] and Vermillion, et al. [125] showed that the propagation of ionization waves through the dust can modify the streaming velocity of ions and introduce time-dependent anisotropies in the ion wakefield structure surrounding each grain.

The statistical analysis conducted in this work provides quantitative experimental evidence for the presence of these anisotropies in the PK-4 ISS dusty plasmas. For all pressure-current conditions, the histogram shapes, nonextensive parameters q_p and q_v, diffusion coefficients, and temperatures show differences when calculated for the direction along the electric field versus the cross-field direction. In addition, this anisotropy on the diffusion seems to become more pronounced at higher pressures. This can be inferred from single distribution fits of the diffusion in Figure 4.9 a) and b) in the $0.35mA$ and the $1mA$ case, where $D_{\parallel}$ increases with pressure increase, while $D_{\perp}$ decreases with pressure increase. Physically, the general decrease in most diffusion values in the transverse direction at higher pressure coincides with the observation that the dust alignment in filaments longitudinally improves at higher pressure, which has been confirmed by calculating pair correlation functions [137]. As the filamentary structures form, the interparticle separation and coupling strength change with direction, which in turn changes the flow of thermal energy and energy dissipation in these clouds.

However, these trends are not exactly followed by the $0.7mA$ case, most notably, the $46.1Pa$ data point. While there may be particle tracking errors in the absolute particle positions data, we believe that the statistical treatment using position displacements and fits to histograms minimizes this source of errors. In addition, a measure of goodness of fit using R^2 and χ^2 normalized by degrees of freedom, for all cases, including the $46.1Pa, 0.7mA$, is typically around $R^2 \approx 0.99$ for both parallel (single q-Gaussian Figure 4.9 a)) and perpendicular (single q-Gaussian for Figure 4.9 b) and bi-q-Gaussian for Fig. 4.9 c) and d)) distribution fits. The parallel direction distribution fits have normalized $\chi^2 < 10^1$ while normalized $\chi^2 \approx 10^2$ for single q-Gaussian perpendicular fits and $\chi^2 \approx 10^1$ in the bi-q-Gaussian fits,

which is expected due to better fitting of the tail behavior. Thus, instead of fitting error, the probable source of the disagreement in the $46.1Pa$, $0.7mA$ data point is the difference in dust densities for different plasma conditions. Re-examination of the data from the PK-4 plasma glow camera reveals that for all currents the $46.1Pa$ experiments had one large cloud at the center of the discharge tube, while for the $28.5Pa$ and the $70.5Pa$ cases, there were multiple smaller dust clouds forming around plasma striations throughout the discharge tube. Since the number of particle dispenser shakes was kept constant, it is reasonable to expect that the difference in size and number of clouds will lead to a difference in dust density, which in turn, affects the calculated statistical properties. In a follow-up experiment (not discussed here), the plasma conditions were kept constant, while the dust density of the same cloud was varied through cloud compressions. These results will be a subject of a follow-up study.

It has been demonstrated numerically [136] that the formation of filamentary structures in PK-4 is enhanced by the presence of ionization waves. Since the PK-4 experiment on the ISS is not equipped with a high-speed video camera, we do not have direct experimental evidence that these ionization waves occur for all examined pressure-current conditions. However, the statistical analysis presented here provides a way to quantify the possible effect of ionization waves through the observed anisotropies in the dust diffusion. The present findings will benefit from comparison to further discharge simulations and experimental studies using the on-ground PK-4 replicas to better understand the parameter space where the ionization waves should be expected to dominate.

4.5 Statistical Analysis Conclusions

The presented analysis of of PK-4 dusty plasma experiments highlights the features of anomalous dust diffusion resulting from an interplay between temperature fluctuations and anisotropies in the dust-dust interaction potential caused by the application of external electric field to this strongly coupled complex system. Notably, we used non-extensive Tsallis statistics to quantify the nonequilibrium state of the system in the directions along and

across the electric field using q-Gaussian distributions. The nonequilibrium parameters q_p and q_v (extracted from position and velocity distributions) have distinctly different values for the directions parallel and perpendicular to the electric field, as shown in Table 4.2. Particle motion parallel to the electric field is superdiffusive and for several pressure-current cases, superdiffusion crosses over to a Lévy process. In the cross-field direction, the diffusion is again anomalous, but the bi-Gaussian fit best describing the histograms suggests a superposition of two processes. One of these processes is similar to classical diffusion, while the other one is superdiffusive, but not Lévy. We attribute the directional dependence of diffusion to anisotropies in the dust-dust interaction potential and fluctuations of the dust temperature throughout the cloud. The former is caused by the anisotropic shape of the ion wakefield clouds surrounding the dust grains, which leads to the alignment of the dust particles into filaments. Inside a filament, macroscopic regions of positive space charge form along the direction of the electric field due to ion focusing causing local dust accelerations towards these attractors. Similarly, the cross-field motion of the dust is restrained due to a restoring force from the streaming ions within the wakefield structure. However, if a dust particle escapes the filament, it will experience large jumps across the cloud until it finds force balance within another filament (which is visible in the video data). We hypothesize that the enhanced parallel diffusion causes more energy exchange between particles, thus bringing the system to equilibrium. This is seen by $q_{v\parallel}$ being only slightly greater than 1 while the parallel diffusion coefficient is large. Also, $q_{v\perp}$ is relatively greater than 1, while the perpendicular diffusion coefficient is much smaller. This is also supported by the trends that exist between the parallel diffusion and $q_{v\parallel}$ with increasing pressure, which are inversely proportional. The same is true of perpendicular diffusion and $q_{v\perp}$ also being inversely proportional, which may suggest that increased spatial diffusion contributes to increasing the equilibrium in velocity space.

In addition, the kinetic temperature is found to vary throughout the dust cloud as shown in Figure 4.16. Analysis of subdomains within the dust clouds reveals that a single

q-Gaussian fit works well even in the cross-field direction for small domain sizes. Since the q_v extracted from velocity histograms quantifies the nonequilibrium state of the system, the domain analysis allows for a nuanced understanding of cloud properties, including the structural anisotropy, diffusion, and equilibrium state. Specifically, we conclude that the different domains within the same dust cloud are characterized by different diffusion regimes driving the global state away from equilibrium. Temperature gradients were identified for the dust in the PK-4. While all the temperatures were higher than room temperature, we propose that the observed high kinetic temperature is due to electrostatic fluctuations. Finally, we conclude that dusty plasmas, such as those in PK-4, are excellent for studying nonequilibrium systems, anomalous diffusion and the physical origins of the two phenomena. As the mathematical description of these processes is universal, we expect that the dusty plasma experiments can be a practical means to investigate other nonequilibrium complex systems, such as the solar wind.

With the results obtained from this statistical analysis of PK-4 and with the connections made earlier in section 2.3 linking nonextensive statistics to the Fractional Laplacian Spectral Method (FLSM), we now move to the application of FLSM to the PK-4 experiment.

Chapter 5

Application of the Fractional Laplacian Spectral Method to Anisotropic Anomalous Diffusion in Microgravity Dusty Plasma

The Fractional Laplacian Spectral Method (FLSM) presented here is based on the extended states conjecture, first introduced by Liaw [3], and the series representation of the fractional Laplacian, derived by Padgett et al. [11, 138]. The physical interpretation of the spectral approach [115] and its application to transport in different disordered systems [114, 139, 140], including dusty plasma [116, 12], has been developed over the past decade. The core idea of applying the FLSM to dusty plasma is that the relationship between a given dust-dust interaction potential and the resulting global dust particle structure and dynamics can be inferred from the spectrum of the corresponding Hamiltonian operator. For a given interaction potential and plasma conditions, we will show how to define a corresponding Hamiltonian from quantities measurable in the experiments. Then, the time-evolved dynamics of the dust cloud evolving under the action of this Hamiltonian will be determined based on the collection of possible energy states, or the spectrum of the Hamiltonian. During a structural transition (in PK-4 data, the observed transition is from a homogeneous to a filamentary state), changes in the structure function and the correlation lengths within the system also yield changes in the corresponding energy spectrum and related transport properties. This approach originally been introduced in the condensed matter community, specifically, in the study of the metal-to-insulator transition in the Anderson localization problem [141, 142] and it forms the basis of the scaling theory of Anderson localization [143]. In this project, aim to expand the use of spectral theory to the study of anomalous diffusion in plasma. In

this chapter, we will show how to use the FLSM to quantify changes in the energy spectra for different structural states observed in the PK-4 dusty plasma experiments.

The key advantage of using such infinite-dimensional operators is the ability to study the available energy states for a system with given global characteristics without the need to know details of the local dynamics and without the need to impose boundary conditions [114, 115]. The main requirement for the validity of the proposed spectral method is to ensure that the experiment or the simulation yields enough data so that a meaningful statistical analysis can be used to inform the correct form of the corresponding Hamiltonian. Here, to fulfill this requirement, the input Hamiltonian will be informed from the PK-4 experiments, in which the number of particles in the dust cloud is large ($\approx 10^6$) and the experiments last over extended times ($\approx 20 - 30\ min$).

Earlier in section 4.3, statistical analysis of particle tracking data from 9 datasets from PK-4 experiments was performed. Each dataset represented a different combination of pressure-current conditions, which resulted in a different structural state of the dusty plasma cloud. Fits to the dust mean squared displacements (MSDs) and position histograms were used to obtain parameters that can be scaled as inputs for the Fractional Laplacian in FLSM. Table 4.5 shows the 9 pressure current datasets, along with the main fitted parameters - the MSD exponents α and the nonextensive parameter q_p. The nonextensive parameter q_p is chosen rather than q_v because it is the q parameter that provides the spatial information, such as the diffusion coefficients, and the fractional Laplacian is a spatial operator. With this information, using the scaling relations discussed in Sec.2, we can obtain the nonlocality parameter (fraction on the Laplacian) s_α and s_q from α and q_p, respectively in the directions parallel ($\|$) and perpendicular ($\perp$) to the electric field.

Pressure–Current		$\alpha_{\parallel}$	$\alpha_{\perp}$	$q_{p\parallel}$	$q_{p\perp 1}$	$q_{p\perp 2}$	$s_{\alpha\parallel}$	$s_{\alpha\perp}$	$s_{q\parallel}$	$s_{q\perp 1}$	$s_{q\perp 2}$
70 Pa	1 mA	2.01	1.05	1.81	1.40	1.60	0.498	0.952	0.482	0.800	0.700
	0.7 mA	1.68	1.13	1.70	0.98	1.25	0.595	0.885	0.647	1.010	0.875
	0.35 mA	2.05	1.45	1.55	0.96	1.38	0.488	0.690	0.725	1.020	0.810
46 Pa	1 mA	2.40	0.925	1.44	0.98	1.27	0.417	1.081	0.780	1.010	0.865
	0.7 mA	1.54	1.10	1.41	0.95	1.20	0.649	0.909	0.795	1.025	0.900
	0.35 mA	2.03	1.40	1.47	0.95	1.21	0.493	0.714	0.765	1.025	0.895
30 Pa	1 mA	1.68	1.18	1.33	0.99	1.22	0.595	0.847	0.835	1.005	0.890
	0.7 mA	1.50	1.04	1.25	0.94	1.28	0.667	0.962	0.875	1.030	0.860
	0.35 mA	1.67	0.88	1.34	1.07	1.10	0.599	1.136	0.830	0.965	0.950

5.1: Fitted and calculated parameters for the 9 pressure-current cases in the PK-4 experiments. The values of α and q were extracted from fits to MSD plots and position histograms, respectively. The values of s_α were calculated using the scaling relation $s_\alpha = 1/\alpha$. The values of s_q were extracted using the scaling relation $s_q = \frac{3-q}{2}$ if $q < \frac{5}{3}$ and $s_q = \frac{3-q}{2q-2}$ if $q \geq \frac{5}{3}$.

This provides a parameter space $0.4 < s < 1.2$ for the fractional Laplacian in the spectral calculations. The next step is to quantify the dimensionless disorder for each of the PK-4 pressure-current cases, which will provide the key input for the potential energy term of the Hamiltonian.

5.1 Disorder Parameter

To quantify the structural disorder for each dusty plasma cloud over time, we combined two complementary measures of disorder: a density-based disorder and an orientational disorder based on bond angles. The particle positions were obtained from video data using particle

tracking techniques and assuming camera pixel size of $dx = 14.20$ μm. This allowed for all spatial measurements, including sampling radii and inter-particle distances, to be computed in meaningful physical units. The density-based disorder was computed by sampling 60 randomly positioned circular windows around each particle. The center of each window was uniformly drawn from within a radial distance of $30dx$ (30 pixels) from the particle, and each window had a fixed radius of 30 pixels. This window radius was chosen to be sufficiently large to capture mesoscale fluctuations in particle concentration while remaining much smaller relative to the scale of the cloud, which extends over about 1000 pixels in the horizontal direction and about 150 pixels in the vertical direction. Within each window, we counted the number of neighboring particles and calculated the variance across all samples. This variance quantifies the local density inhomogeneity around each particle, with higher values indicating greater spatial disorder due to clustering or irregular voids. Formally, the density-based disorder for particle i is expressed as

$$c_i^{(\text{density})} = \text{Var}(N_1^{(i)}, N_2^{(i)}, \ldots, N_{60}^{(i)}), \tag{5.1.1}$$

where $N_j^{(i)}$ is the number of neighbors found in the j-th sample window around particle i.

Next, we evaluated the angular distribution of neighbors around each particle using the bond orientational order parameter G_6. In all cases, the filamentary structures in the dust clouds seemed to exhibit hexagonal alignment within the 2D plane of the illumination laser sheet, which is why G_6 was selected as appropriate orientational measure. For a given particle, we identified its six nearest neighbors using a KD-tree search and computed the angle θ_{ij} between the particle and each neighbor j. These angles were used to define the complex order parameter,

$$G_6(i) = \frac{1}{6}\sum_{j=1}^{6} e^{i6\theta_{ij}}, \tag{5.1.2}$$

which approaches a magnitude of 1 for a perfectly hexagonal (triangular lattice) configuration. We then defined the structure-based disorder as the deviation from perfect orientational

order:

$$c_i^{(\text{structure})} = 1 - |G_6(i)|. \tag{5.1.3}$$

The two disorder metrics were combined linearly using a tunable mixing parameter β,

$$c_i = \beta c_i^{(\text{density})} + (1 - \beta) c_i^{(\text{structure})} \tag{5.1.4}$$

with weight ($\beta = 0.6$) used in our analysis. We weight the density variation slightly more because of the filamentary structure of the PK-4 clouds where interparticle spacing and hexagonal alignment fluctuates with time.

To ensure comparability across frames and across experiments, we performed a global normalization of the combined disorder metric using fixed reference values. The minimum disorder value was obtained from a simulated hexagonal lattice with inter-particle spacing set to match the experimental average. The maximum disorder value was computed from a uniform random distribution of the same number of particles, generated within the same field of view. The final normalized disorder metric for each particle was defined as

$$c_i^{(\text{norm})} = \frac{c_i - c_{\min}}{c_{\max} - c_{\min}}, \tag{5.1.5}$$

which maps values to the interval $[0, 1]$, where 0 corresponds to perfect crystalline order and 1 to maximal disorder. To address occasional numerical instabilities, such as extremely large variance values due to sparsely populated regions or edge effects, we applied a correction step. Any disorder value exceeding a threshold (e.g., 0.5) was flagged as an outlier and replaced with a corrected value defined as 1.25 times the second-highest valid disorder in that frame. This ensured that rare pathological points did not distort color scales or skew statistical averages. All disorder values were visualized over time using color-mapped scatter plots with a consistent turbo colormap and fixed scaling. A representative scatter plot is shown in Figure 5.1. Additionally, the temporal evolution of the minimum, mean, and

maximum disorder across all frames was tracked to observe changes in the system's spatial organization, as shown in Figure 5.2. Overall, the tunable parameters were chosen so that the disorder map of the dust particle positions aligns with what is expected from observation. For example, particles in straight filaments should have a low disorder $\sim 10^{-5}$ while particles not aligned in filaments or particles that are visibly crowded together should have a higher disorder $\sim 10^{-1}$.

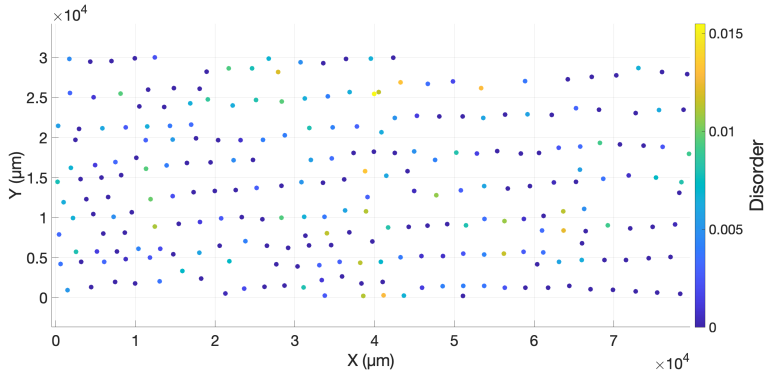

Figure 5.1: Disorder visualization at a single frame for the case of 70 Pa and 0.35 mA. Particle positions are color-coded by normalized disorder values.

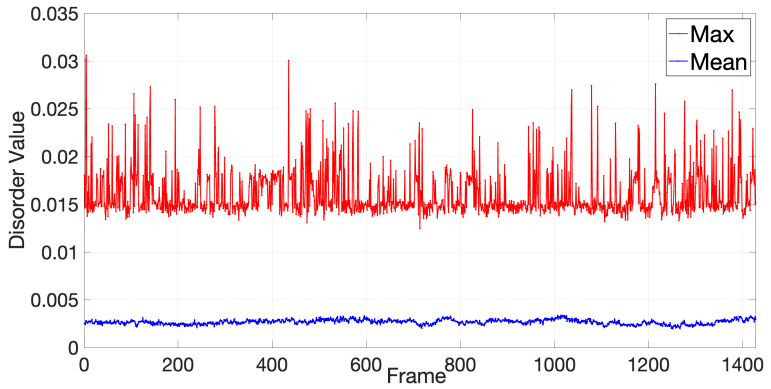

Figure 5.2: Temporal evolution of disorder across all frames for the case of 70 Pa and 0.35 mA. The plot shows the mean and maximum disorder per frame.

From the plot we see that the maximum disorder fluctuates much more than the mean disorder. This provides some information about the system dynamics suggesting that dust particles in disordered regions participate in large structural changes from one frame to the next.

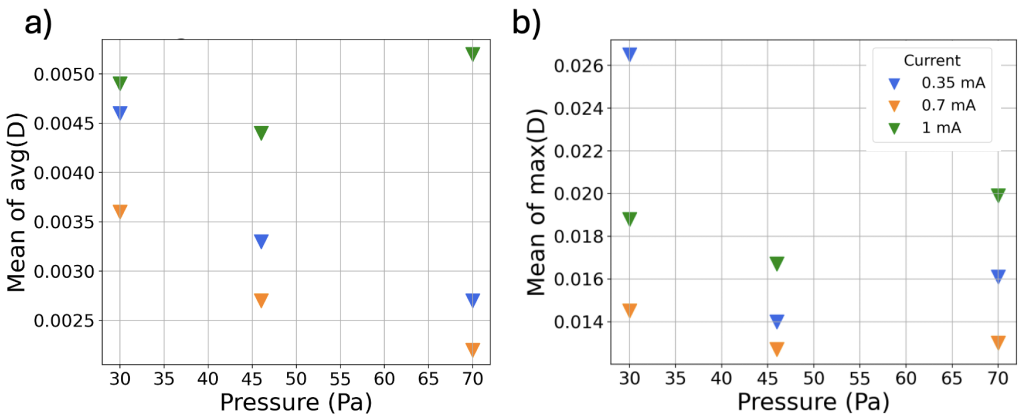

Figure 5.3: Disorder for all nine pressure and current conditions: (a) mean of the average disorder for all frames, and (b) mean of the max disorder for all frames.

We see that for most cases the mean disorder decreases with increasing pressure. This is also in agreement earlier in subsubsection 4.3 as the dust kinetic temperature was also found to decrease with increasing pressure. However, the maximum disorder shows a nonlinear relation with pressure, with minimum values at 46 Pa. As discussed in section 4.4, the cloud in the 46 Pa cases was larger, which results in higher dust densities. For that cloud, it can be expected that the outer layers of dust particles provide stronger confinement of particles in the interior, thus improving stability. The higher fluctuation of the maximum disorder in Figure 5.2 is also in agreement with subsubsection 4.3, where we discussed that, while the majority of the dust particles are in a stable configuration, there exists a subpopulation of particles with much higher energy as evident from the 'fat' tailed velocity distributions. These higher energy dust particles make big jumps across the cloud, which contribute to the maximum disorder over time.

5.2 Spatial Scaling

In the previous sections, we discussed how to obtain the fraction s on the Laplacian and the dimensionless disorder c, which are the two main inputs in the Fractional Laplacian Spectral Method (FLSM) 2.4.6. As mentioned previously, FLSM calculates whether a continuous

spectrum for a given Hamiltonian exists, which corresponds to the existence of extended energy states for the system described by that Hamiltonian. The FLSM calculation can be performed with respect to any reference vector ν in Hilbert space. The vector ν is a linear combination of the standard basis vectors δ_i from Eq. 2.4.1, and the number of basis functions can be varied. In other words, ν is simply a subspace of the Hilbert space and increasing the number of δ_i basis vectors used to define ν increases the size of the subspace. Mathematically, if continuous spectrum exists, performing the FLSM calculation with respect to subspaces of increasing size should always yield a nonzero value of the distance parameter in Eq. 2.4.6. Physically, if the distance parameter limits to a non-zero value with respect to some subspaces, but limits to zero at other scales, the system described by the Hamiltonian is expected to exhibit characteristic length scales of transport defined by the combined effects of nonlocality and disorder. In the PK-4 experiments, the characteristic scale of diffusive transport can be understood from the characteristic step-size displacement of the dust particle diffusion.

Historically, studying diffusion was performed in part by analyzing step-size displacement of the particles. This provides spatial information important to the dynamics of the system. For example, the microscopic dynamics are certainly going to be different for a system containing much larger scale displacements, like Lévy flights. Mathematically, Lévy flights are characterized as being scale-free and thus infinite in size. That is to say, there is not a rigorous observational way to define if a displacement is a Lévy flight based on a simple criterion such as, for example, the displacement being found to be ten times the average displacement or greater. However, in our experiments, the particles (and their jumps) are tracked at the kinetic level, which allows for some quantification of the characteristic step-size of particle diffusion and the identification of large jumps, even if they are not Lévy flights. Here we take a large portion of the dust particle tracks for each pressure-current case and find the average step size, the maximum step size, and a percentage of how many of the step sizes were ten times greater than the average.

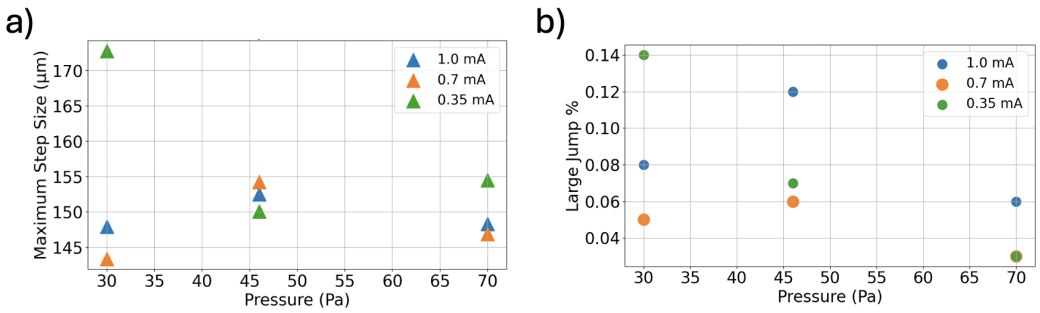

Figure 5.4: a) Maximum step-size for all pressure-current cases. b) Percentage of particle displacements that are ten times the average step-size for all pressure-current cases.

We found that, after drift motion was carefully subtracted from the dust trajectories, the average displacement in between two successive frames (frame rate $70.1fps$, yielding $\Delta t = 0.014s$) across the pressure-current cases was approximately one pixel or $14\mu m$. This is presumably due to background collisions or local electrostatic fluctuations. Due to both spatial and time resolution in these experiments, this is therefore the smallest spatial scale to observe. Figure 5.4 a) shows that the maximum particle displacements are slightly larger than ten times the average particle displacements. These are characterized as "large jumps" for the remainder of the dissertation. The percentage of "large jumps" in the system, as shown in Figure 5.4 b), is in the range 0.03% - 0.14% for all pressure-current cases, with overall higher numbers occurring at lower pressures. With around 440 particles in a frame and 1400 frames of data, this yields approximately 616,000 total displacements of which around 500 are "large jumps". Note that the video data clearly showed frequent instances of particles that make much larger jumps, on the order of $1mm$ or bigger, which resembles Lévy flights. However, those were omitted from the analysis due to difficulties in obtaining accurate tracks with the particle tracking software.

When breaking down the different scales of step-sizes (mean, large, and clustered), we saw that the $\parallel$-step-sizes tend to decrease more with increasing pressure than the $\perp$-step-sizes. This trend was strongest for the mean step-size (Pearson $r = -0.901$ for $\parallel$ vs. pressure, compared to $r = -0.765$ for $\perp$ vs. pressure). The trend persisted across the

large and clustered steps, though with decreasing magnitude and statistical significance. We also assessed whether large jumps exhibited a distinct directional bias by comparing the angular distributions of mean displacements and "large jump" displacements. The average angular orientation with respect to the direction of the electric field was 1.1° for mean displacements and 7.5° for large displacements. A two-sample t-test indicated a trend toward significance $p = 0.0837$, where the p-value reflects the probability of observing this result if no true difference exists, suggesting a modest directional shift. To verify this without assuming normality, we performed a Mann–Whitney U test, which yielded a comparable result ($p = 0.0729$). These results suggest that large jumps may be preferentially oriented cross field angles than typical displacements, though the evidence remains suggestive rather than conclusive. We also found that successive "large jump" occasionally take place. This is a scale larger than $150\mu m$ of dust displacements, where dust displacements on the order of the interparticle separation happen directly after a previous "large jump". This can be seen in the below plot which gives the percentage of "large jumps" that recently (within 10 frames) had another "large jump" happen. We call this a "cluster of large jumps", where "large jumps" happen relatively soon after another and could span a larger distance. This distance is roughly twice as large since the jump clusters are typically pairs of "large jumps". However, these clusters of large jumps have a wide distribution of angles. This means the "clusters of large jumps" are not found to have a directional bias.

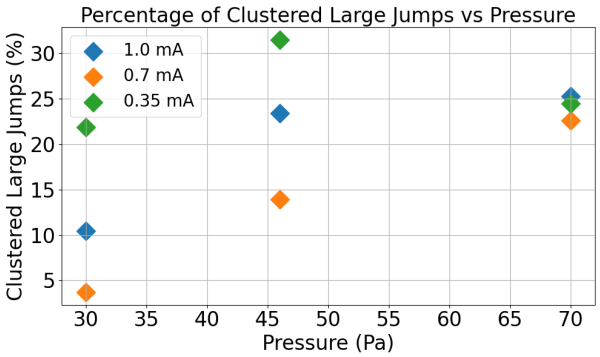

Figure 5.5: Percentage of "large jumps" that are followed by another "large jump" within 10 frames.

Among all pressure–current combinations analyzed, a total of 19 clusters of large particle displacements were identified across the pressure-current datasets. Of these, only three clusters exhibited a directional standard deviation less than 30°, indicating a relatively coherent directional alignment. These three "clusters of large jumps" were aligned in the cross field direction, thus leading to a total displacement in the cross field direction much larger than any other displacement around $250\mu m$. Specifically, two of these clusters originated from the 30 Pa and 0.35 mA condition, while the third occurred under 70 Pa and 0.70 mA.

5.3 FLSM Plots

In this section, we present the results from solving Equation 2.4.6 for Hamiltonian operators encompassing a wide parameter space of nonlocality and stochasticity conditions, which includes the ranges of parameters extracted from the PK-4 experiments. The input parameters for the model are: the fraction on the Laplacian s (which quantifies the type and strength of nonlocality), the number m of terms in the series representation of the fractional Laplacian (which quantifies the range of nonlocality), the dimensionless disorder c (which quantifies fluctuations in potential energy), the number of trials to average over different random realizations of the dimensionless disorder (here we did 8 trials for every parameter combination), the reference scale ν (which is a subspace in Hilbert space), and the number of time-steps N (which corresponds to the number of iterative applications of the Hamiltonian). The series representation of the fractional Laplacian is valid for infinite number of terms m in the series [11], while the extended states conjecture [3] is true for infinite number of time steps N. While this is computationally not feasible, this limitation can be overcome by reasonable truncation of the fractional Laplacian series and running the simulation for sufficient number of time-steps and either extrapolating the distance value at infinity from fitting or performing asymptotic analysis of the final time-steps.

Since the off-diagonal terms of the fractional Laplacian fall off rapidly, we choose a cutoff value of $m = 75$ to account for sufficient nonlocal range behavior. For this number of terms

in the series, only a small remainder is discarded from the calculation, while maintaining computational efficiency. The effect of different series truncations is discussed in more detail in [11] and shown in Table 1 of that paper. Next, since we cannot perform infinite iterations of the Hamiltonian, we perform as many as computationally feasible and then analyze the asymptotic behavior. Curve fitting to the limiting behavior was implemented for a few parameter combinations. Figure 5.6 shows a plot of the distance $D^N_{s,c}$ for the specific case $s = 0.65$, and $c = 0.01$. We tested 6 different curve fitting relations to help find the relation most closely corresponding to the limiting behavior of $D_{s,c}$ over many simulation time-steps. The form $D = A + be^{-kt}$ consistently yields the least error over multiple parameter tests. Since the best fits correspond to an exponential decay function, this provides confidence that the chosen number of time-steps for the simulation is sufficiently large to reveal the limiting behavior of the distance parameter.

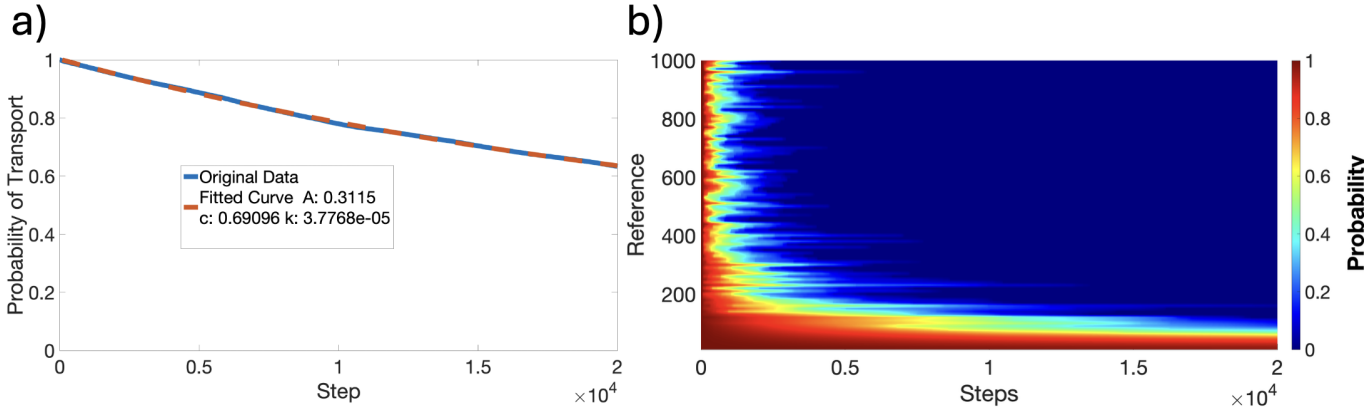

Figure 5.6: Probability for transport $D_{s,c}$ for parameters $s = 0.65$, $c = 0.01$, $m = 150$, and $N = 20000$ time-steps. a) $D_{s,c}$ as a function of timestep for reference scale $\nu = 60$, along with equation fit. b) The value of $D_{s,c}$ as a function of time-step calculated for reference scales from $\nu = 10$ to $\nu = 1000$ in increments of $\Delta\nu = 10$.

The value of $D_{s,c}$ as a function of timestep for a single combination of parameters is shown in Figure 5.6 a). A 3D plot, for the same set of parameters over many reference scales is shown in Figure 5.6 b). These figures are useful to see how the simulation progresses over time and visualize numerical fluctuations (e.g., due to the random realization of disorder). The fits to specific combinations of parameters are useful to infer the functional form of

the asymptotic behavior, here - an exponential decay towards a constant value. However, we find that analyzing the limiting value at infinity for a large-scale parameter scan can be most efficiently performed by asymptotic analysis of the final time-steps. To determine whether $D_{s,c}$ may indicate probability of transport, we look at the asymptotic saturation by analyzing the tail behavior of $D_{s,c}$ after $N = 8000$ time-steps were extracted from each parameter combination. This was done by computing the mean of the absolute rolling slope over the final 200 time-steps of each trajectory

$$\bar{\sigma} = \frac{1}{k-1} \sum_{i=1}^{k-1} \left| \frac{D(N_{i+1}) - D(N_i)}{\Delta N} \right|. \tag{5.3.1}$$

A low rolling slope ($\bar{\sigma} < 10^{-5}$) indicates strong asymptotic convergence, while ($\bar{\sigma} \approx 10^{-3}$) may indicate near convergence. The resulting slope values were visualized as a continuous asymptotic strength map over the parameters s, c, and ν (see representative map in 5.7 b). A log scale of $\bar{\sigma}$ is used for the color axis. Dark blue indicates very good asymptotic behavior and yellow indicates near convergence. This approach allows high-confidence classification of asymptotic behavior across the entire parameter space, independent of fitting assumptions. The major result presented in this section is a large-scale computational study (details in **??**) to find the probability for continuous spectrum (and related transport) with good asymptotic convergence for 55,0000 parameter combinations between the fraction s of the Laplacian, the dimensionless disorder c, and the reference scale ν in Hilbert-space. The main goal is to understand how the combined effect of nonlocality and stochasticity results in transport at key scales. The results from the calculations are maps of the limiting value of the distance parameter (Equation 2.4.6). We present the parameter maps of c vs reference scale ν for several fixed values of s (Figure 5.7 and 5.8), s vs reference scale ν at fixed c (5.9 and 5.10), and s vs c at fixed reference scale (ν 5.11 and 5.12). All figures have been given a slight Gaussian smoothing to help visualization.

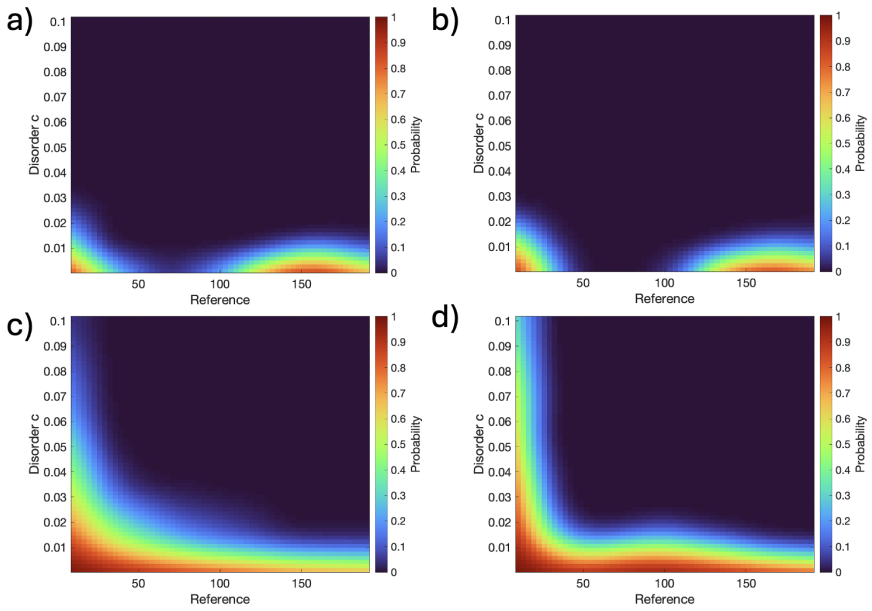

Figure 5.7: Probability of transport for fixed values of s: a) $s = 0.5$ (Lévy process) b) $s = 0.8$ (superdiffusion) c) $s = 1.0$ (classical diffusion) d) $s = 1.3$ (subdiffusion)

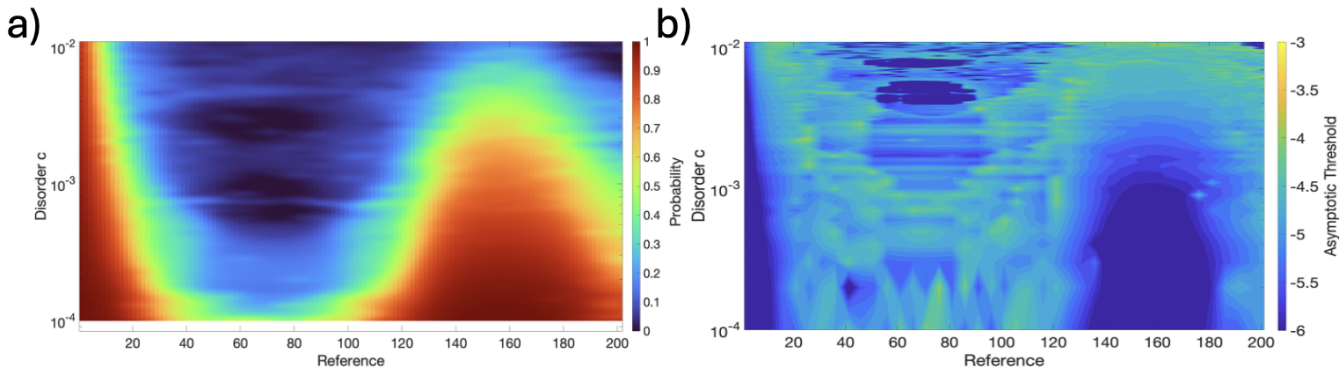

Figure 5.8: (a) Probability for transport for fixed parameter $s = 0.66$, corresponding to the crossover between superdiffusion and a Lévy process. (b) Corresponding asymptotic convergence map. Darker blue regions indicate very strong convergence.

In figure 5.7 we vary the amount of disorder from $c = 0.01$ to $c = 0.1$ in increments of $\Delta c = 0.01$ and the reference scales from $\nu = 10$ to $\nu = 200$ in increments of $\Delta\nu = 10$. Four different values of s were selected to represent distinct diffusion regimes $s = \{0.5, 0.8, 1.0, 1.3\}$. For all four regimes, disorder on the order of $c \approx 10^{-1}$ leads to zero limiting distance value (dark blue regions), suggesting that continuous spectrum cannot be

found. However, nonzero limiting distance value is found for most reference scales when the disorder is on the order of $c \lesssim 10^{-2}$ or smaller. For the Lévy process ($s = 0.5$) and the superduffusion ($s = 0.8$) cases, shown in figure 5.7a) and b), we also see that transport is unlikely at intermediate reference scales $\nu \approx 50 - 100$. While there is no gap in the subdiffusive case ($s = 1.3$), shown in Figure 5.7d), there is a visible dip for small scales $\nu \approx 10 - 50$, which is not observed in the classical diffusion case ($s = 1$), shown in Figure 5.7c). The gaps or dips in probability for transport at certain scales is likely due to the characteristic transport scale defined by the nonlocality for any $s \neq 1$. In other words, each value of s models anomalous diffusion that will cause the particles to perform nonlocal jumps of a certain scale, which will inevitably lead to smaller probability for transport at some intermediate (forbidden) scales. This is true even in the subdiffusive case, which here is modeled as a superposition of classical diffusion and a small superdiffusion part, i.e., $(-\Delta)^{1.3} = (\Delta)^1(-\Delta^{0.3})$.

In Figure 5.8, we show the probability for transport for smaller disorder values $c = 0.0001$ to $c = 0.01$, with $\Delta c = 0.0001$, and smaller reference scale increments $\Delta\nu = 5$, for fixed nonlocality $s = 0.66$, which represents the crossover from superdiffusion to Lévy flights. This map shows that the interesting feature of "forbidden scales" in the range $\nu = 40 - 100$ and an "island of transport" in the range $\nu = 100 - 200$ (peak at $\nu \approx 160$) is reproduced. Figure 5.8 also shows high probability for transport at small scales $\nu < 40$) even for large disorder, which suggests that the disorder-defined localization lengths is larger than these scales or that the nonlocality-defined scale of jumps is larger than the disorder localization length. We find that as the diffusion regime changes from superdiffusion to a Lévy process, the gap of forbidden scales shrinks, while the island of transport broadens, which is consistent with the interpretation that the particle jumps will become larger.

Figure 5.9 shows probability of transport as a function of nonlocality in the superdiffusive regime for $s = 0.5 - 0.86$ with $\Delta s = 0.02$, Reference scale $\nu = 10 - 200$ with $\Delta\nu = 10$, and four different orders of magnitude for the disorder values $c = \{0.0001, 0.001, 0.01, 0.1\}$. Again

we see that higher disorder suppresses the probability of transport, as expected. Also visible are the forbidden scales and the island of transport for $c = 0.0001$ and $c = 0.001$, but in each case, there are certain values of s which result in higher probability for transport, thus bridging the forbidden scales gap. These values may be indicative of crossovers to further sub-regimes in the diffusion behavior. The range of forbidden reference scales is narrower for $c = 0.0001$ as compared to $c = 0.001$, suggesting that the decrease in the disorder localization length leads to narrower range of forbidden scales. This supports the interpretation that the forbidden scales and the island of transport result from the competition between the scale of nonlocal jumps and the localization length.

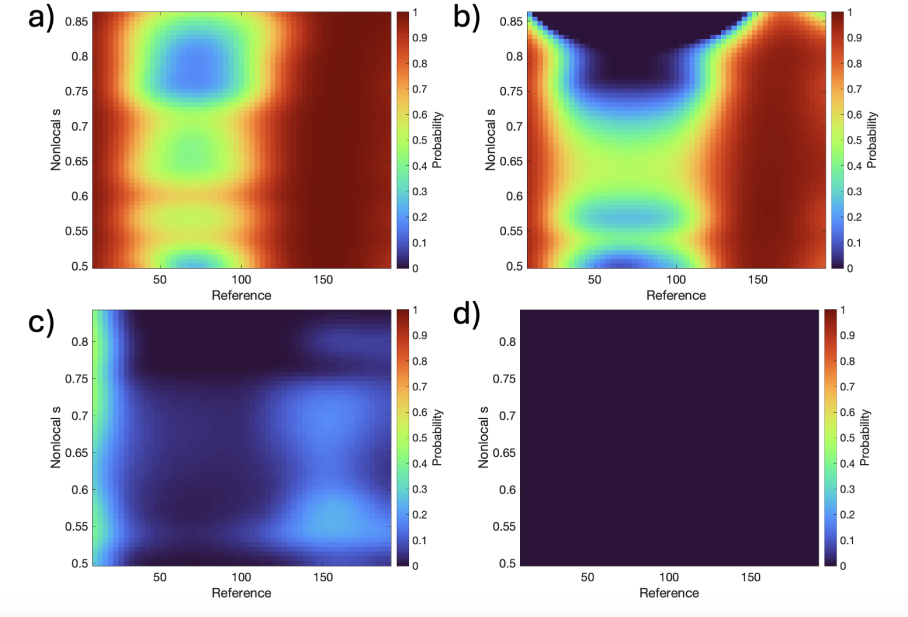

Figure 5.9: Probability of transport for fixed values of disorder a) $c = 0.0001$, b) $c = 0.001$, c) $c = 0.01$, and d) $c = 0.1$.

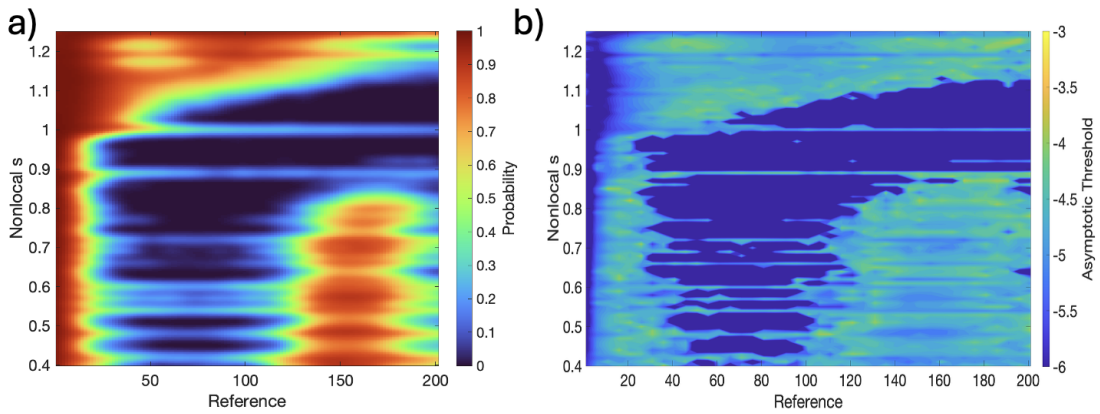

Figure 5.10: (a) Probability of transport for fixed disorder $c = 0.0035$. (b) Corresponding asymptotic convergence map with darker blue indicating very strong convergence.

Figure 5.10 shows probability of transport as a function of nonlocality for $s = 0.4 - 1.25$ with $\Delta s = 0.01$, and reference scale $\nu = 2 - 200$ with $\Delta\nu = 1$, for fixed value of the disorder $c = 0.0035$. This particular disorder value was selected as it represents the average disorder calculated for all the pressure-current cases in the PK-4 experiments. The range of nonlocality values in the figure covers all s values calculated from q-Gaussian displacement distributions in the PK-4 experiment (see Table 5.1). The values extracted for the dust displacement along the direction of the external electric field all fell in the superdiffusion regime with $s \in (0.4, 0.9)$. The values extracted from bi-q-Gaussians corresponding to cross-field diffusion yielded mostly classical diffusion from one of the q-Gaussians ($s \approx 1$) and mildly superdiffusive regime from the other q-Gaussian with $s \in (0.7 - 0.95)$ (see last two columns of Table 5.1). In figure 5.10, a transport island is observed for reference scales approximately within the range $\nu \in (110 - 190)$ for all $s < 1$, except for $s \approx [0.89, 0.99]$, which limits towards a classical diffusion behavior. Transport at scales in the range $\nu \in (110 - 190)$ is less likely for $s \in (1, 1.15]$, which corresponds to subdiffusion. For $s > 1.15$, the probability for transport for this disorder starts to increase again. As we mentioned before, the sub-diffusive fractional Laplacian in this representation is a superposition of classical diffusion and small super-diffusive part. We suspect that the superdiffusion part leads to big enough

jumps to overcome the localization length for this disorder, which is why we see the enhanced transport for $s > 1.15$ at the examined range of reference scales.

Figures 5.11 and 5.12 show probability of transport at fixed reference scales ($\nu = 50$ and $\nu = 150$, respectively) as a function of nonlocality $s = 0.4 - 1.25$, with $\Delta s = 0.01$, and disorder $c = 0.0001 - 0.01$, with $\Delta c = 0.0001$. We chose these two reference scales as the smaller one $\nu = 50$ falls within the range of forbidden scales in figure 5.10, while the larger scale $\nu = 150$ falls within the transport island in the same figure. Figure 5.11 shows increased probability for transport in the subdiffusive regimes for disorder values of up to $c \approx 10^{-3}$ and suppressed probability for transport at higher disorder. This suggests that, subdiffusion in this representation can lead to intermediate-scale jumps that can lead to enhanced transport at intermediate scales even at high disorder, while superdiffusion will not result in transport at these scales for the same disorder concentrations.

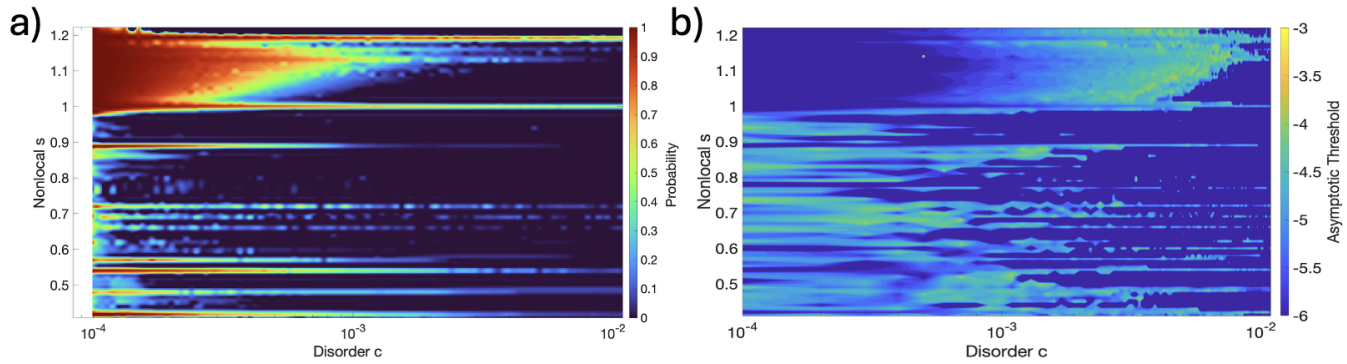

Figure 5.11: (a) Probability of transport with fixed $\nu = 50$. (b) Corresponding asymptotic convergence map. Darker blue regions indicate very strong convergence.

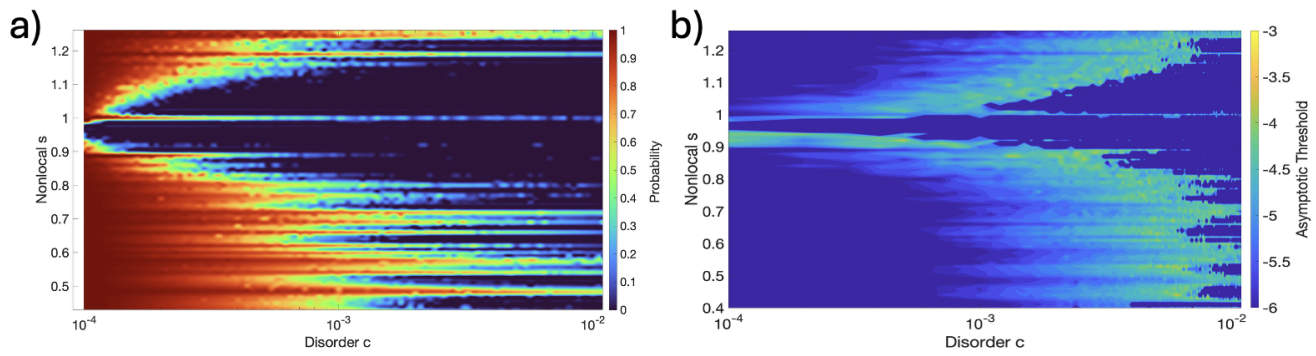

Figure 5.12: (a) Probability of transport for s vs c with fixed $Reference = 150$. (b) Corresponding asymptotic convergence map.Darker blue regions indicate very strong convergence.

In comparing the results for $\nu = 50$ (5.11) to $\nu = 150$ (5.12), again we see evidence of the "island of transport" as there is an increased probability for transport across both disorder scales and powers of the Fractional Laplacian. We also see that for $1 < s < 1.2$ the probability for transport has decreased across disorder scales when compared to figure 5.11. This supports the hypothesis that superdiffusion will cause enhanced transport at larger scales determined by the length of nonlocality. Finally, both figures 5.11 and 5.12 show streaks of high probability for transport for key combinations of disorder and nonlocality. While there may be a mathematical or physical interpretation of this result, we also note that these realizations correspond to cases near convergence (yellow color in convergence maps). Thus, it is possible that these cases take longer to converge to a lower limiting value due to a numerical instability or due to a particular realization of the random disorder.

5.4 Discussion

5.4.1 Disorder

There is a subtle correspondence between the disorder implemented in the Hamiltonian operator (Equation 2.4.1) and the disorder calculated from fluctuations in dust displacements in the PK-4 experiment. In the Hamiltonian, the disorder represents random fluctuations of the potential energy term. Since the dust-dust interaction potential in PK-4 is electrostatic,

it depends on several processes: (i) random fluctuations of the dust charge, (ii) random fluctuations of the ion wakefiled structure surrounding the dust, and (iii) random fluctuations of the dust positions due to collisions with neutral atoms and due to the processes listed in (i) and (ii). Here we only calculated the fluctuation of electrostatic potential energy due to fluctuations of the dust positions, while assuming overall constant dust charge and steady-state wakefield structure. With those limitations in mind, in this formulation, a completely disordered $c = 1$ case is expected to result in no probability for extended states since the distribution of disorders in 2.4.1 acts as a distribution of potential barriers that randomizes the displacements and thermalizes the particle ensemble. Therefore, in the case of highly disordered lattice, even in the presence of nonlocal interactions, the diffusion will be dominated by the thermalization process and the limiting behavior of the system will be classical diffusion (which always leads to only localized energy states for high disorder). Conversely, if $c = 0$ and there are zero potential barriers, then extended states are expected to occur at all spatial scales and for all diffusion regimes, including subdiffusion. In this case, the particles are arranged in an ideal lattice configuration and the different strength and range of nonlocal interactions will only affect the diffusion time, but not the overall probability for transport as time goes to infinity.

In the PK-4 experiments examined here, the dust particles are in a liquid-crystalline state, where strong correlations and alignment into filamentary crystalline structures is observed along the direction of the electric field, while weaker coupling and less alignment is observed in the cross-field direction (see detailed analysis of pair correlation functions for these experiments in [**?**]). In agreement with these observations, in section 4.3, we found that the dust particles exhibit superdiffusion in the direction along the electric field, which resulted in enhanced probability for transport observed in the spectral maps presented here. In the cross-field direction, we found a bi-q-Gaussian distributions of positions, suggesting a superposition of diffusive and a weakly superdiffusive behavior. This agrees with the observation that there is weak coupling in the cross-field direction, but the structure is more

disordered, which thermalizes the displacements in this direction and decreases the probability for transport.

Lastly, when comparing the calculated disorder 5.1 to the classification of characteristic step-wise jumps 5.2, we found that there is a positive correlation of slight significance ($p = 0.09$) between the percentage of "clusters of large jumps" and the maximum disorder given in Figure 5.3 b). This suggests that regions of increased structural disorder can be linked to a more frequent occurrence of large jumps, thus, providing evidence that disorder and nonlocality can act constructively to enhance diffusion. We also tested if there existed correlation between the mean disorder and mean step-size jumps. While we found a moderately positive trend, the resulting statistical significance was not strong enough ($p = 0.13$) and requires more data to verify.

5.4.2 Spatial Scaling

Dusty plasma is notorious for its complexity due to the multi-physics multi-scale phenomena arising from the charge to mass ratio of the different charged species (electrons, ions, and dust) and due to the presence of collisions with atoms from the neutral background gas. The system encompasses many scales of dynamics, from charging at the dust surface, to inter-particle interaction mediated by extended ion wakefields, to local electrostatic confinement effects due to striations of the plasma discharge. In the present study, we only focus on the characteristic spatial scales of dust dynamics as observed from particle tracking data from the PK-4 experiments. There are several distinct spatial scales that can be considered. The smallest range of scale is defined by the dust particle diameter, here $\approx 3.38\mu m$, and the pixel size, here $\approx 14.2\mu m$. Typically, the light reflected by a single dust grain of that size results in a bright spot that extends over several pixels. The particle tracking algorithm used here can identify the location of the dust particle with some sub-pixel resolution and has been shown to be robust against pixel locking [128]. Thus, it is reasonable to assume that the smallest relevant spatial scale is on the order of $\approx 10\mu m$. At this smallest scale, the

background plasma, neutral gas pressure, and electrostatic field exchange energy with the dust and the fluctuation of this exchange is proportional the dust kinetic temperature.

The next range of relevant spatial scales is defined by the spatial extent of the ion wakefields and the resulting interparticle separation (here, $\approx 220-250\mu m$, as calculated from pair correlation functions in [**?**]). The actual spatial scale extent of the ion wakefields in these experiments is expected to be anisotropic (larger along the direction of the electric field) and fluctuating due to the presence of high-frequency ionization waves in the background plasma discharge [124, 136]. The ion wakefied is a structure in which positive space charge accumulates locally, especially in between neighboring dust grains within field-aligned filamentary structures. It is reasonable to assume that the dynamics of the positive space charge regions within one interparticle separation will result in dust displacements on the order of half the interparticle separation. Thus, we expect that these processes result in an intermediate spatial scale for the dust dynamics of $\approx 100\mu m$. This is confirmed by the maximum step size of dust displacements shown in 5.4 a). In all pressure-current cases analyzed, the maximum displacement found was in the range $140-180\mu m$, which is smaller than the corresponding interparticle separation.

The largest relevant spatial scale is that of the whole dust cloud, which extends to $\approx 6-8mm$ in width in the camera field of view. While in the experiments, we observe some particles making large jumps (on the order of $\approx 1000\mu m$) across big sections of the cloud's width, those were excluded from the analysis due to limitations of the particle tracking. Therefore, we assume that this is this third, and largest spatial scale of dust dynamics is not captured by our analysis.

Here we propose that there is a correspondence between the characteristics spatial scales of dust dynamics as observed from experiment and the distinct ranges of reference scales ν (or subspaces) in the Hilbert space for which the FLSM calculation predicts high probability for transport. The statistical analysis of the PK-4 data suggested that the dust diffusion along the direction of the external electric field is in the strongly superdiffusive regime, with

$s \in (0.5, 0.85)$ for all pressure-current cases. Comparison with figure 5.10 suggest that, in this regime, the probability for transport is high for small scales, $\nu < 20$, and for intermediate scales, $\nu \in (110, 190)$, but the range of scales in between is forbidden. This agrees with the physical picture that the displacements of dust particles along the direction of the electric field in PK-4 is either on the order of $10\mu m$ due to kinetic temperature motion or on the order of $100\mu m$ due to interactions with the wakefield structure. For motion in the cross-field direction, we found that the diffusion is either close to classical, $s \in (1, 1.1)$ or weakly superdiffusive, $s \in (0.85, 1)$ for most cases, which yielded higher probability for transport at small scales and no transport island at larger scales. The subset of values $s \in (1, 1, 1)$ even suggested high probability for transport at a slightly larger range of smaller scales $\nu < 60$. This agrees with the physical picture that the smaller ion wakefield extent in the cross-E-field direction results in overall smaller scale displacements, closer to the scale of kinetic temperature displacements. We did observe smaller displacements in the cross-field direction, with the exception of the three "clusters of large jumps" discussed in section 5.2. It is also reasonable to assume that, since the ions are streaming along the direction of the electric field and forming macroscopic regions of positive space charge in between the dust particles within filaments, the wakefield fluctuations (causing the large dust displacements) are greater in this streaming direction than the cross-stream (cross-E-Field) direction.

5.4.3 Comparing to Other Studies

A recent study [**?**] using the same data sets of PK-4 experiments conducted a detailed structural analysis of the dust clouds using 2D and 3D pair-correlation functions. The study found that, at low pressure (28 Pa), the bulk cloud exhibits crystalline properties with isotropic short-range coupling of particles within filaments and across neighboring filaments. At higher pressure (70.5 Pa), the coupling of particles within filaments becomes both stronger and longer-range, enhancing crystalline behavior, while the coupling across-neighboring filaments become liquid-like, suggesting a transition to a liquid-crystal structural state [**?**].

The present study found that, at higher pressure, the average system disorder figure 5.3 a) decreased, which agrees with higher crystalline order. As mentioned earlier, for the different scales of step-sizes (mean, large, and clustered), the $\|$-step-sizes tend to decrease more with increasing pressure than the $\perp$-step-sizes. The step-sizes in the $\|$-direction decreasing faster with pressure agrees with the enhanced crystalline behavior within filaments, while the step-sizes in $\perp$-direction decreasing slower agrees with a more fluid-like behavior across neighboring filaments. Our findings seem to be in agreement with those found from the pair correlation analysis in [**?**].

5.5 FLSM Conclusions

In this chapter, we presented an in-depth analysis of anisotropic anomalous diffusion in dusty plasma using the Fractional Laplacian Spectral Method (FLSM). We calculated the probability for transport at different scales in Hilbert space from the spectrum of a Hamiltonian that models nonlocality using a fractional Laplace operator and stochasticity using a random disorder potential energy term. The calculations were informed from statistical analysis of PK-4 dusty plasma experiments that yielded ranges of values for the nonlocality fraction s on the Laplacian and the dimensionless disorder c for the potential energy term. The nonlocality fractions were obtained using scaling relations from literature and the statistical parameters calculated in section 4.3. The dimensionless disorder was quantified from fluctuations of dust densities and displacements. The relationship between the scales (or subspaces) in Hilbert space and the characteristic scales of dust dynamics observed in experiments was obtained through physical arguments based on a classification of the different step-sizes observed in particle trajectories.

For the characteristic disorder in the PK-4 clouds, the spectral results predicted that superdiffusive motion will yield high probability for transport at smaller and intermediate scales in Hilbert space, but there will be a range of forbidden scales in between. Physically, this was found to agree with the observation that the dust displacements along the

direction of the external electric field in PK-4 either happen at the scale of the camera pixel resolution (due kinetic temperature motion) or at an order of magnitude larger scales (due to fluctuations in the wakefield structure surrounding the dust grains. The spectral calculation further predicted that probability for transport in the cross-field direction will be high only at smaller scales, which is consistent with the picture where streaming ions in the ion wakefields reduce dust displacements in the cross-field direction. We reiterate that for $D_{s,c} \to 0$ the extended states conjecture does not imply localized states, therefore there may some part of the singular continuous spectrum at play that could be an avenue of future research. We further observed that, along the direction of the external electric field, both the average system disorder (calculated here) and the dust kinetic temperature (calculated in chapter 5) decrease with increasing pressure, consistent with the transition to a liquid-crystalline structure observed by [**?**].

This study also presented a large parameter scan yielding high-resolution maps of the probability for transport (Equation 2.4.6), resulting from 55,000 combinations of nonlocality fraction, disorder parameter, and reference scale in Hilbert space. As expected, the probability for transport decreases with increasing dimensionless disorder bigger than a threshold of $c \approx 10^{-3}$. Unexpectedly, below the threshold, we found "islands of transports" and ranges of forbidden transport scales for a broad range of nonlocal s values within the superdiffusive regime. This suggests that nonlocality and stochasticity can have a scale-dependent constructive or deconstructive effect on transport. We hypothesize that these "islands of transport" result from an interplay between disorder-defined localization length and nonlocality-defined jump scale, which strengthens the argument that nonlocal processes have an optimal scale where their effect is most prominent.

The present study further supports the growing perspective that dusty plasma systems, such as those observed in PK-4, can serve as powerful analog models for studying transport and structural transitions relevant to condensed matter and complex systems. The existence of anisotropic pressure-dependent trajectory displacements, Lévy-type flights, and system

disorder mirror the kinds of phenomena encountered in solid-state systems and strongly coupled systems undergoing structural transitions and nonequilibrium states. In fact, the spectral model used here originates from studies on the the metal-to-insulator transition in Anderson localization [116]. As dusty plasmas operate on mesoscopic spatial and temporal scales that are optically resolvable and externally tunable, they provide a uniquely accessible platform for experimentally probing nonequilibrium dynamics, transport in disordered potentials, and the statistical nature of transitions between liquid-like and crystalline regimes, as has been shown in section 4.3 and chapter 5. These parallels suggest that dusty plasmas may not only help validate theoretical models originally developed for quantum systems, but also inspire new frameworks for understanding complex transport in systems that bridge order and disorder across scales.

Next, we move to magnetically confined fusion plasma and analyze magnetic island topology, chaos and field line disorder, and what this says about diffusion and transport properties. We discuss the relevance of nonextensive statistics in fusion plasmas from existing literature and how it may applied to this very different plasma regime. We also develop a scale free quantification of the disorder of the magnetic field lines, similarly to what was done in section 5.1. This allows us to briefly discuss future application of FLSM to magnetically confined fusion plasmas.

Chapter 6

Nonextensive Statistics as a Model of Magnetic Field Line Diffusion in Magnetized Plasma

The magnetized plasma regime is of great interest to both fundamental plasma science and fusion energy research. The pursuit of fusion energy has long been motivated by its potential for high energy yield and minimal emissions. However, realizing this potential has been difficult, in part due to the challenge of understanding and controlling disruption events. These disruptions, during which plasma particles escape confinement and strike the reactor wall with significant energy, pose a serious threat to sustained operation. As a result, studying the causes and characteristics of disruptions has become central to advancing magnetically confined fusion research. One key pathway is through understanding the interaction between magnetic field structures and the plasma species, which often leads to anomalous diffusion.

In this chapter, we study how magnetic field line diffusion is affected by changes in magnetic topology, specifically, the formation and bifurcation of magnetic islands in a tokamak device. As the electrons and ions in magnetically confined fusion devices are magnetized (i.e., closely following the magnetic field lines), we expect that the crossover from classical to anomalous magnetic field line diffusion can significantly affect plasma confinement and contribute to disruptions. Understanding the formation and dynamics of magnetic islands is not only important for confinement quality in fusion devices, but also for understanding anomalous electron/ion diffusion and nonlocal transport in other magnetized plasma environments, such as the Earth's magnetosphere. Building on this, we present a literature review connecting Tsallis' nonextensive statistics to the observed non-Gaussian distributions in particle densities, particle velocities, and magnetic field line fluctuations in magnetized plasmas. We further discuss studies that explore fractional derivative models and self-organized criticality

as theoretical frameworks for understanding the statistical nature of transport and field line topology in magnetized plasmas.

6.1 Literature Review

The fundamentals of anomalous diffusion, non-Gaussian distributions as it relates to Tsallis statistics, and fractional derivative operators have been laid out and discussed in chapter 2. Here we present relevant material in the literature relating these topics to magnetized plasma. While anomalous diffusion in magnetically confined plasmas has been extensively discussed in literature, there is no census on what causes it or how best to model it. This dissertation proposes that nonextensive statistics may be a good model for anomalous diffusion in magnetized plasmas since the fundamental theory, shown to describe well other cases of anomalous diffusion in plasmas, and, is system agnostic. In addition, modern day developments in diagnostics and synthetic diagnostics allow for reconstructions of electron and ion distributions directly from experiment. Those can be quantified using nonextensive statistics and scaled as input parameters in other models, such as the FLSM discussed in the previous chapters.

Sattin et al. [144] provided experimental evidence that particle flux in edge fusion plasmas follows power-law tails, similar to the nonextensive q-Gaussian distributions, challenging traditional transport models. Hauff et al. [145] showed that test particle transport in nonlinear gyrokinetic core plasma turbulence leads to particle displacement distributions similar to the Bi-q-Gaussian distributions given in section 4.3. The study demonstrates that intermediate superdiffusion and subdiffusion regimes emerge due to stochastic fluctuations of magnetic fields. Benkadda et al. [146] observed that the azimuthally averaged momentum and particle fluxes driven by turbulence in magnetized plasma exhibit non-Gaussian PDFs. The study also discusses a crucial need for obtaining a relationship between particle transport and momentum transport, underscoring the need for global, rather than local, transport models in turbulent magnetized plasmas. Crilly et al. [147] further develop a theoretical framework for classifying ion velocity distributions using fusion product spectroscopy.

Their analysis reveals that inertial confinement fusion experiments exhibit spectral moments inconsistent with Maxwellian velocity distributions, necessitating a kinetic description of reacting ions. Kong et al. [148] explored the impact of non-Maxwellian velocity distributions, including drift-ring-beam and kappa super-thermal distributions, on fusion reactivity. Their results show significant reactivity enhancements in D-T and p-B11 fusion reactions. Lastly, Goud [149] used from statistical analysis to show that fluctuation induced poloidal flux has a strongly non-Gaussian PDF (see Figure 5 in their work). These experimental measurements were performed as a function of increasing toroidal magnetic field strength. This study is similar and may be closely tied to the analysis done here on poloidal flux distributions resulting from toroidal perturbations.

Next we review literature on Lévy statistics, fractional transport, and self-organized criticality (SOC) for magnetized plasmas. Sokolov and Klafter [150] introduced Monte Carlo simulations of charged particle dynamics in the presence of Lévy electrostatic fluctuations. Their findings reveal that when turbulent fluctuations follow Lévy distributions, the resulting transport shifts from exponential decay to power-law distributions, implying that guiding center approximations may be inadequate in such regimes. Sánchez et al. [151] introduced fractional transport models based on continuous-time random walks and fractional differential equations to SOC effects in magnetically-confined turbulent plasmas. The framework discussed in this study may be directly related to the non-Gaussian distributions through the scaling relations discussed in section 2.2. Similarly, numerical work by del Castillo-Negrete et al. [152] provided evidence of fractional transport in plasma turbulence, with test particle displacements exhibiting power-law distributions. Using a similar tracer particles approach, Gheorghiu et al. [153] linked fractional transport terms to zonal flow dynamics, demonstrating how these structures influence transport behavior in edge plasma turbulence.

Lastly, we revise literature discussing magnetic field line complexity, which is strongly linked to particle transport. However, the exact nature of the connection between field line complexity and anomalous particle diffusion is not clear. We hope to better understand the

connections between the two in this chapter and in future work. First, Lemoine [154] demonstrated how non-Gaussian fluctuations in magnetic field curvature affect particle transport in turbulent plasmas. This, along with findings by Burlaga et al. [133] and Sokolov et al. [150] suggests that background field fluctuation distributions and particle transport distributions are strongly linked. Myra et al. [155] examined poloidal drift effects in turbulent transport, showing how diffusion coefficient can be sensitive to the spectral width of the magnetic turbulence relative to a finite Larmor radius parameter. Next, Särkimäki et al. [156] found that magnetic islands in tokamaks are transport barriers for cross-field electron diffusion, implying that they act as mechanism for subdiffusive particle transport. Evans et al. [157, 158] and Bardczi et al. [159] studied homoclinic tangles and resonant magnetic perturbations, demonstrating that chaotic field lines caused by island bifurcations can influence particle diffusion in fusion devices. Numerical studies by Wingen et al. [160] showed that magnetic perturbations in DIII-D deform the separatrix, creating fractal bands that enable deep plasma penetration and laminar flux tubes that rapidly transport particles to divertor targets. This study seems to suggest that highly disordered field lines increase superdiffusion. Lastly, Muraglia et al. [161] and Moges et al. [162] further differentiated between field line stochasticity and orbit chaos, showing that energetic particles follow unique chaotic trajectories distinct from magnetic structure. This literature review shows several complexities of studying diffusion in magnetized plasma. While magnetic field fluctuation PDFs and particle PDFs may be linked and it is expected that field line chaos influences the particle trajectories, high energy particles can exhibit diffusion behavior distinct from the field line diffusion. In this chapter, we focus on the investigation of magnetic field line diffusion only using the nonextensive statistics framework. However, in future work, the analysis can be extended to include tracer particle diffusion and examine the conditions in which the tracer PDFs become distinct from field lines PDFs.

6.2 NSTX-U Simulation

Here we examined data from a simulation of the NSTX-U tokamak that aimed to investigate magnetic island bifurcations caused by 3D coil perturbations. The data used here was originally published in Wu et al. [163]. That study utilized the M3D-C1 linear resistive magnetohydrodynamic (MHD) code [164] to generate magnetic equilibrium for an NSTX-U discharge. Then, the TRIP3D field line tracing code [165] was used to investigate the topological bifurcations of magnetic islands resulting from $n = 3$ small 3D magnetic perturbation fields. The NSTX-U equilibrium was synthetically generated using the following parameters: plasma current of $I_p = 1.5$ MA, a toroidal magnetic field of $B_T = 1.0$ T, a safety factor at the edge of $q_{95} = 8.7$, an aspect ratio $A = 1.9$, and beta value ($\beta_N = 5.5$). The magnetic field reconstruction was then perturbed to create magnetic islands on the $q = 3$ resonant surface using increasing input currents for the simulated effect from non-axisymmetric control coils (NCCs) at NSTX-U. This latter step employed TRIP3D-GPU, a parallelized field line integration code, to trace magnetic field line trajectories and to generate Poincaré plots, which served as the primary dataset for analyzing magnetic topology changes caused by the coil perturbations. The TRIP3D-GPU code integrated nonlinear magnetic field line differential equations with a toroidal angle step size $\Delta\phi < 1^\circ$ to ensure sufficient accuracy for resolving island structures. The field line tracing incorporated synthetic magnetic perturbation fields, allowing detailed visualization of island evolution and bifurcation events. The primary focus of the analysis in Wu et al. [163] was the $m/n = 9/3$ islands on the $q = 3$ resonant surface, where successive bifurcations led to the formation of new sub-islands as the perturbation coil currents were increased. Here we use the same data as in Wu et al. [163], but build on the analysis by quantifying the field line diffusion regime for each perturbation using nonextensive statistics.

6.3 Analysis of NSTX-U Synthetic Equilibria

In magnetically confined plasmas, such as those found in tokamaks and stellarators, the large-scale structure of the magnetic field is described by a magnetohydrodynamics (MHD) equilibrium. This equilibrium is governed by the balance between the Lorentz force and the plasma pressure gradient, given by the steady-state MHD force balance equation:

$$\vec{J} \times \vec{B} = \vec{\nabla} P \tag{6.3.1}$$

where $\vec{J}$ is the current, $\vec{B}$ the magnetic field, and $\vec{\nabla} P$ the pressure gradient. Under the assumption of axisymmetry, this equation can reduce to the Grad–Shafranov equation, a second-order partial differential equation that describes the shape of magnetic flux surfaces. A key quantity in describing magnetic geometry is the poloidal magnetic flux Ψ, which is commonly used to label magnetic flux surfaces. To compare profiles across different discharges or machines, it is convenient to normalize this flux. The *normalized poloidal flux* is defined as:

$$\Psi_N = \frac{\Psi - \Psi_{\text{axis}}}{\Psi_{\text{edge}} - \Psi_{\text{axis}}}, \tag{6.3.2}$$

where Ψ_{axis} and Ψ_{edge} are the values of the poloidal flux at the magnetic axis (possibly close to the geometric center) and the plasma edge, respectively. This normalization maps flux surfaces onto a dimensionless interval $[0, 1]$, allowing for the definition of radial profiles and surface-averaged quantities independent of machine size or plasma shape. The normalized flux is essential for constructing equilibrium profiles, interpreting diagnostics, and performing transport analysis, particularly in the study of turbulence, magnetic islands, and edge-localized modes (ELMs). The focus of the present analysis using simulated NSTX-U equilibria is on magnetic island formation and the onset of stochasticity during island bifurcations, which can be visualized using Poincaré maps. These plots display the normalized poloidal flux, Ψ_N, as a function of the poloidal angle, revealing the topology of magnetic field

lines. Poincaré maps—also referred to as puncture plots—represent the successive intersections of magnetic field lines with a poloidal cross-sectional plane located at a fixed toroidal angle. Those plots provide insight into the structure of flux surfaces and the degree of field line chaos.

6.3.1 Fitting the Normalized Poloidal Flux

In magnetically confined plasmas, such as those in tokamaks, modes are often characterized by two integers: the poloidal mode number m and the toroidal mode number n. A mode with the label m/n describes the number of oscillations or wave crests the perturbation has in the poloidal and toroidal directions, respectively. For example, a 9/3 mode implies that the perturbation wraps around the torus 9 times poloidally for every 3 times it wraps toroidally. This corresponds to a safety factor (or winding number) $q = m/n = 3$, which describes the field line pitch at the resonant surface where this mode is most likely to be excited. Such modes are significant in analyzing MHD stability and magnetic island formation, as resonances between the mode structure and the magnetic field geometry can lead to tearing modes, magnetic islands, or other instabilities. The NSTX-U simulation data examined the 9/3 mode caused by $n = 3$ nonaxisymmetric perturbations (i.e., perturbations what will cause resonance at every magnetic surface $q = m/n = m/3$). Therefore, while Ψ_N extends from the magnetic axis to the last closed flux surface (LCFS), the below plots show a reduced region ($\Psi_N \approx 0.5 - 0.6$ where the 9/3 mode resides. Here we consider six values of the perturbation coil current at $1kA, 2kA, 4kA, 8kA, 13kA$, and $16kA$ analyzed. Figure 6.1 shows the $8kA$ NCC perturbation with colored flux tubes to highlight the 9/3 surfaces and magnetic islands. We can see nine islands, each with sub-islands containing two O-point regions colored in magenta and cyan, surrounded by blue, green, or red colors for the external island surfaces. The islands with matching color of the external surfaces are connected flux tubes representing each of the three toroidal mode numbers n.

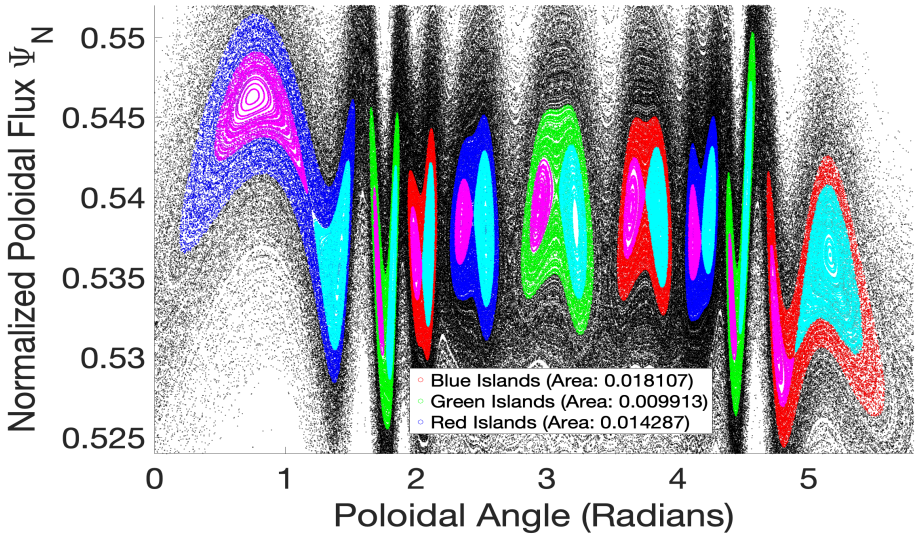

Figure 6.1: Poincare map of the 8 kA perturbation case with colored islands tubes and sub-islands. The islands with matching color of the external surfaces (blue, green, or red) are connected flux tubes representing each of the three toroidal mode numbers n. Each flux tube consists of three connected islands, each of which contains two sub-islands, marked in magenta and cyan, for all islands.

In Figure 6.2 we see the Poincaré map for the a) the smallest perturbation case $1kA$ and b) the largest perturbation case $16kA$. The y-axis has the histogram of the normalized poloidal flux superimposed in red. Figure 6.2 shows both the 9/3 island chain as well as the surrounding poloidal flux region. We can see that in 6.2 a) the flux surfaces form a smooth distribution across the island structures while in6.2 b), the island topology has drastically changed and the surrounding poloidal flux surfaces are now broken up and stochastic.

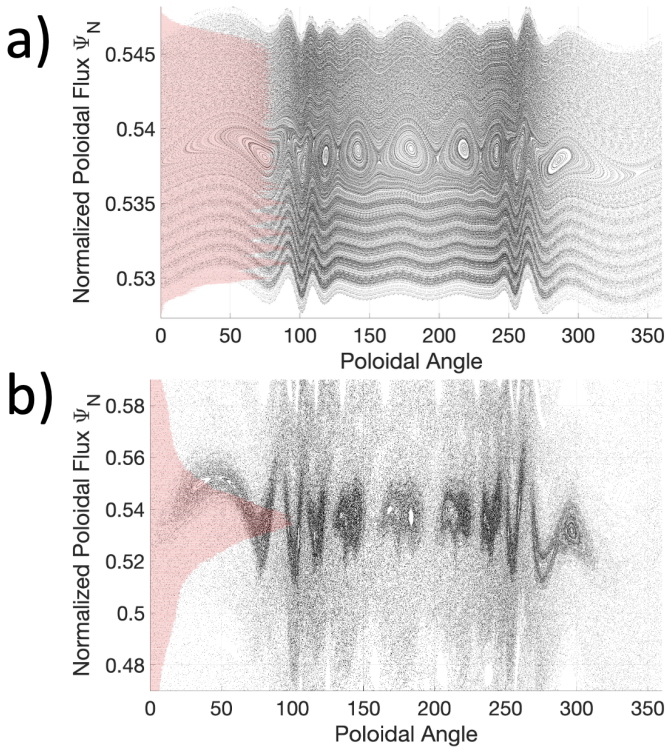

Figure 6.2: Poincare map for a) the 1 kA and b) the 16 kA nonaxisymmetric perturbations. The histogram of the normalized poloidal flux data is superimposed on the y-axis in red.

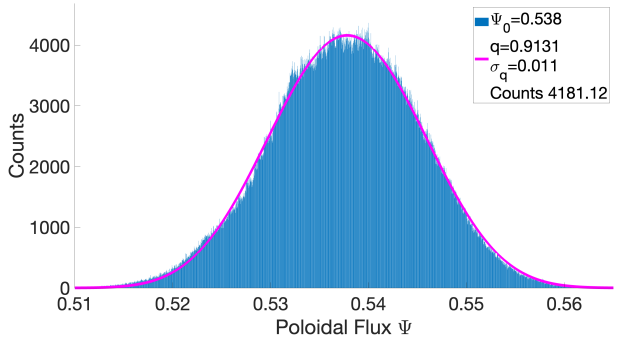

Figure 6.3: Normalized poloidal flux of the 8 kA perturbation with q-Gaussian fitting.

For each perturbation case, the histogram of the normalized poloidal flux was fit with a q-Gaussian distribution as seen in Figure 6.3, and the q_p parameter was recorded. The spatial parameter q_p is used since the poloidal flux is in some ways a radial coordinate, therefore, the distribution is a fit in position space. Figure 6.4 shows how the q_p parameter changed with increasing the coil current of the nonaxisymmetric perturbation.

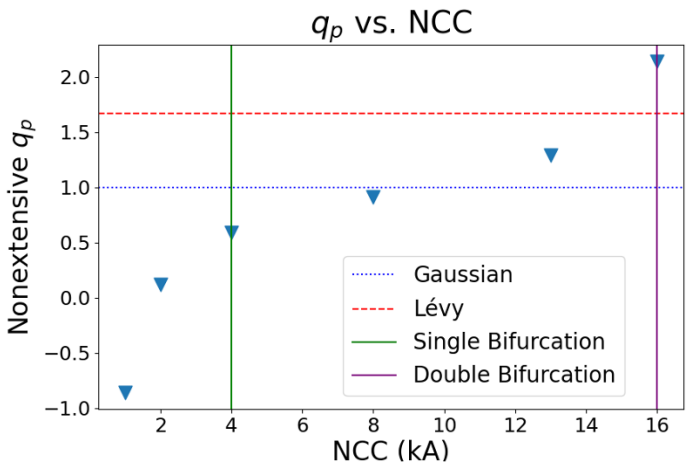

Figure 6.4: Nonextensive q_p as a function of the coil current of the simulated nonaxisymmetric perturbations.

In Figure 6.4, we see a monotonic increase of the q_p parameter as the current in the perturbation coils increases. The relationship between q_p and NCC is clearly nonlinear with rapid increase of q_p at both the low and high NCC currents and an inflection point for the curvature at $8kA$. The two vertical lines in Figure 6.4 mark the current values for which the islands on the 9/3 flux surface experienced bifurcations. Here, we define an island bifurcation as the process in which a single O-point becomes two O-points, resulting int he formation of sub-islands within an island. Figure 6.4 indicates that the islands experienced two bifurcation events - at $4kA$ and at $16kA$. In the same figure, the horizontal lines mark the values of q_p that correspond to a Gaussian $q_p = 1$ and a Lévy $q_p \geq 5/3$ distribution of the normalized poloidal flux. It can be seen that the diffusion regime corresponding to the flux distributions transitions from sub-diffusion to classical diffusion after the first bifurcation and from superdiffusion to a Lévy process at the second bifurcation. Assuming that the electrons in the fusion device are highly magnetized, which is to be expected for the strong magnetic field ($\approx 1T$), Figure 6.4 suggests that the cross-field electron diffusion will experience similar transitions as the perturbations are increased. This means that for small perturbations and a simpler island structure, the electrons in the region local to the 9/3 surface will exhibit subdiffusive transport, which can be interpreted as the electrons being trapped inside the

islands and having uniformly spaced flux surfaces. However, as the toroidal perturbation is increased and island bifurcations happen, the electron diffusion will transition to a classical and eventually to a superdiffusive one that can even lead to Lévy flights. This can be interpreted as resulting from the increased stochasticization of the magnetic island surfaces. Most models of flux surfaces with increased perturbation, mode resonances, or some other process that greatly changes the flux surface topology and the stochasticity of the field are rather complex as great care is required for a rigorous treatment of folding flux tubes and nonlinear Hamiltonian chaos. However, the flux distribution analysis using the nonextensive q_p, combined with the scaling relations discussed earlier, may provide a much simpler method of analysis. Though it is not common to consider the poloidal flux in magnetized plasmas as a distribution, some discussion of this theoretical approach is presented later in 6.4.

6.3.2 Quantifying Field Line Disorder

Similar to the treatment presented for dusty plasma, in addition to quantifying the anomalous diffusion regime, it is desirable to develop a dimensionless measure of disorder in the field line positions. Here we use the term disorder to mean both field line chaos and field line stochasticity, as it can be expected that the the field lines will first become chaotic and then stochastic as the perturbation current is increased. The dimensionless disorder of magnetic field line positions can be quantified using a KD-Tree of the spatial map of the field lines, similar to the process done in section 5.1. The initial conditions for the simulated normalized poloidal flux was a uniform distribution of field lines centered around the 9/3 magnetic flux surface. Each field line was colored-coded based on its initial position, yielding a map where color-mixing in any region indicates deviations from the initial field line positions.

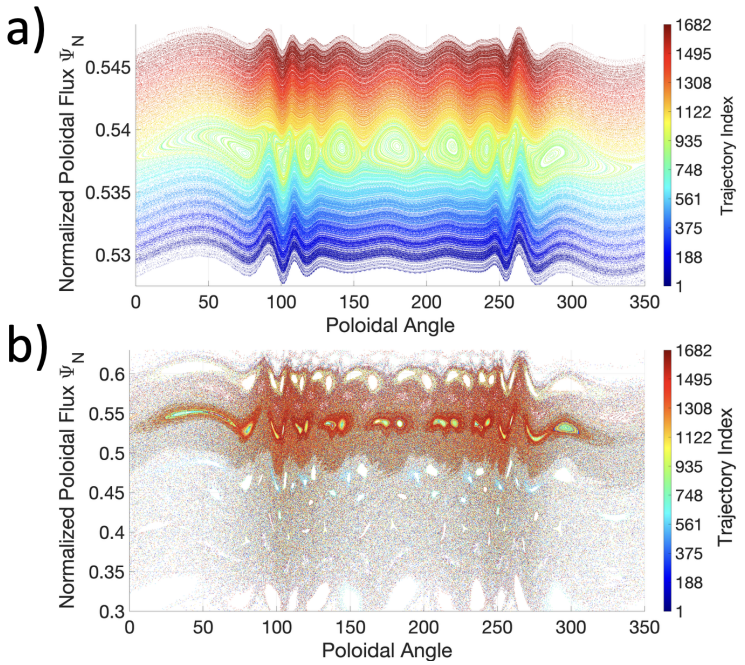

Figure 6.5: 1 kA a) and 16 kA b) Poincaré plots with field line trajectory indices colored.

Figure 6.5 a) shows the $1kA$ perturbation with field lines color coded. We see that the distribution is almost the same as a uniform distribution of the lines except around the island O-points where some mixing of fields lines is represented by the green and yellow colors. Figure 6.5 b) shows the largest perturbation case - achieved with $16kA$ current. In this case, we see that the field lines mixed greatly with lines that started near the bottom (blue trajectories) now being located at the top and vice versa. While Figure 6.5 b) seems to show more of the red field lines, that is only because the red scatter points are plotted last and thus overlap with other field line colors. This is more clear in Figure 6.6 below when we zoom in.

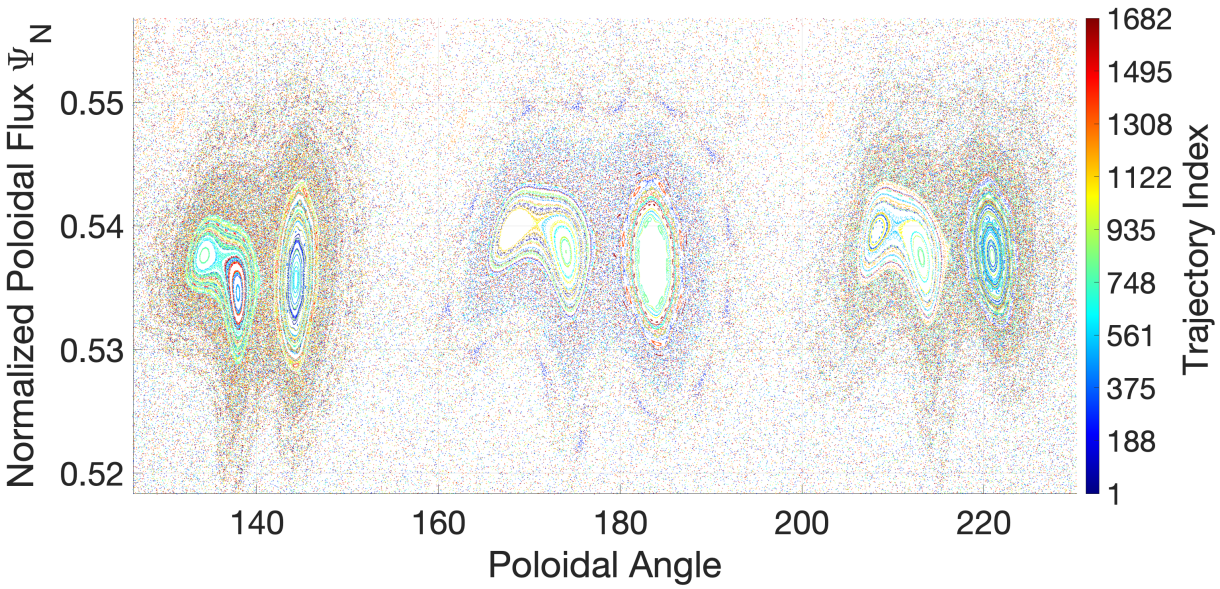

Figure 6.6: Colored $16kA$ Poincaré plot zoomed onto the center three islands.

In Figure 6.6, we can see more clearly, quite frankly, the beautiful mixing of the field lines around the center island region of the normalized poloidal flux. While the intricacy and fractal nature of magnetic islands in Poincaré plots has previously been shown, this may be the first time presenting such figures with the added dimension of color corresponding to the individual trajectory index. The resulting patterns can be quite stunning. Looking closely, there are small orange islands above the three main island surface embedded within the stochastic background. These are called satellite islands and are highlighted in Figure 6.7, where we see larger satellite islands in red and smaller satellite islands in blue.

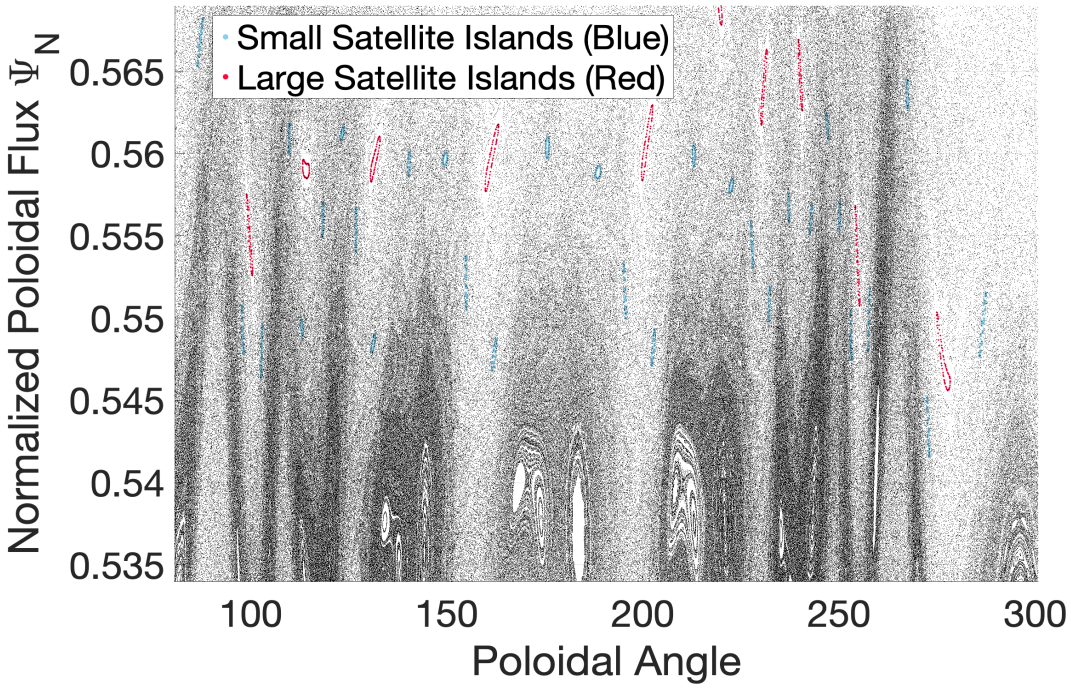

Figure 6.7: The $16kA$ case zoomed to showcase the satellite islands circled in red (larger) and blue (smaller).

With the increased spatial information provided by color indexing the magnetic field line trajectory (as shown in Figures 6.5 and 6.6), we can qualitatively discuss disorder for each of these conditions. Regions where scatter points run parallel or smoothly trace out a curve, such as the small oscillation seen in Figure 6.5 a) around angles 100° and 260°. The ellipsoidal curves in that plot outline the island structure which visibly looks less disordered. In contrast, regions such as those in Figure 6.6 surrounding the island surfaces show a scattering of points as though chosen by a random sampling from a uniform distribution, which are visibly disordered. For these scatter points, it is very difficult to impose a quantifiable metric of disorder as was done in the PK-4 dust lattice in Section 5.1. There are too many different types of structures that can be observed, yet difficult to trace out, such as the complex ellipsoidal shapes of the islands. This makes it challenging to use the same method of having a baseline structured system and using KD-Tree solver to analyze each region around a single particle for this structure, as was done in section 5.1. However, the trajectory color index aligns well with the structures of the magnetic islands. Therefore, we can define the disorder

as the variation in the color or trajectory index at a single point with respect to those of the neighboring points.

Disorder in a spatially distributed index system is quantified by evaluating the variance of particle indices in localized regions. Each point is assigned a unique color or index based on its trajectory. Disorder is computed by determining how mixed these indices are in space. A KD-Tree is constructed from the spatial coordinates (θ, Ψ_N) to efficiently find local neighborhoods. For each point, a neighborhood of radius r is defined, and the indices of neighboring points are collected. The local disorder is measured by computing the variance of these indices

$$\sigma_i^2 = \frac{1}{|\mathcal{N}_i|} \sum_{j \in \mathcal{N}_i} (I_j)^2, \tag{6.3.3}$$

where $\mathcal{N}_i$ is the set of neighboring indices and I_j is the index number of the field line. To ensure consistency across different cases, the disorder values are normalized against a reference variance, $\sigma^2_{\max}$, computed from a normally distributed set of indices:

$$\sigma^2_{\max} = \mathrm{Var}\left(\tilde{I}\right), \tag{6.3.4}$$

where $\tilde{I}$ is a synthetic dataset generated as

$$\tilde{I} = \mathrm{round}\left(\frac{M}{2} + \frac{M}{4} \cdot N(0,1)\right). \tag{6.3.5}$$

Here, M is the total number of unique indices, that is 1682 trajectories. This yields a disorder metric between $[0, 1]$. The final normalized disorder metric for each point is given by

$$D_i = \frac{\sigma_i^2}{\sigma^2_{\max}}. \tag{6.3.6}$$

Since some points may have an artificially assigned variance of zero due to a lack of neighbors, the total disorder across all points is computed by averaging only the nonzero disorder values

$$D_{\text{total}} = \frac{1}{N_{\text{valid}}} \sum_{i \in \{D_i > 0\}} D_i. \tag{6.3.7}$$

Figure 6.8 shows an example of the maximum possible variation of trajectories imposed on the scatter points in the $1kA$ case. This was used to find the maximum disorder Eq. 6.3.4 of field line mixing to normalize the disorder calculated in Eq. 6.3.3, which yields Eq. 6.3.6. The mixing of indices is so even that the figure appears a greenish gray.

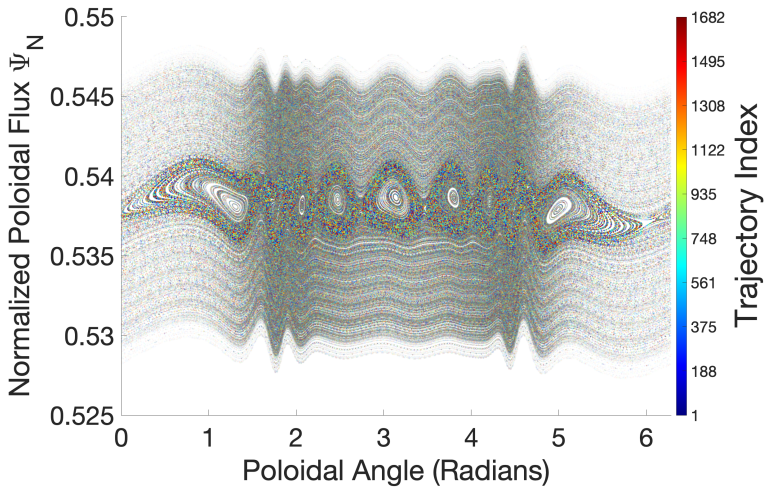

Figure 6.8: $1kA$ case with trajectory indices randomly uniformly distributed across scatter points.

These disorder maps provide a spatial representation of index mixing, where darker regions indicate high disorder and lighter regions indicate more uniformity in index values.

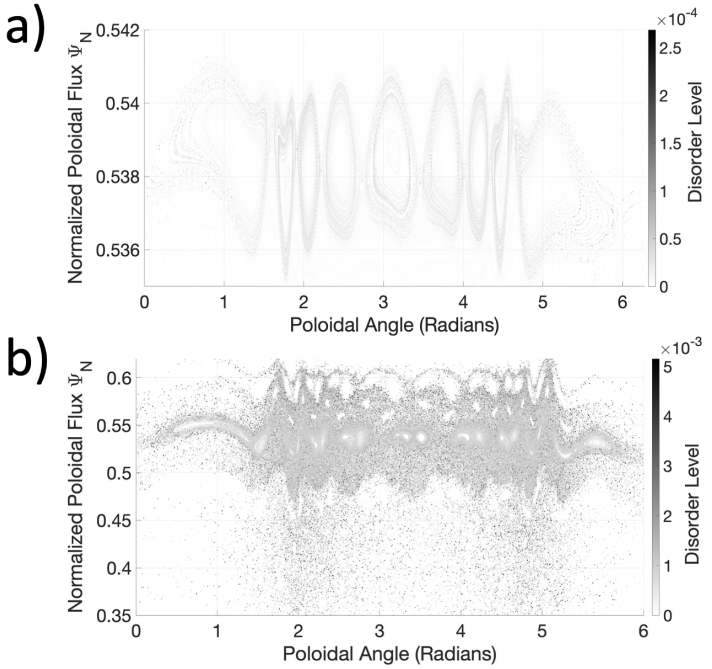

Figure 6.9: Disorder maps of the 1 kA and 16 kA (NCC) cases.

Figure 6.9 shows the disorder plotted for a) the lowest NCC current case $1kA$ and b) the highest NCC current case $16kA$. For small current, the mixing of field line trajectories only happens in the outside edges of the magnetic island surfaces while the poloidal flux surfaces above and below the magnetic island regions indicate zero disorder. Interestingly, the O-points also show little to no disorder, which is consistent with the view that field stochasticity (and related unstable electron trajectories) is most pronounced around island X-points. The overall magnitude of the disorder in the low current case is quite small, being at most 3×10^{-4}. Figure 6.9 b) shows a greatly increased mixing of the field line trajectory throughout the entire region for the highest current case. Yet again, the magnetic island O-points show little to no disorder, but now the disorder has increased by an order of magnitude to 5×10^{-3}.

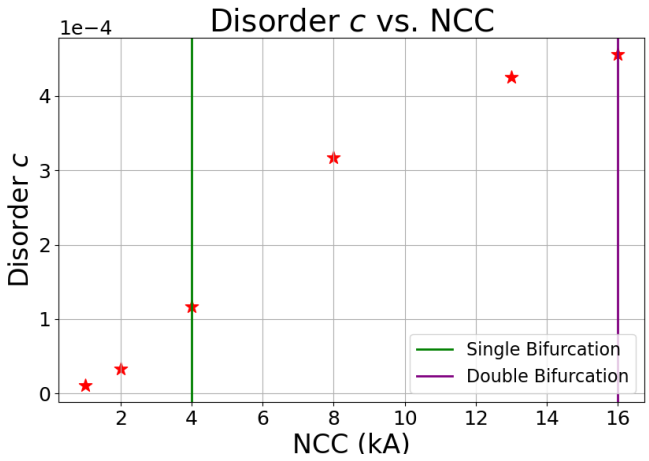

Figure 6.10

Figure 6.10 shows the average disorder calculated from the field line mixing for each Poincaré map as a function of perturbation strength. Again, vertical lines on this plot indicate the NCC currents that leads to a single and a double bifurcation. Just like q_p, disorder monotonically increases with increasing current perturbation. The functional shape of the growth seems almost inverse of what is seen in Figure 6.4, where Figure 6.10 seems to invert concavity at the $8kA$ case.

6.4 Discussion on Poloidal Flux as a Distribution

To help understand the idea of poloidal flux as a distribution, we start with ideal MHD and the force balance equation 6.3.1, which comes from the MHD momentum equation assuming no net electric field inside the plasma, no plasma flow, and isotropic pressure. A short derivation of this equation is provided in the Appendix, D.

$$\Delta^* \Psi = -\mu_0 R J_\phi \tag{6.4.1}$$

where $\Delta^* \equiv \frac{\partial^2}{\partial Z^2} + R\frac{\partial}{\partial R}\left(\frac{1}{R}\frac{\partial}{\partial R}\right)$and using a Green's function integration, we can obtain a solution for the poloidal magnetic field flux Ψ

$$\Psi(R, Z) = \int_{\Omega} G(R', Z', R, Z)\, J_{\phi}(R', Z')\, dR'\, dZ'. \tag{6.4.2}$$

Here, J_ϕ is the toroidal plasma current density and μ_0 is the magnetic permittivity and R and Z are the cylindrical coordinates representing the major radius and vertical position, respectively, in a poloidal cross section.. Equation 6.4.2 can be used to solve for the poloidal magnetic flux in ideal MHD equilibria. In the most basic case, where profiles are uniform and the geometry is symmetric, the poloidal flux surfaces take the form of concentric circles. Below is a representation of the poloidal flux under such idealized conditions.

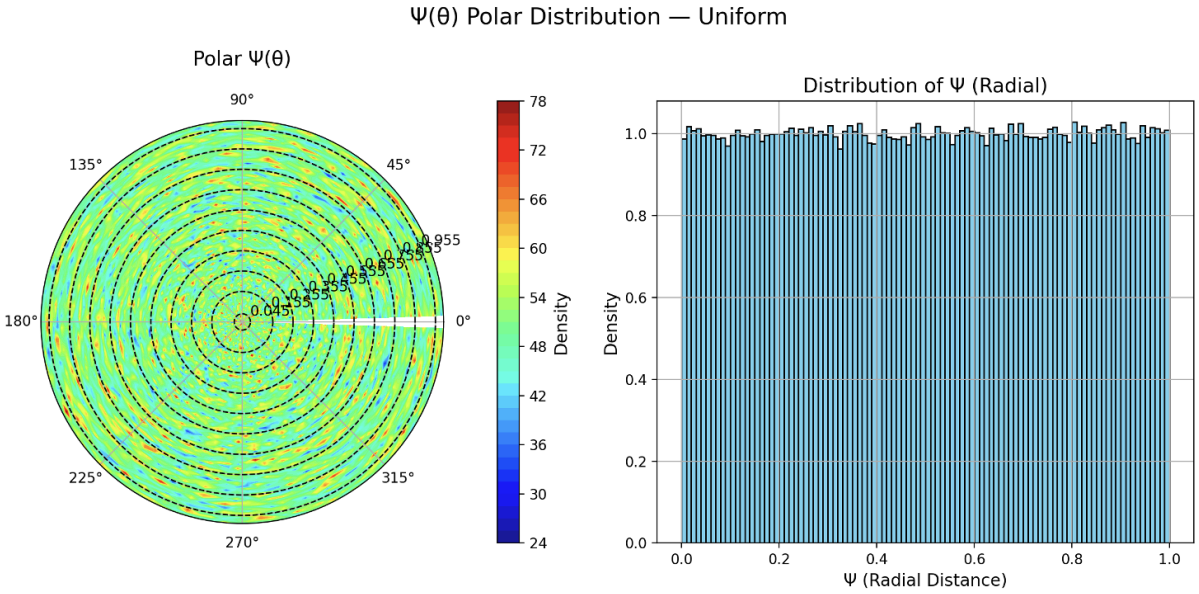

Figure 6.11: Uniform distribution of poloidal flux put into the poloidal plane with contour surfaces in black.

Figure 6.11 was generated by taking a uniform distribution (representing the poloidal flux) and placing it into the poloidal $\hat{r} \times \hat{\theta}$ plane. The resulting flux contours form concentric circles, as expected from a perfectly balanced, unperturbed plasma. While flux surfaces would generally follow the overall shaping of the plasma (e.g., D-shaped boundaries in NSTX-U), the concept of nested and smooth flux surfaces still applies. We now consider

more realistic conditions relevant to the NSTX-U simulation. If the nonaxisymmetric perturbations are included, which means $\tilde{J}_\phi \neq 0$ and therefore $\tilde{B}_R = -\frac{1}{R}\frac{\partial \tilde{\Psi}}{\partial Z}$, $\tilde{B}_Z = \frac{1}{R}\frac{\partial \tilde{\Psi}}{\partial R}$, and $\delta B_\phi = 0$, following similar steps as in D, we arrive at

$$\Delta^*(\Psi + \tilde{\Psi}) = -\mu_0 R(J_\phi + \tilde{J}_\phi). \tag{6.4.3}$$

where $\tilde{\Psi}$ and $\tilde{J}_\phi$ are the perturbation components of the poloidal flux and the toroidal current density, respectively.

Before we proceed, we would like to point out that recent studies have highlighted how magnetic island O-points may arise from localized current filaments. For instance, [166] discusses the formation and growth of islands as a result of tearing mode instabilities driven by current gradients. Real-time diagnostics developed in [167] rely on magnetic perturbations caused by current filaments to detect island structures, underscoring their physical link. The simulations in [168] explore current sheet formation and the emergence of magnetic islands from nonlinear filament dynamics. Similarly, [169] presents experimental evidence of magnetic islands in LHD plasmas that correlate with filamentary current structures. Together, these studies reinforce the interpretation of magnetic island O-points as manifestations of localized current filaments. This approach of considering and analyzing current filaments may help reveal more on island and transport dynamics. With the inclusion of nonaxisymmetric perturbations, known to create magnetic islands, and assuming that island dynamics can be associated with current filaments (i.e., none of the current filaments are artificially introduced due to particle beams or anything other than the perturbations creating the magnetic islands), then equation 6.4.3 can be rewritten by including current filaments in the following way

$$\Delta^*(\Psi + \tilde{\Psi}) = -\mu_0 R(J_\phi + \tilde{J}_\phi) - \mu_0 R \sum_i I_i \delta(R - R_i)\delta(Z - Z_i). \tag{6.4.4}$$

The solution to the above equation can be obtained with Green's functions as

$$\Psi(R,Z) + \tilde{\Psi}(R,Z) = \int_{\Omega} G(R',Z',R,Z)\, J_{\phi}(R',Z')\, dR'\, dZ' + \int_{\Omega} G(R',Z',R,Z)\, \tilde{J}_{\phi}(R',Z')\, dR'\, dZ' + \sum_{i=1}^{N} G(R_i,Z_i,R,Z)\, I_i. \tag{6.4.5}$$

Here, I_i is a toroidal current filament located at $(R = R_i, Z = Z_i)$ and $\delta(\cdot)$ is Dirac's delta function. Thus, with a coordinate transformation from Z to poloidal angle θ and with knowledge of the locations of O-points and X-points as the locations of all current filaments i, then a possibly clearer picture could be obtained using a distribution perspective.

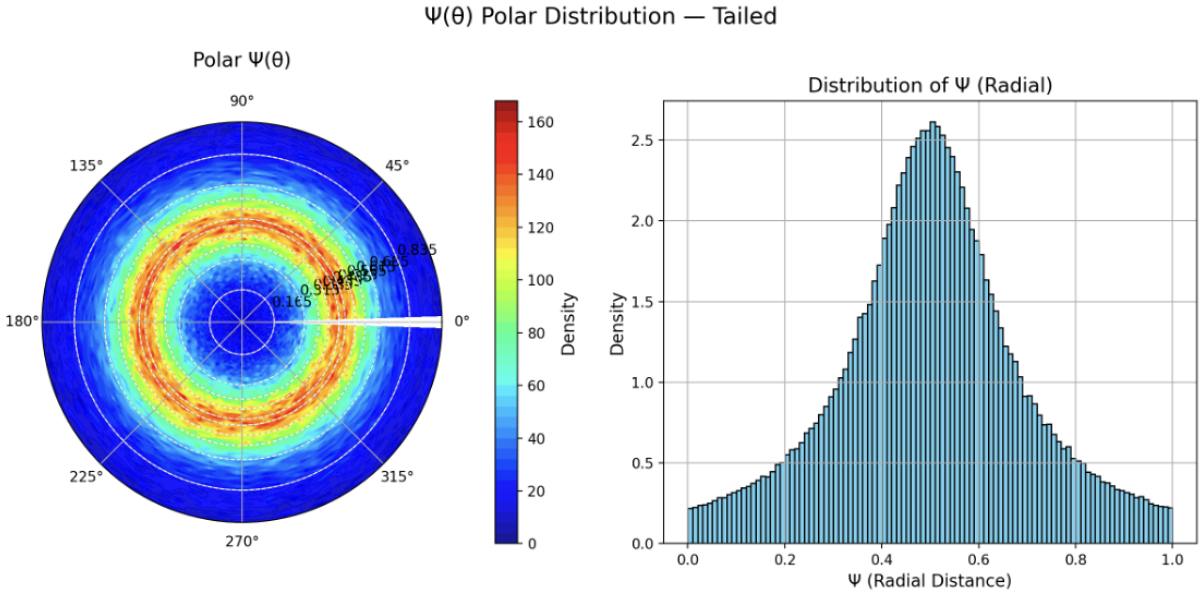

Figure 6.12: Lévy type distribution of poloidal flux put into the poloidal plane with white lines indicating the contour surfaces.

Figure 6.12 shows flux surfaces and contour surfaces in white created from a $q_p \geq 5/3$ Lévy type distribution. This indicates that, in a situation such as the 16 kA perturbation, we no longer have evenly spaced concentric circles, and the poloidal magnetic flux surfaces become a very dense single region. We present these equations, though not newly derived, to help better understand this picture of the poloidal flux as distribution function. To the best of our knowledge, this is a novel perspective only introduced here and in [149].

6.5 Conclusion of Magnetic Field Line Analysis

It was demonstrated how nonaxisymmetric perturbations in magnetically confined plasmas—particularly the 9/3 mode in NSTX-U simulations—generate magnetic islands, bifurcations, and ultimately lead to the onset of stochastic magnetic field regions. Using Poincaré maps and normalized poloidal flux histograms, we revealed how increasing perturbation current intensifies the departure from classical nested flux surfaces. The normalized poloidal flux, Ψ_N, was treated as a statistical distribution, with deviations from Maxwellian-like behavior captured by a nonextensive q-Gaussian fit. This approach is strengthened by literature establishing the presence of non-Gaussian and heavy-tailed behavior in both particle transport and flux observables across a range of plasma conditions [144, 146, 149]. Our findings echo such results, suggesting that the statistical behavior of poloidal flux under perturbation may be part of a broader class of nonextensive plasma phenomena. We briefly discussed the theoretical underpinning of how the poloidal flux may be seen as a distribution in both the simple ideal MHD and the non-ideal, nonaxisymmetric perturbative case. As the perturbation increased, the fitted q_p parameter also increased, indicating a transition from subdiffusion, to classical diffusion to super-diffussion and eventually crossing the threshold q_p needed for Lévy flights. This trend was correlated with island bifurcations and the stochasticization of magnetic surfaces. This study provides further evidence for the use of a statistical transport framework similar to those seen in studies of Lévy transport and fractional diffusion [150, 151, 152].

In addition to this statistical characterization, a novel trajectory-based disorder metric was introduced using KD-tree spatial analysis of colored field-line indices. This metric quantitatively described how much individual field lines positions diverged from their initial locations under the action of the perturbation. We observed a consistent monotonic increase in disorder as a function of perturbation current strength, with peak disorder occurring in regions of heavy island overlap causing stochasticization of magnetic surfaces. Notably, even

under high perturbations, island O-points remained relatively ordered, implying resilience in the core of the island structures. This framework, through both q_p and spatial disorder, allows for quantifying how changes in the magnetic topology may lead to anomalous diffusion. This can also connect to the Fractional Laplacian Spectral Method (FLSM), similarly the to analysis done in chapter 5. The final scaling that would be needed is connecting the Hilbert space vector reference scale ν to spatial scales in magnetically confined fusion plasma, such as the electron gyroradius ($\rho_e \sim 10^{-5}$–10^{-4} m), ion gyroradius ($\rho_i \sim 10^{-3}$–10^{-2} m), average magnetic island width (typically $\sim 10^{-2}$–10^{-1} m), the overall device radius from the plasma core to the wall (on the order of 1–2 meters for machines like NSTX-U or DIII-D), the connection length to the edge of the plasma (tens to hundreds of meters), and the mean free path along a magnetic field line (ranging from hundreds of meters up to several kilometers, depending on collisionality).

The alignment between our results and recent studies highlighting the role of field-line complexity, stochasticity, and their distinction from particle chaos, underscores the importance of treating magnetic field structures as evolving statistical objects. Our work supports the idea that the field line structure itself, not just test particle dynamics, may be governed by similar nonextensive principles, advancing the ongoing conversation around fractional modeling and self-organized criticality in fusion-relevant plasmas. Together, these tools and insights not only provide quantitative diagnostics for magnetic disorder but also situate this work within a growing body of literature advocating for nonlocal, non-Gaussian, and fractional approaches to turbulent plasma transport.

Chapter 7

Concluding Remarks

Summary of Results and Physical Significance

This dissertation explored the connections between anomalous diffusion, nonextensive statistics, fractional derivative operators, and spectral models in plasma physics. A detailed theoretical discussion was presented that clarified the relationship between nonextensive statistical mechanics, nonlinear differential equations, and fractional transport models. Specifically, it was shown that a fractional derivative diffusion equation (with nonlinear fraction γ) is connected to nonextensive statistics (with nonextensivity parameter q) by the following scaling relation $\gamma = 2s = \frac{3-q}{q-1}$. Similarly, the nonlinear diffusion equation (with nonlinear exponent ν is connected to the nonextensivity parameter q through the following scaling relation$\nu = 2 - q$. All three of these models are connected to the description of anomalous diffusion via scaling relationships with the power α on the time evolution of the Mean Squared Displacement (MSD) $MDS \propto \tau^{\alpha}$. A diagram summarizing the scaling relations across the different models of anomalous diffusion was provided in Fig. 2.9.

We further discussed that the distinguishing difference between power-law–tail distributions with finite variance ($q < 5/3$) from true Lévy distributions with infinite variance ($q \geq 5/3$) can be given some quantifiable theoretical interpretation with Lévy flights as very large step-size displacements. Specifically, we proposed that the scale of Lévy flights $\lambda_{\text{Lévy}}$ far exceeds the effective transport length scale λ_q, which far exceeds the mean free path λ_{mfp}, i.e. $\lambda_{mfp} \ll \lambda_q \ll \lambda_{\textbf{Lévy}}$. The key difference between $\lambda_{\text{Lévy}}$ and λ_q is that the latter corresponds to large jumps that still remain bounded by the system size L. Building on this

physical picture, arguments were made to connect the fractional Laplacian (with fraction s) to nonextensive statistics through the scaling relations $s = \frac{3-q}{2q-2}$ for $q \geq 5/3$ and $s = \frac{3-q}{2}$ for $q < 5/3$ (see Figure 2.9). This was used to map between statistical quantities calculated from experiments and simulations and spectral frameworks, highlighting a path to modeling anomalous diffusion via a physics-informed Anderson-type Hamiltonian with a fractional Laplacian.

This theoretical framework was first applied to the analysis of PK-4 microgravity dusty plasma experiments, where clouds of charged micron-sized particles were suspended in low temperature plasma with the help of a polarity switched external electric field. Using Tsallis q-Gaussians, we quantified the nonequilibrium behavior of dust particle trajectories in both the position and velocity domains. We found directional anisotropy in the diffusion coefficients, with particle motion parallel to the electric field being more superdiffusive than in the cross-field direction. In several pressure-current cases, the parallel transport was shown to follow Lévy-like dynamics, while the perpendicular motion followed a bi-modal distribution suggesting a superposition of classical diffusive and superdiffusive behavior. The nonequilibrium parameters q_p and q_v varied with direction and plasma conditions, as was shown in Table 4.2, with $q_{v\parallel}$ typically closer to 1, i.e. equilibrium, than $q_{v\perp}$. This indicates that energy exchange along the direction of the field brings the system closer to thermal equilibrium. In contrast, the cross-field component remained further from equilibrium due to the restoring force of the ion wakefields surrounding the dust grains. These findings support the hypothesis that enhanced diffusion in position space can coexist with system equilibrium in velocity space.

The PK-4 study also revealed the existence of spatial temperature gradients and subdomain-dependent q_v values, reinforcing the interpretation that the dust clouds in PK-4 are strongly anisotropic, nonequilibrium systems. In smaller domains, single q-Gaussian fits to cross-field data became viable, suggesting localized quasi-equilibria. The dust particle motion was shown to be shaped by the ion streaming velocity resulting from the external electric

field, the anisotropies of the ion wakefield structure, and the local interaction between dust particles and regions of positive space charge within the ion wakefield. We expect that the complex combination of these effects causes the intermittent large dust jumps that constitute Lévy-like dynamics.

The analysis of dusty plasma experiments was then extended to consider disorder and scaling lengths in PK-4. To quantify dimensionless disorder, a spatial disorder metric bounded between $[0, 1]$ was developed based on an idealized perfect lattice and uniformly disordered lattice. To understand the spatial scales characteristic of the dust diffusion, particle step-size distributions were decomposed into "mean," "large," and "clustered large" jump components. It was observed that clustered large jumps tended to occur in sequence, covering two interparticle distances, with about 20% of large jumps being followed by another within ten frames. This "clustering" behavior corresponds to enhanced transport at slightly larger spatial scales and matches the superdiffusive transport seen in the trajectory histogram analysis. We found that as pressure increased, system disorder decreased, which makes sense as the increase in pressure leads to higher frequency of collisions between dust and neutral atoms from the background gas. This, effectively, acts as a cooling mechanism by decreasing the dust kinetic temperature and improving order. These results agree with the pair correlation study by Gehr et al. [**?**], which identified increased alignment of the dust particles into crystalline filamentary structures at higher pressures. A positive correlation (with modest statistical significance) was found between disorder and the prevalence of clustered jumps, supporting the hypothesis that increased disorder facilitates instability and rare, large-scale motion.

The observed nonlocal diffusion and disorder in each dusty plasma experiment were then used as inputs to the Fractional Laplacian Spectral Method (FLSM), which models anomalous transport using a fractional Laplacian to represent nonlocality and a disordered potential energy to capture stochastic effects. A wide parameter sweep of over 55,000 combinations of the nonlocality fractional Laplacian exponent s, the disorder strength of potential barriers

c, and the Hilbert space reference scale ν was performed to produce high-resolution maps of transport probability. A key result was the discovery of "islands of transport"—regions in Hilbert space where nonlocality and disorder constructively interact to enhance transport. These transport islands were separated by forbidden length scales where probability for transport is suppressed. These spectral features were mapped to physical scales observed in the PK-4 dusty plasma experiments using step-size classifications and statistical measures of disorder and temperature. The model predicts scale-dependent transport consistent with experimental observations: superdiffusive jumps aligned with the electric field at both small and large scales, and suppressed cross-field motion. These findings support the interpretation of PK-4 as a mesoscopic analog system capable of probing complex structural transitions. These studies suggest that scale-dependent interplay between disorder and nonlocality governs the structure of transport in strongly coupled nonequilibrium systems.

Finally, this framework was extended to magnetically confined fusion plasmas using M3D-C1 simulations of NSTX-U equilibrium and TRIP3D simulations of 3D magnetic field perturbations. Here, the increasing magnitude of nonaxisymmetric perturbation currents—specifically the 9/3 mode—were shown to induce magnetic islands, successive island bifurcations, and the formation of stochastic regions in the poloidal flux surfaces. The normalized poloidal flux Ψ_N was treated as a statistical distribution, and its deviation from Gaussianity was captured using a fitted q_p-Gaussian. As the perturbation current increased, the q_p parameter rose monotonically, suggesting a transition from ordered flux surfaces to heavy-tailed distributions as the magnetic field topology became increasingly disordered. We conjecture that, for strongly magnetized electrons, these topological changes will lead to a crossover from subdiffusion to classical diffusion to superdiffusion, and even Lévy flights. In parallel, a KD-tree spatial disorder metric was applied to field-line trajectories, revealing increasing divergence of positions among neighboring lines. Both metrics indicated growing magnetic complexity and stochasticity with increasing perturbation strength, with island O-points remaining relatively ordered even under high distortion.

These results strongly agree with literature on self-organized criticality, Lévy-type transport, and fractional modeling in magnetized and fusion plasmas. Moreover, the consistent rise in q_p and spatial disorder in perturbed equilibria suggests that these tools may serve as practical diagnostics for topological instability or disruption precursors. The dual approach—capturing both non-Gaussian flux distributions and spatial disorder—offers a richer framework for interpreting magnetic field complexity in modern fusion devices.

Together, these studies help understand anomalous diffusion better: from dusty plasmas to magnetized plasma, anomalous diffusion and nonequilibrium behavior can be described through a combination of nonextensive statistics, fractional operators, and scale-resolved transport diagnostics. This approach should be further explored to help bridge microscopic fluctuations, mesoscopic structures, and macroscopic topology, to help offer a unified and interpretable framework for plasma transport across disciplines.

Limitations

While our findings are substantial, there do exist limitations. First, the PK-4 data was constrained by frame rate and resolution, limiting analysis of very short or very long time behavior or more precise spatial resolution . The Fractional Laplacian Spectral Method and extended state conjecture are relatively novel and would benefit from even longer simulation time as well as increased theoretical understanding. In NSTX-U, simulations relied on M3D-C1 equilibrium outputs, and nonlinear turbulence or kinetic effects were not explicitly modeled. Furthermore, while we established empirical connections between q-parameters and physical observables, a formal theoretical derivation connecting q to kinetic theory parameters remains an open question. In addition, many of these scaling relations need experimental validation.

Future Work

This dissertation opens several promising directions for future work:

- **Theoretical**: Derive the explicit dependence of the q-parameter on physical plasma parameters for a given plasma condition. Explore how it relates to transport coefficients in the Balescu–Lenard or Fokker–Planck equations. Find a relation between q-Gaussians and correlation distributions in the BBGKY Hierarchy. Find a relation connecting q_p and q_v starting with a nonextensive form of the Einstein relation. Find if a possible derivation of q-Gaussians in both spatial q_p and velocity q_p space can be performed from the full phase-space Fokker-Planck Equation with collisions.

- **Computational**: Test kinetic simulations of the two-stream instability to see if after a long time the distribution relaxes to steady-state q-Gaussian distribution. Extend the fractional Laplacian model to 2D/3D PIC simulations.

- **Experimental**: Use spectroscopy in low-temperature plasmas to explore Tsallis-distributed electron backgrounds. Measure how emission line broadening compares with Maxwellian and q-Gaussian input populations.

- **Application to Fusion**: Implement the q_p and spatial disorder metrics in time-resolved MHD simulations of tokamak plasmas. Assess whether early increases in q_p could actually serve as precursors for disruptions. Apply the Fractional Laplacian Spectral Method as a model for probability of transport.

- **Cross-domain**: Use PK-4's mesoscopic observability to explore condensed matter parallels in a controlled plasma setting using the statistical and spectral models applied in this dissertation.

In summary, this dissertation investigated the deep connections between anomalous diffusion, nonextensive statistics, fractional derivative operators, and spectral models in plasma physics. The theoretical foundations of these topics and their interrelations were presented in a unified framework, offering a more comprehensive understanding of anomalous transport

processes. A thorough literature review established the robustness of nonextensive statistics and highlighted its potential for broader application across plasma regimes.

These theoretical tools were then applied to two distinct but complementary domains: dusty plasma in the PK-4 experiment aboard the International Space Station, and magnetic confinement fusion plasmas in the NSTX-U tokamak. In PK-4, nonextensive statistics were successfully used to quantify nonequilibrium dynamics, revealing novel insights such as the superdiffusion in position space can coexist with close-to-classical diffusion in velocity space, which indicates equilibrium, and pressure acting as an effective inverse temperature, and connections to other plasma environments, such as the solar wind. The Fractional Laplacian Spectral Method was significantly advanced through large-scale parameter scans, yielding detailed transport spectra that helped reveal the role of nonlocal operators in disordered systems.

Finally, the application of nonextensive statistics to magnetic field lines in NSTX-U simulations offered a new statistical perspective on magnetic topology and transport. By quantifying normalized poloidal flux distributions and spatial field-line disorder, we provided tools that may contribute to disruption prediction and deeper insight into magnetic structure formation. With both mathematical elegance and physical relevance, the frameworks developed here offer a unified path forward for describing diffusion and transport in plasmas, bridging microscopic kinetics with macroscopic behavior across multiple sub-fields.

References

[1] Donald Gary Swanson. *Plasma Kinetic Theory*. Series in Plasma Physics. CRC Press / Taylor & Francis, Boca Raton, FL, 1st edition, 2008.

[2] Constantino Tsallis. *Introduction to Nonextensive Statistical Mechanics: Approaching a Complex World*. Springer, New York, 2009th edition, 2009.

[3] Constanze Liaw. Approach to the Extended States Conjecture. *Journal of Statistical Physics*, December 2013.

[4] Nadine Tarantino, Jean-Yves Tinevez, Elizabeth Faris Crowell, Bertrand Boisson, Ricardo Henriques, Musa Mhlanga, Fabrice Agou, Alain Israël, and Emmanuel Laplantine. Tnf and il-1 exhibit distinct ubiquitin requirements for inducing nemo–ikk supramolecular structures. *Journal of Cell Biology*, 2014.

[5] Andy Reynolds. Liberating lévy walk research from the shackles of optimal foraging. *Physics of Life Reviews*, 2015.

[6] M. Benhamou. Lecture on the anomalous diffusion in condensed matter physics. *Materials and Devices*, 2018.

[7] Yan Feng, J. Goree, and Bin Liu. Identifying anomalous diffusion and melting in dusty plasmas. *Physical Review E*, 2010.

[8] Bin Liu, J. Goree, and Yan Feng. Non-gaussian statistics and superdiffusion in a driven-dissipative dusty plasma. *Physical Review E*, 2008.

[9] Fernando A. Oliveira, Rogelma M. S. Ferreira, Luciano C. Lapas, and Mendeli H. Vainstein. Anomalous diffusion: A basic mechanism for the evolution of inhomogeneous systems. *Frontiers in Physics*, 2019.

[10] Till Daniel Frank. *Nonlinear Fokker-Planck equations: fundamentals and applications*. Springer Series in Synergetics. Springer, 2005.

[11] J. L. Padgett, E. G. Kostadinova, C. D. Liaw, K. Busse, L. S. Matthews, and T. W. Hyde. Anomalous diffusion in one-dimensional disordered systems: a discrete fractional laplacian method. *Journal of Physics A: Mathematical and Theoretical*, April 2020.

[12] E. G. Kostadinova, R. Banka, J. L. Padgett, C. D. Liaw, L. S. Matthews, and T. W. Hyde. Fractional laplacian spectral approach to turbulence in a dusty plasma monolayer. *Physics of Plasmas*, 2021.

[13] D. G. Aronson. The porous medium equation. In A. Fasano and M. Primicerio, editors, *Nonlinear Diffusion Problems*, volume 1224 of *Lecture Notes in Mathematics*, pages 1–46. Springer, Berlin, Heidelberg, 1986.

[14] Nahla Ben Salah. Some properties of q-gaussian distributions. https://arxiv.org/abs/2101.00516.arXiv:2101.00516 [math.PR], 2021. Preprint.

[15] Zahra Ghannad. Identification of time scales of the violation of the stokes–einstein relation in yukawa liquids. *Physics of Plasmas*, 28(4), April 2021.

[16] Constantino Tsallis. Possible generalization of boltzmann-gibbs statistics. *Journal of Statistical Physics*, 52(1):479–487, 1988.

[17] J. A. S. Lima, R. Silva, and A. R. Plastino. Nonextensive thermostatistics and the H theorem. *Physical Review Letters*, 86(14):2938–2941, April 2001.

[18] Muhammad Bilal, Aman ur Rehman, Mushtaq Ahmad, Muhammad Ahsan Shahzad, Muhammad Sarfraz, and Shahzad Mahmood. Linear analysis of whistler mode instability in anisotropic q-nonextensive distributed plasmas: a numerical approach. *Physica Scripta*, 98(9):095607, August 2023.

[19] Ralf Metzler and Joseph Klafter. The random walk's guide to anomalous diffusion: a fractional dynamics approach. *Physics Reports*, 339(1):1–77, 2000.

[20] Igor Podlubny. *Fractional Differential Equations: An Introduction to Fractional Derivatives, Fractional Differential Equations, to Methods of Their Solution and Some of Their Applications*, volume 198 of *Mathematics in Science and Engineering*. Academic Press, San Diego, 1999.

[21] Jiulin Du. Nonextensivity in nonequilibrium plasma systems with Coulombian long-range interactions. *Physics Letters A*, 329(4-5):262–267, August 2004. Publisher: North-Holland.

[22] Yu Haining and Du Jiulin. The nonextensive parameter for nonequilibrium plasmas in magnetic field. *Annals of Physics*, 350:302–309, November 2014. arXiv:1403.1760 [cond-mat, physics:physics].

[23] Ran Guo and Jiulin Du. Transport coefficients of the fully ionized plasma with kappa-distribution and in strong magnetic field. *Physica A: Statistical Mechanics and its Applications*, 523:156–171, June 2019.

[24] Du Jiulin. Transport coefficients in Lorentz plasmas with the power-law kappa-distribution. *Physics of Plasmas*, 20(9):092901, September 2013.

[25] Lan Wang and Jiulin Du. The diffusion of charged particles in the weakly ionized plasma with power-law kappa-distributions. *Physics of Plasmas*, 24(10):102305, October 2017.

[26] Yue Wang and Jiulin Du. The current density and transport coefficients in the fully ionized plasma with q-distributions in nonextensive statistics. *Physica A: Statistical Mechanics and its Applications*, 523:757–764, June 2019.

[27] Yue Wang and Jiulin Du. Effect of magnetic field on transports of charged particles in the weakly ionized plasma with power-law q-distributions in nonextensive statistics. *Physica A: Statistical Mechanics and its Applications*, 541:123281, March 2020.

[28] Yue Wang and Jiulin Du. The effect of magnetic field on the viscosity in the weakly ionized and magnetized plasma with power-law q-distributions in nonextensive statistics. *Physica A: Statistical Mechanics and its Applications*, 527:121120, August 2019.

[29] Xiaoxuan Ji and Jiulin Du. Diffusion and heat conductivity in the weakly ionized plasma with power-law q-distributions in nonextensive statistics. *Physica A: Statistical Mechanics and its Applications*, 523:292–300, June 2019.

[30] I. S. Elkamash and I. Kourakis. Electrostatic wave breaking limit in a cold electronegative plasma with non-Maxwellian electrons. *Scientific Reports*, 11(1):6174, March 2021. Publisher: Nature Publishing Group.

[31] Danny Summers and Richard M. Thorne. The modified plasma dispersion function. *Physics of Fluids B: Plasma Physics*, 3(8):1835–1847, August 1991.

[32] J. A. S. Lima, R. Silva, and Janilo Santos. Plasma oscillations and nonextensive statistics. *Physical Review E*, 61(3):3260–3263, March 2000. Publisher: American Physical Society.

[33] R. Silva, J. S. Alcaniz, and J. A. S. Lima. Constraining nonextensive statistics with plasma oscillation data. *Physica A: Statistical Mechanics and its Applications*, 356(2-4):509–516, October 2005. arXiv:cond-mat/0603175.

[34] M Taherimoghadam, I Motie, A Bakhshayeshi, and T Mirzaye. Relativistic effects on dust grain charging in nonequilibrium dusty plasma with relativistic tsallis distribution. *Physics of Plasmas*, 26(11):113704, 2019.

[35] Tayebeh Abbaszadeh and Hossein Zahed. Kinetic approach on the dust ion-acoustic wave propagation in a non-extensive distributed dusty plasma. *Contributions to Plasma Physics*, 61(9):e202100049, 2021.

[36] José F. Nieves and John D. Verges. Simplified calculations of plasma oscillations with non-extensive statistics. *The European Physical Journal D*, 74(9):194, September 2020.

[37] Xiao-Chang Chen and Xiao-Qing Li. Comment on "plasma oscillations and nonextensive statistics". *Physical Review E*, 86(6), December 2012.

[38] M. Hashemzadeh. Nonextensive statistics and skin depth of transverse wave in collisional plasma. *Physics of Plasmas*, 23(5):052113, May 2016.

[39] V. Muñoz. A nonextensive statistics approach for Langmuir waves in relativistic plasmas. *Nonlinear Processes in Geophysics*, 13(2):237–241, June 2006. Publisher: Copernicus GmbH.

[40] Xiao-Ling Liu and Xiang-Qun Li. The full zakharov equations in nonextensive q-plasma. *Physics of Plasmas*, 21(2):022306, 2014.

[41] Muhammad Bilal, Aman ur Rehman, Shahzad Mahmood, Muhammad Ahsan Shahzad, and Muhammad Sarfraz. Landau damping of ion-acoustic waves with simultaneous effects of non-extensivity and non-thermality in the presence of hybrid cairns–tsallis distributed electrons. *Contributions to Plasma Physics*, 2023.

[42] E. Saberian and A. Esfandyari-Kalejahi. Kinetic theory of acoustic-like modes in nonextensive pair plasmas. *Astrophysics and Space Science*, 349(2):799–811, November 2013.

[43] Shalini, N. S. Saini, and A. P. Misra. Modulation of ion-acoustic waves in a nonextensive plasma with two-temperature electrons. *Physics of Plasmas*, 22(9), September 2015.

[44] B. Azarvand-Hassanfard, A. Esfandyari-Kalejahi, and M. Akbari-Moghanjoughi. Ion energy spectrum in expansion of plasmas with nonextensive electrons. *Results in Physics*, 7:4213–4221, 2017.

[45] Khalid Khan, Obaid Algahtani, Muhammad Irfan, and Amir Ali. Electron-acoustic solitary potential in nonextensive streaming plasma. *Scientific Reports*, 12(1), September 2022.

[46] Bruce M. Boghosian. Thermodynamic description of the relaxation of two-dimensional turbulence using Tsallis statistics. *Physical Review E*, 53(5):4754–4763, May 1996.

[47] Celia Anteneodo and Constantino Tsallis. Two-dimensional turbulence in pure-electron plasma: A nonextensive thermostatistical description. *Journal of Molecular Liquids*, 71(2):255–267, April 1997.

[48] M. Ghorbanalilu and S. Sadegzadeh. Particle-in-cell simulation of two-stream instability in the nonextensive statistics. *Laser and Particle Beams*, 32(3):419–425, 2014.

[49] Fernando Haas, Horst Fichtner, and Klaus Scherer. Electron holes in a regularized kappa background. *Nonlinear Processes in Geophysics*, 30(3):277–286, 2023.

[50] Khireddine Mebrouk, Leila Ait Gougam, and Mouloud Tribeche. Nonextensive statistical mechanics approach to electron trapping in degenerate plasmas. *Physica A: Statistical Mechanics and its Applications*, 451:525–532, June 2016.

[51] Mubarak Alqahtani, Nasser Demir, and Michael Strickland. Nonextensive hydrodynamics of boost-invariant plasmas. *The European Physical Journal C*, 82(10), October 2022.

[52] Shane Davis, Gabriel Avaria, and Alejandro Navarro. Single-particle velocity distributions of collisionless, steady-state plasmas must follow superstatistics. *Physical Review E*, 100(2):023205, 2019.

[53] F. E. M. Silveira and M. H. Benetti. Towards a physical interpretation of the deformation parametrization in nonextensive statistics: Evidence for a generalization of the number of degrees of freedom in a nonextensive gas of charged particles. *The European Physical Journal Plus*, 136(12), December 2021.

[54] Sergio Davis, Gonzalo Avaria, Biswajit Bora, Jalaj Jain, José Moreno, Cristian Pavez, and Leopoldo Soto. Kappa distribution from particle correlations in nonequilibrium, steady-state plasmas. *Physical Review E*, 108(6):065207, 2023.

[55] David J. McComas and George Livadiotis. Correlations and kappa distributions: Numerical experiment and physical understanding. *Entropy*, 27(4):375, 2025.

[56] M. M. Hatami. Nonextensive statistics and the sheath criterion in collisional plasmas. *Physics of Plasmas*, 22(1):013508, January 2015.

[57] Huibin Qiu, Zhenyu Zhou, Xingkun Peng, Xianyang Zhang, Yuqing Zhu, Yue Gao, Donghua Xiao, Haifeng Bao, Tianling Xu, Jia Zhang, Tianhui Huang, Jinmao Zhou, Zhiyi Ming, Pengfei Xiang, Hai Yang, Xiaofeng Wang, Dongyang Wu, and NCST Team. Initial measurement of electron nonextensive parameter with electric probe. *Physical Review E*, 101(4):043206, April 2020. Publisher: American Physical Society.

[58] Huibin Qiu, Donghua Xiao, Yue Gao, Xingkun Peng, Yuqing Zhu, Xianyang Zhang, Zhenyu Zhou, Weihong Xiong, Zhiyi Ming, Tianling Xu, Pengfei Xiang, Hai Yang, Jia Zhang, Tianhui Huang, and Jinmao Zhou. Sheath potential coefficient in plasma with nonextensive distribution. *AIP Advances*, 10(6):065135, June 2020.

[59] Gunjan Sharma, Rupali Paul, Kishor Deka, Rakesh Moulick, Sayan Adhikari, S. S. Kausik, and B. K. Saikia. Study of two-electron temperature plasma sheath using

non-extensive electron distribution in presence of an external magnetic field. *AIP Advances*, 13(1):015011, January 2023.

[60] Koji Kikuchi and Hiroshi Akatsuka. Reconsideration of Temperature Determined by the Excited-State Population Distribution of Hydrogen Atoms Based on Tsallis Entropy and Its Statistics in Hydrogen Plasma in Non-Equilibrium State. *Entropy*, 25(10):1400, October 2023. Number: 10 Publisher: Multidisciplinary Digital Publishing Institute.

[61] Mohamed El Bojaddaini, Mohamed El Kaouini, and Hassan Chatei. Sheath structure behavior in collisional non-extensive plasma with negative ions. *The European Physical Journal Plus*, 139(3):373, 2024.

[62] Zhipeng Liu and Jiulin Du. Dust acoustic instability driven by drifting ions and electrons in the dust plasma with Lorentzian kappa distribution. *Physics of Plasmas*, 16(12):123707, December 2009.

[63] Jingyu Gong and Jiulin Du. Dust charging processes in the nonequilibrium dusty plasma with nonextensive power-law distribution. *Physics of Plasmas*, 19(2):023704, February 2012.

[64] Utpal Kumar Samanta, Asit Saha, and Prasanta Chatterjee. Bifurcations of dust ion acoustic travelling waves in a magnetized dusty plasma with a q-nonextensive electron velocity distribution. *Physics of Plasmas*, 20(2):022111, February 2013.

[65] Moufida Benzekka, Nedjma Bouchemla, and Abderrzak Merriche. Nonlinear dust acoustic waves in nonuniform complex plasma under the effect of tsallis polarization force. *Physics of Wave Phenomena*, 31(4):348–357, 2023.

[66] Salim Benaiche, Mustapha Bacha, Abderrzak Merriche, and Rabia Amour. Effect of tsallis–gurevich distributed ions on nonlinear dust-acoustic oscillations in collisionless nonextensive plasma. *Contributions to Plasma Physics*, 2023.

[67] Z. Eljabiri, O. El Ghani, I. Driouch, and H. Chatei. Total secondary emission effect on the complex plasma sheath with superextensive electrons. *Journal of Plasma Physics*, 90(5):905900506, October 2024.

[68] V.M. Vasyliunas. A survey of low-energy electrons in the evening sector of the magnetosphere with ogo 1 and ogo 3. *Journal of Geophysical Research*, 73(9):2839–2884, 1968.

[69] M. P. Leubner. Fundamental issues on kappa-distributions in space plasmas and interplanetary proton distributions. *Physics of Plasmas*, 11(4):1308–1316, April 2004.

[70] R. A. Treumann, C. H. Jaroschek, and M. Scholer. Stationary plasma states far from equilibrium. *Physics of Plasmas*, 11(4):1317–1325, April 2004.

[71] Leonard F Burlaga and Adolfo F Viñas. Multiscale probability distributions of solar wind speed fluctuations at 1 au described by a generalized tsallis distribution. *Geophysical Research Letters*, 31(16):L16807, 2004.

[72] L. F. Burlaga and A. F.-Viñas. Tsallis distributions of the large-scale magnetic field strength fluctuations in the solar wind from 7 to 87 AU. *Journal of Geophysical Research: Space Physics*, 110(A7), 2005. _eprint: https://onlinelibrary.wiley.com/doi/pdf/10.1029/2005JA011132.

[73] Leonard F Burlaga and Adolfo F Viñas. Triangle for the entropic index q of non-extensive statistical mechanics observed by voyager 1 in the distant heliosphere. *Physica A: Statistical Mechanics and its Applications*, 361(1):173–179, 2006.

[74] George Livadiotis and David J McComas. Beyond kappa distributions: Exploiting tsallis statistical mechanics in space plasmas. *Journal of Geophysical Research: Space Physics*, 114(A11):A11105, 2009.

[75] George Livadiotis and David J McComas. Understanding kappa distributions: A toolbox for space science and astrophysics. *Space Science Reviews*, 175:183–214, 2013.

[76] Zhipeng Liu, Liyan Liu, and Jiulin Du. A nonextensive approach for the instability of current-driven ion-acoustic waves in space plasmas. *Physics of Plasmas*, 16(7):072111, July 2009.

[77] Mouloud Tribeche, R Amour, and P K Shukla. Ion acoustic solitary waves in a plasma with nonthermal electrons featuring tsallis distribution. *Physical Review E*, 85(3):037401, 2012.

[78] Viviane Pierrard and Marian Lazar. Kappa distributions: Theory and applications in space plasmas. *Solar Physics*, 267(1):153–174, 2010.

[79] G.P. Pavlos, L.P. Karakatsanis, and M.N. Xenakis. Tsallis non-extensive statistics, intermittent turbulence, soc and chaos in the solar plasma, part one: Sunspot dynamics. *Physica A: Statistical Mechanics and its Applications*, 391(24):6287–6319, December 2012.

[80] L.P. Karakatsanis, G.P. Pavlos, and M.N. Xenakis. Tsallis non-extensive statistics, intermittent turbulence, soc and chaos in the solar plasma. part two: Solar flares dynamics. *Physica A: Statistical Mechanics and its Applications*, 392(18):3920–3944, September 2013.

[81] Viviane Pierrard, Maximilien Péters de Bonhome, Jasper Halekas, Charline Audoor, Phyllis Whittlesey, and Roberto Livi. Exospheric solar wind model based on regularized kappa distributions for the electrons constrained by parker solar probe observations. *Plasma*, 6(3):36, 2023.

[82] Hadia Mushtaq, Kuldeep Singh, Sadia Zaheer, and Ioannis Kourakis. Nonlinear ion-acoustic waves with landau damping in non-maxwellian space plasmas. *Scientific Reports*, 14(1):13005, 2024.

[83] Kamel Ourabah. Demystifying the success of empirical distributions in space plasmas. *Physical Review Research*, 2(2):023121, 2020.

[84] S. Bouzat and R. Farengo. Effects of varying the step particle distribution on a probabilistic transport model. *Physics of Plasmas*, 12(12):122303, December 2005.

[85] Jean-Christophe Pain, Denis Teychenné, and Franck Gilleron. Self-consistent modelling of hot plasmas within non-extensive tsallis' thermostatistics. *The European Physical Journal D*, 65(3):441–445, 2011.

[86] H. J. Haubold and D. Kumar. Fusion yield: Guderley model and Tsallis statistics. *Journal of Plasma Physics*, 77(1):1–14, February 2011.

[87] Hui-Bin Qiu, Hai-Ying Song, and Shi-Bing Liu. Collisionless damping of geodesic acoustic mode in plasma with nonextensive distribution. *Physics of Plasmas*, 21(6), June 2014.

[88] Huibin Qiu, Donghua Xiao, Junjie Wu, Shengfa Wu, Chengjie Zhong, Xiaobin Li, Xingkun Peng, Youlong Yuan, Qilong Cai, Jinming Chang, Tianyi Hu, Zuozhi Hu, and Yuqing Zhu. Initial measurement of ion nonextensive parameter with geodesic acoustic mode theory. *Scientific Reports*, 12:3412, March 2022.

[89] Huibin Qiu, Zuozhi Hu, Shengfa Wu, Jiangcun Chen, Chengjie Zhong, Junjie Wu, Xiaobin Li, Donghua Xiao, Chunhui Shi, Junhui Liu, Wenjun Xiong, Tianyi Hu, Qilong Cai, and Youlong Yuan. Initial analytical theory of plasma disruption and experimental evidence. *Scientific Reports*, 13(1):9551, June 2023.

[90] P.K. Shukla. A survey of dusty plasma physics. *Physics of Plasmas*, 8(5):1791–1803, 2001.

[91] R. L. Merlino, J. R. Heinrich, S.-H. Hyun, and J. K. Meyer. Nonlinear dust acoustic waves and shocks. *Physics of Plasmas*, 19(5), March 2012.

[92] S. A. Khrapak, B. A. Klumov, P. Huber, V. I. Molotkov, A. M. Lipaev, V. N. Naumkin, A. V. Ivlev, H. M. Thomas, M. Schwabe, G. E. Morfill, O. F. Petrov, V. E. Fortov, Yu. Malentschenko, and S. Volkov. Fluid-solid phase transitions in three-dimensional complex plasmas under microgravity conditions. *Physical Review E*, 2012.

[93] Evdokiya G. Kostadinova, Emerson Gehr, Bradley Andrew, Lorin S. Matthews, Truell W. Hyde, and Abbie Terrell. Liquid plasma crystals on the iss. In *AIAA SCITECH 2023 Forum*. American Institute of Aeronautics and Astronautics, January 2023.

[94] M. G. Hariprasad, P. Bandyopadhyay, V. S. Nikolaev, D. A. Kolotinskii, S. Arumugam, G. Arora, S. Singh, A. Sen, and A. V. Timofeev. Self-sustained non-equilibrium coexistence of fluid and solid states in a strongly coupled complex plasma system. *Scientific Reports*, 12(1), August 2022.

[95] Alexei V. Ivlev, Philip C. Brandt, Gregor E. Morfill, Christoph Rath, Hubertus M. Thomas, Glenn Joyce, Vladimir E. Fortov, Andrey M. Lipaev, Vladimir I. Molotkov, and Oleg F. Petrov. Electrorheological complex plasmas. *IEEE Transactions on Plasma Science*, 38(4):733–740, April 2010. Conference Name: IEEE Transactions on Plasma Science.

[96] A. V. Ivlev, G. E. Morfill, U. Konopka, and M. Kretschmer. Electrorheology of complex plasmas. *Physical Review Letters*, 106(15):155001, 2011.

[97] M. Y. Pustylnik, S. A. Khrapak, A. G. Khrapak, M. H. Thoma, H. M. Thomas, G. E. Morfill, A. M. Lipaev, A. D. Usachev, V. I. Molotkov, O. F. Petrov, A. V. Zobnin, and V. E. Fortov. Electrorheological phenomena in dusty plasma. *Physical Review Research*, 2(3):033314, 2020.

[98] V. N. Tsytovich, U. De Angelis, R. Bingham, and D. Resendes. Long-range correlations in dusty plasmas. *Physics of Plasmas*, 1997.

[99] B. Smith, J. Vasut, T. Hyde, L. Matthews, J. Reay, M. Cook, and J. Schmoke. Dusty plasma correlation function experiment. *Advances in Space Research*, 2004.

[100] Matheus V. Correia, Emerson J. Freitas, Leonardo R. E. Cabral, and Clécio C. de Souza Silva. Structural phases of classical 2d clusters with competing two-body and three-body interactions. *Journal of Physics: Condensed Matter*, 35(41):415404, July 2023.

[101] Kashif Arshad, M. Lazar, Shahzad Mahmood, Aman ur Rehman, and S. Poedts. Kinetic study of electrostatic twisted waves instability in nonthermal dusty plasmas. *Physics of Plasmas*, 2017.

[102] O. F. Petrov, V. E. Fortov, O. S. Vaulina, A. V. Chernyshev, S. N. Antipov, A. V. Gavrikov, and I. A. Shakhova. Experimental study of dusty plasma kinetics. *Physica Scripta*, 2005.

[103] Bin Liu, J. Goree, M. Y. Pustylnik, H. M. Thomas, V. E. Fortov, A. M. Lipaev, A. D. Usachev, V. I. Molotkov, O. F. Petrov, and M. H. Thoma. Particle velocity distribution in a three-dimensional dusty plasma under microgravity conditions. In *AIP Conference Proceedings*, 2018.

[104] Yan Feng. *Microscopic dynamics in two-dimensional strongly-coupled dusty plasmas*. PhD thesis, The University of Iowa, 2010.

[105] E. Joshi, M. Y. Pustylnik, M. H. Thoma, H. M. Thomas, and M. Schwabe. Recrystallization in string-fluid complex plasmas. *Physical Review Research*, 5(1), March 2023.

[106] Sachin Sharma, Rauoof Wani, Prabhakar Srivastav, Meenakshee Sharma, Sayak Bose, Yogesh Saxena, and Sanat Tiwari. Observation of kolmogorov turbulence due to multiscale vortices in dusty plasma experiments. *Physics of Plasmas*, 31(12):123704, 2024.

[107] Mangilal Choudhary. A review on the vortex and coherent structures in dusty plasma medium. *Journal of Plasma Physics*, 91(1):E7, 2025.

[108] M.S. Murillo. Strongly coupled plasma physics and high energy-density matter. *Physics of Plasmas*, 11(5):2964–2971, 2004.

[109] A. V. Ivlev, G. E. Morfill, H. M. Thomas, C. Räth, G. Joyce, P. Huber, R. Kompaneets, V. E. Fortov, A. M. Lipaev, V. I. Molotkov, T. Reiter, M. Turin, and P. Vinogradov. First observation of electrorheological plasmas. *Physical Review Letters*, 100(9):095003, March 2008.

[110] Christopher Dietz, Johannes Budak, Tobias Kamprich, Michael Kretschmer, and Markus H. Thoma. Phase transition in electrorheological plasmas. *Contributions to Plasma Physics*, 61(10):e202100079, 2021. _eprint: `https://onlinelibrary.wiley.com/doi/pdf/10.1002/ctpp.202100079`.

[111] J. Beckers, J. Berndt, D. Block, M. Bonitz, P. J. Bruggeman, L. Couëdel, G. L. Delzanno, Y. Feng, R. Gopalakrishnan, F. Greiner, P. Hartmann, M. Horányi, H. Kersten, C. A. Knapek, U. Konopka, U. Kortshagen, E. G. Kostadinova, E. Kovačević, S. I. Krasheninnikov, I. Mann, D. Mariotti, L. S. Matthews, A. Melzer, M. Mikikian, V. Nosenko, M. Y. Pustylnik, S. Ratynskaia, R. M. Sankaran, V. Schneider, E. J. Thimsen, E. Thomas, H. M. Thomas, P. Tolias, and M. van de Kerkhof. Physics and applications of dusty plasmas: The perspectives 2023. *Physics of Plasmas*, 30(12), December 2023.

[112] Mangilal Choudhary. Perspective: Dusty plasma experiments — a learning tool for physics graduate students. *European Journal of Physics*, 42(5):053001, 2021.

[113] Robert Merlino. Dusty plasmas: from saturn's rings to semiconductor processing devices. *Advances in Physics: X*, 6(1), January 2021.

[114] E.G. Kostadinova, K. Busse, N. Ellis, J. Padgett, C.D. Liaw, L.S. Matthews, and T.W. Hyde. Delocalization in infinite disordered two-dimensional lattices of different geometry. *Physical Review B*, 96(23):235408, 2017.

[115] E.G. Kostadinova, C.D. Liaw, L.S. Matthews, and T.W. Hyde. Physical interpretation of the spectral approach to delocalization in infinite disordered systems. *Materials Research Express*, 3(12):125904, 2016.

[116] E.G. Kostadinova, F. Guyton, A. Cameron, K. Busse, C. Liaw, L.S. Matthews, and T.W. Hyde. Transport properties of disordered two-dimensional complex plasma crystal. *Contributions to Plasma Physics*, 58(2-3):209–216, 2018.

[117] M.Y. Pustylnik, M.A. Fink, V. Nosenko, T. Antonova, H.M. Hagl, H.M. Thomas, A.V. Zobnin, A.M. Lipaev, A.D. Usachev, V.I. Molotkov, O.F. Petrov, V.E. Fortov, C. Rau, C. Deysenroth, S. Albrecht, M. Kretschmer, M.H. Thoma, G.E. Morfill, R. Seurig, A. Stettner, V.A. Alyamovskaya, A. Orr, E. Kufner, E.G. Lavrenko, G.I. Padalka, E.O. Serova, A.M. Samokutyaev, and S. Christoforetti. Plasmakristall-4: New complex (dusty) plasma laboratory on board the international space station. *Review of Scientific Instruments*, 87(9):093505, 2016.

[118] V. N. Naumkin, D. I. Zhukhovitskii, A. M. Lipaev, A. V. Zobnin, A. D. Usachev, O. F. Petrov, H. M. Thomas, M. H. Thoma, O. I. Skripochka, and A. A. Ivanishin. Excitation of progressing dust ionization waves on pk-4 facility. *Physics of Plasmas*, 28(10), October 2021.

[119] D. I. Zhukhovitskii. On the controversy of dust ionization waves. *Physics of Plasmas*, 29(7):073701, 2022.

[120] M. Y. Pustylnik. Dust ionization wave analysis and response to critiques. *Physics of Plasmas*, 29(11):114701, 2022.

[121] A. Mendoza, D. Jiménez Martí, L. S. Matthews, B. Rodríguez Saenz, P. Hartmann, E. Kostadinova, M. Rosenberg, and T. W. Hyde. Ion density waves driving the formation of filamentary dust structures. *Physics of Plasmas*, 32(2):023705, 2025.

[122] J. Goree, Bin Liu, M. Y. Pustylnik, H. M. Thomas, V. E. Fortov, A. M. Lipaev, V. I. Molotkov, A. D. Usachev, O. F. Petrov, M. H. Thoma, E. Thomas, U. Konopka, and S. Prokopiev. Correlation and spectrum of dust acoustic waves in a radio-frequency plasma using *PK-4* on the international space station. *Physics of Plasmas*, 27(12), December 2020.

[123] Bin Liu, John Goree, M. Y. Pustylnik, H. M. Thomas, V. E. Fortov, A. M. Lipaev, A. D. Usachev, O. F. Petrov, A. V. Zobnin, and M. H. Thoma. Time-dependent shear motion in a strongly coupled dusty plasma in pk-4 on the international space station (*ISS*). *IEEE Transactions on Plasma Science*, 49(9):2972–2978, September 2021.

[124] Peter Hartmann, Marlene Rosenberg, Zoltan Juhasz, Lorin S. Matthews, Dustin L. Sanford, Katrina Vermillion, Jorge Carmona-Reyes, and Truell W. Hyde. Ionization waves in the pk-4 direct current neon discharge. *Plasma Sources Science and Technology*, 29(11):115014, November 2020.

[125] Katrina Vermillion, Dustin Sanford, Lorin Matthews, Peter Hartmann, Marlene Rosenberg, Evdokiya Kostadinova, Jorge Carmona-Reyes, Truell Hyde, Andrey M. Lipaev, Alexandr D. Usachev, Andrey V. Zobnin, Oleg F. Petrov, Markus H. Thoma, Mikhail Y. Pustylnik, Hubertus M. Thomas, and Alexey Ovchinin. Influence of temporal variations in plasma conditions on the electric potential near self-organized dust chains. *Physics of Plasmas*, 29(2), February 2022.

[126] Katrina Vermillion, Abbie Terrell, Emerson Gehr, Evdokiya G. Kostadinova, Peter Hartmann, Lorin S. Matthews, and Truell W. Hyde. Numerical modeling of the

plasmakristall-4 experiment on the *ISS*. In *AIAA SCITECH 2023 Forum*. American Institute of Aeronautics and Astronautics, January 2023.

[127] Johannes Schindelin, Ignacio Arganda-Carreras, Erwin Frise, Verena Kaynig, Mark Longair, Tobias Pietzsch, Stephan Preibisch, Curtis Rueden, Stephan Saalfeld, Benjamin Schmid, Jean-Yves Tinevez, Daniel James White, Volker Hartenstein, Kevin Eliceiri, Pavel Tomancak, and Albert Cardona. Fiji: an open-source platform for biological-image analysis. *Nature Methods*, 9(7):676–682, 2012.

[128] A. Shivanandan, A. Radenovic, and I. F. Sbalzarini. Mosaicia: an imagej/fiji plugin for spatial pattern and interaction analysis. *BMC Bioinformatics*, 14:349, 2013.

[129] K. Avinash, R. L. Merlino, and P. K. Shukla. Anomalous dust temperature in dusty plasma experiments. *Physics Letters A*, 375(30-31):2854–2857, July 2011.

[130] G. Livadiotis, M. I. Desai, and L. B. Wilson. Generation of Kappa Distributions in Solar Wind at 1 au. *The Astrophysical Journal*, 853(2):142, February 2018.

[131] M. P. Leubner and Z. Voros. A Nonextensive Entropy Approach to Solar Wind Intermittency. *The Astrophysical Journal*, 618(1):547–555, January 2005.

[132] Constantino Tsallis, João C. Anjos, and Ernesto P. Borges. Fluxes of cosmic rays: A delicately balanced stationary state. *Physics Letters A*, 310(5–6):372–376, 2003.

[133] L. F. Burlaga and A. F.-Viñas. Tsallis distributions of the large-scale magnetic field strength fluctuations in the solar wind from 7 to 87 au. *Journal of Geophysical Research: Space Physics*, 110(A7), July 2005.

[134] Lori S. McCabe, Jeremiah Williams, Saikat C. Thakur, Uwe Konopka, Evdokiya Kostadinova, Mikhail Y. Pustylnik, Hubertus M. Thomas, Markus H. Thoma, and Edward Thomas. Experiments and modeling of dust particle heating resulting from

changes in polarity switching in the pk-4 microgravity laboratory. *Physics of Plasmas*, 32(5):053701, 2025.

[135] P. Hartmann, M. Rosenberg, Z. Juhasz, L. S. Matthews, D. L. Sanford, K. Vermillion, J. Carmona-Reyes, and T. W. Hyde. Ionization waves in the pk-4 direct current neon discharge. *Plasma Sources Science and Technology*, 2020.

[136] Lorin S. Matthews, Truell W. Hyde, Katrina Vermillion, Dustin L. Sanford, Peter Hartmann, Marlene Rosenberg, Evdokiya G. Kostadinova, and Jorge Carmona-Reyes. Effect of ionization waves on dust chain formation in a dc discharge. *Journal of Plasma Physics*, 87(6):905870618, 2021.

[137] E. G. Kostadinova, E. Gehr, B. Andrew, L. S. Matthews, T. W. Hyde, and A. Terrell. Liquid plasma crystals on the iss. In *AIAA SCITECH 2023 Forum*, page 2615, 2023.

[138] Tiffany Frugé Jones, Evdokiya Georgieva Kostadinova, Joshua Lee Padgett, and Qin Sheng. A series representation of the discrete fractional laplace operator of arbitrary order. *Journal of Mathematical Analysis and Applications*, 504(1):125323, 2021.

[139] Evdokiya G. Kostadinova. *Spectral Approach to Transport Problems in Two-Dimensional Disordered Lattices: Physical Interpretation and Applications*. Springer Theses. Springer, Cham, 2018.

[140] E. G. Kostadinova, C. D. Liaw, A. S. Hering, A. Cameron, F. Guyton, L. S. Matthews, and T. W. Hyde. Spectral approach to transport in a two-dimensional honeycomb lattice with substitutional disorder. *Physical Review B*, 99(2):024115, 2019.

[141] P. W. Anderson. Absence of diffusion in certain random lattices. 109(5):1492–1505.

[142] J. T. Edwards and D. J. Thouless. Numerical studies of localization in disordered systems. 5(8):807.

[143] E. Abrahams, P. W. Anderson, D. C. Licciardello, and T. V. Ramakrishnan. Scaling theory of localization: Absence of quantum diffusion in two dimensions. 42(10):673–676. Publisher: American Physical Society.

[144] Fabio Sattin, N. Vianello, M. Valisa, V. Antoni, and G. Serianni. On the probability distribution function of particle density and flux at the edge of fusion devices. *Physics of Plasmas*, 11(11):5032–5036, 2003.

[145] Tobias Hauff, Frank Jenko, and Sascha Eule. Intermediate non-gaussian transport in plasma core turbulence. *Physics of Plasmas*, 14(10):102316, 2007.

[146] M. Muraglia, P. Beyer, S. Benkadda, X. Garbet, and P. H. Diamond. Non-gaussian properties of global momentum and particle fluxes in plasma turbulence. *Physics of Plasmas*, 18(7):070701, 2011.

[147] A. J. Crilly, B. D. Appelbe, O. M. Mannion, W. Taitano, E. P. Hartouni, A. S. Moore, M. Gatu-Johnson, and J. P. Chittenden. Constraints on ion velocity distributions from fusion product spectroscopy. *Nuclear Fusion*, 62(12):126015, 2022.

[148] Haozhe Kong, Huasheng Xie, Bing Liu, Muzhi Tan, Di Luo, Zhi Li, and Jizhong Sun. Enhancement of fusion reactivity under non-maxwellian distributions: effects of drift-ring-beam, slowing-down, and kappa super-thermal distributions. *Plasma Physics and Controlled Fusion*, 66(1):015009, December 2023.

[149] T. S. Goud, R. Ganesh, Y. C. Saxena, and D. Raju. Fluctuations and intermittent poloidal transport in a simple toroidal plasma. *Physics of Plasmas*, 20(7):072308, July 2013.

[150] I. M. Sokolov, A. Blumen, and J. Klafter. Charged particle dynamics in the presence of non-gaussian lévy noise. *Physical Review E*, 64(2):021107, 2001.

[151] R. Sánchez, B.A. Carreras, L. Garcia, J.A. Mier, B.Ph. vanMilligen, and D.E. Newman. Non-diffusive transport in numerical simulations of magnetically-confined turbulent plasmas. In *Chaos, Complexity and Transport*, pages 189–206. World Scientific, 2008.

[152] D. del Castillo-Negrete, B. A. Carreras, and V. E. Lynch. Nondiffusive transport in plasma turbulence: A fractional diffusion approach. *Physical Review Letters*, 94(6), February 2005.

[153] T. Gheorghiu, F. Militello, and J. Juul Rasmussen. On the transport of tracer particles in two-dimensional plasma edge turbulence. *Physics of Plasmas*, 31(1), January 2024.

[154] Martin Lemoine. Particle transport through localized interactions with sharp magnetic field bends in mhd turbulence. *Journal of Plasma Physics*, 89(5), September 2023.

[155] J. R. Myra, Peter J. Catto, H. E. Mynick, and R. E. Duvall. Quasilinear diffusion in stochastic magnetic fields: Reconciliation of drift-orbit modification calculations. 5(4):1160–1163.

[156] Konsta Särkimäki, Eero Hirvijoki, Joan Decker, Jari Varje, and Taina Kurki-Suonio. An advection–diffusion model for cross-field runaway electron transport in perturbed magnetic fields. *Plasma Physics and Controlled Fusion*, 58(12):125017, November 2016.

[157] T. E. Evans, R. K. W. Roeder, J. A. Carter, and B. I. Rapoport. Homoclinic tangles, bifurcations and edge stochasticity in diverted tokamaks. *Contributions to Plasma Physics*, 44(1–3):235–240, April 2004.

[158] T E Evans. Resonant magnetic perturbations of edge-plasmas in toroidal confinement devices. *Plasma Physics and Controlled Fusion*, 57(12):123001, November 2015.

[159] L. Bardóczi and T.E. Evans. Experimental observation of magnetic island heteroclinic bifurcation in tokamaks. *Physical Review Letters*, 126(8), February 2021.

[160] A. Wingen, T.E. Evans, and K.H. Spatschek. High resolution numerical studies of separatrix splitting due to non-axisymmetric perturbation in diii-d. *Nuclear Fusion*, 49(5):055027, April 2009.

[161] Magali Muraglia, Olivier Agullo, Nicolas Dubuit, Roméo Bigué, and Xavier Garbet. Multi-scale physics of magnetic reconnection in hot magnetized plasmas. *Journal of Plasma Physics*, 91(1), January 2025.

[162] H. T. Moges, Y. Antonenas, G. Anastassiou, Ch. Skokos, and Y. Kominis. Kinetic vs magnetic chaos in toroidal plasmas: A systematic quantitative comparison. *Physics of Plasmas*, 31(1), January 2024.

[163] W. Wu, T.E. Evans, G.P. Canal, N.M. Ferraro, B.C. Lyons, and D.M. Orlov. Topological bifurcation of magnetic islands in nstx-u. *Nuclear Fusion*, 59(6):066010, April 2019.

[164] S. C. Jardin, N. M. Ferraro, J. J. Breslau, and M. G. Ruschenburg. The M3D-C1 Project: Three-Dimensional Extended MHD Simulations with C^1 Hermite Finite Elements. *Journal of Computational Physics*, 227(3):1954–1971, 2008.

[165] T. E. Evans and R. A. Moyer. Modeling of Coupled Edge Stochastic and Core Resonant Magnetic Field Effects in Diverted Tokamaks Using TRIP3D. *General Atomics Report GA-A23986*, 2002.

[166] H. P. Furth, P. H. Rutherford, and H. Selberg. Tearing mode instabilities in plasmas. *Journal of the Physical Society of Japan*, 50(10):3124–3132, 1981.

[167] Y. Sun, R. J. Zhou, Y. F. Liang, H. Q. Wang, Y. Q. Liu, L. Zeng, C. B. Jiang, D. Hu, Y. Liu, J. Luo, L. Wang, W. Zhang, and B. N. Wan. Development of a real-time magnetic island detector using electron cyclotron emission imaging on east. *Review of Scientific Instruments*, 88(8):083510, 2017.

[168] A. Bhattacharjee, E. G. Zweibel, J. Chen, and Y. Zhou. Current sheets and magnetic island formation in plasmas. *arXiv preprint arXiv:2108.13508*, 2021.

[169] G. Matsunaga, K. Ida, S. Inagaki, Y. Kawasumi, Y. Kawai, R. Sano, A. Shimizu, M. Yamasaki, H. Yamada, and K. Y. Watanabe. Observation of magnetic island formation due to current filaments in lhd plasmas. *Plasma Physics and Controlled Fusion*, 58(4):045015, 2016.

[170] Yue Wang and Jiulin Du. The collision frequencies in the plasmas with the power-law q-distributions in nonextensive statistics. *Physics of Plasmas*, 566:125623, 2021.

Appendix A

Nonextensive Plasma Formulary

Below are a selection of proposed plasma coefficients and equations under nonextensive statistics. Note that authors may have the parameter q under an alternate definition, e.g. $q' = 2 - q$ or others. Accordingly, this chapter retains the original notations used in each cited source to preserve clarity and consistency.

Nonextensivity parameter [21, 22]:

$$1 - q = \frac{k_B \nabla T}{e\left(\nabla\phi - \frac{1}{c}\boldsymbol{u} \times \boldsymbol{B}\right)} \tag{A.0.1}$$

here q is the nonextensive entropic index, k_B is the Boltzmann constant, ∇T is the temperature gradient, e is the elementary charge, $\nabla\phi$ is the gradient of the electrostatic potential, c is the speed of light in vacuum, $\boldsymbol{u}$ is the bulk flow velocity of the particles (typically electrons), and $\boldsymbol{B}$ is the magnetic field vector. Nonextensive parameter relation extended with inertial effects [23]:

$$\left(\kappa_\alpha - \frac{3}{2}\right) k_B \nabla T_\alpha = e\left[-\nabla\varphi_c + \frac{1}{c}\boldsymbol{u} \times \boldsymbol{B}\right] - m_\alpha\left(\omega^2 \boldsymbol{R} + 2\boldsymbol{u} \times \boldsymbol{\omega}\right) \tag{A.0.2}$$

κ_α is the kappa parameter for species α, related to the nonextensive index by $\kappa = 1/(q-1)$; m_α is the particle mass of species α; ω is the angular velocity; $\boldsymbol{R}$ is the radial position vector; and $\boldsymbol{\omega}$ is the angular velocity vector, contributing to Coriolis effects. Kappa-dependent

diffusion coefficient [25]:

$$D_{i,e}^{\kappa} = \frac{2\sqrt{\pi}k_B T_{i,e}(2\kappa_{i,e}-3)}{m_e \nu_{i,e}} \cdot \frac{\Gamma(\kappa_{i,e}+1)}{\Gamma(\kappa_{i,e}-1/2)} \cdot \frac{(2\kappa_{i,e}-5)!!}{(2\kappa_{i,e})!!} \tag{A.0.3}$$

where i, e is ions or electrons respectively, ν is the collision frequency, Γ is the gamma function, and !! is the double factorial. Mobility coefficient [25]:

$$\mu_{\kappa,\alpha} = \frac{2\sqrt{\pi}Z_\alpha e(2\kappa_\alpha-3)!!\,\Gamma(\kappa_\alpha+1)}{m_\alpha \nu_\alpha (2\kappa_\alpha)!!\,\Gamma(\kappa_\alpha-1/2)} \tag{A.0.4}$$

here Z is the ion charge number. Thermal conductivity λ from q-distributions divided by normal Maxwellian ($q=1$) case [29]:

$$\frac{\lambda_{q,\alpha}}{\lambda_{1,\alpha}} = \frac{4}{(5q_\alpha-7)(7q_\alpha-9)}, \quad 0 < q_\alpha < \frac{9}{7} \tag{A.0.5}$$

Thermoelectric coefficient χ from q-distributions divided by normal Maxwellian ($q=1$) case [29]:

$$\frac{\chi_{q,\alpha}}{\chi_{1,\alpha}} = \frac{2}{7-5q_\alpha}, \quad 0 < q_\alpha < \frac{9}{7} \tag{A.0.6}$$

Thermal diffusion coefficient D from q-distributions divided by normal Maxwellian ($q=1$) case [29]:

$$\frac{D_{q,T\alpha}}{D_{1,T\alpha}} = \frac{2}{7-5q_\alpha}, \quad 0 < q_\alpha < \frac{7}{5} \tag{A.0.7}$$

Collision frequency in nonextensive plasma divided by normal Maxwellian ($q=1$) case [170]:

$$\frac{\nu_{q,ie}}{\nu_{1,ie}} = \begin{cases} \dfrac{(1-q)^{1/2}(3-q)(5-3q)\,\Gamma\left(\frac{1}{1-q}+\frac{1}{2}\right)}{4\,\Gamma\left(\frac{1}{1-q}\right)}, & 0 < q < 1 \\ \dfrac{(q-1)^{3/2}\,\Gamma\left(\frac{1}{q-1}\right)}{\Gamma\left(\frac{1}{q-1}-\frac{3}{2}\right)}, & 1 < q < \frac{5}{3} \end{cases} \tag{A.0.8}$$

Electron plasma beta β divided by normal Maxwellian ($q = 1$) case [18]:

$$\frac{\beta_{\|e}(q)}{\beta_{\|e}(M)} = \frac{2}{5q-3} \tag{A.0.9}$$

Nonextensive temperature scaling divided by normal Maxwellian ($q = 1$) case [18]:

$$\frac{T_{\|,\perp}(q)}{T_{\|,\perp}(M)} = \frac{2}{5q-3} \tag{A.0.10}$$

Whistler mode instability growth rate Ω [18]:

$$\Omega_q = \frac{\left[1 + (1-q)\,\frac{\omega_{ce}^2\left(\frac{\omega_r}{\omega_{ce}}-1\right)^2}{k_\|^2 v_{th\|}^2}\right]^{\frac{q}{q-1}} \left(\frac{\omega_{pe}^2}{\omega_r k_\| v_{th\|}} + \Lambda\,\frac{\omega_{pe}^2}{\omega_r^2}\,\frac{\omega_{ce}\left(\frac{\omega_r}{\omega_{ce}}-1\right)}{k_\| v_{th\|}}\right)}{2\,\frac{c^2 k_\|^2}{\omega_r^3}} \tag{A.0.11}$$

ω_{ce} is the electron cyclotron frequency, ω_{pe} is the electron plasma frequency, ω_r is the real part of the wave frequency, $k_\|$ is the wave number component parallel to the magnetic field, $v_{th\|}$ is the parallel electron thermal speed, and Λ is the Coulomb logarithm, accounting for the range of impact parameters in binary collisions. Whistler instability imaginary frequency [18]:

$$\frac{\omega_i}{\omega_{ce}} = \begin{cases} -\sqrt{\pi}\left(\dfrac{3q-1}{2q}\right)\dfrac{\Gamma\left(\frac{1}{1-q}+1\right)}{\left(\frac{1}{1-q}\right)^{3/2}\Gamma\left(\frac{1}{1-q}-\frac{1}{2}\right)}\Omega_q, & 3/5 < q < 1 \\ -\sqrt{\pi}(q-1)^{3/2}\left(\dfrac{3q-1}{2q}\right)\dfrac{\Gamma\left(\frac{1}{q-1}+\frac{3}{2}\right)}{\Gamma\left(\frac{1}{q-1}\right)}\Omega_q, & q > 1 \end{cases} \tag{A.0.12}$$

Modified plasma dispersion function $Z(\xi)$ with κ-distributions [31]:

$$Z_\kappa^*(\xi) = -\frac{(\kappa-1/2)\,\kappa!}{2\kappa^{3/2}\,(2\kappa)!}\sum_{\ell=0}^{\kappa}\frac{(\kappa+\ell)!}{\ell!}\,i^{\kappa-\ell}\left(\frac{2}{\left(\frac{\xi}{\sqrt{\kappa}}+i\right)}\right)^{\kappa+1-\ell} \tag{A.0.13}$$

ℓ is the summation index, i is the imaginary unit, and $\xi = (\omega_0 + i\gamma)/(kv_{th})$ is the normalized complex phase velocity, with $\omega_0 \equiv \omega_{pe}$ is the electron plasma frequency, γ the growth or

damping rate, and k the wave number Nonextensive dispersion relation for electrostatic waves [32]:

$$\omega^2 = \omega_0^2 + 3(\lambda_D k)^2 \omega_0^2 \left(\frac{2}{3q-1}\right) \tag{A.0.14}$$

Growth rate for electrostatic instability [32]:

$$\gamma_q = \omega_0 \sqrt{\frac{\pi}{8}}\, L_q \frac{1}{(k\lambda_D)^3} \times \left[1 - (q-1)\left(-\frac{1}{2(k\lambda_D)^2}\right)\right]^{\frac{2-q}{q-1}} \tag{A.0.15}$$

with Normalization function L_q:

$$L_q = \begin{cases} \dfrac{\Gamma\left(\frac{1}{1-q}\right)}{\Gamma\left(\frac{1}{q-1} - \frac{1}{2}\right)} \sqrt{1-q}, & q \leq 1 \\ \left(\dfrac{1+q}{2}\right) \dfrac{\Gamma\left(\frac{1}{2} + \frac{1}{q-1}\right)}{\Gamma\left(\frac{1}{q-1}\right)} \sqrt{q-1}, & q > 1. \end{cases} \tag{A.0.16}$$

Nonextensive dielectric function in relativistic plasmas [36]:

$$\epsilon_\ell^{(r)} = 1 + \frac{\omega_p^2}{v_{th}^2 k^2} \left(\frac{3q-1}{2}\right) \left[1 - \frac{\omega^2}{v_{th}^2 k^2} \left(\frac{1+q}{2}\right)\right] \tag{A.0.17}$$

Dispersion relation from nonextensive electron gas [36, 37]:

$$\omega^2(k) = \left(\frac{2}{q+1}\right) k^2 v_{th}^2 \left[1 + k^2 \lambda_D^2 \left(\frac{2}{3q-1}\right)\right] \tag{A.0.18}$$

Nonextensive skin-depth λ_{sk} in collisional plasma [38]:

$$\lambda_{sk} = \frac{1}{\Omega} \left[\frac{2}{-1 - \frac{2}{3q-1}\frac{V^2}{\nu^4} + \sqrt{\left(1 + \frac{2}{3q-1}\frac{V^2}{\nu^4}\right)^2 + \left(\frac{1}{\Omega\nu} - \frac{2}{3q-1}\frac{\Omega V^2}{\nu^3}\right)^2}} \right]^{1/2} \tag{A.0.19}$$

$\Omega = \omega/\omega_{pe}$ is the wave frequency normalized by the electron plasma frequency, ν is the electron–neutral collision frequency, $V = v_{Te}/c$ is the electron thermal velocity divided by the speed of light.

Appendix B

DT Resonant Wave Heating Connection to Nonextensive Statistics

A discussion about the connection between nonextensive statistics and resonant wave heating, discussed by Swanson in [1] page 58 is presented. Swanson examines the heating of a plasma at either the fundamental ion cyclotron frequency or its first harmonic via the fast Alfvén wave. This derivation starts with the Fokker-Planck equation with quasi-linear diffusion and arrives at the below distribution.

$$\ln f(v) = -\frac{E}{k_B T_e(1+\xi)}\left[1 + \frac{R_j(T_e - T_j + \xi T_e)}{T_j(1+R_j+\xi)} H(E/E_j)\right] \tag{B.0.1}$$

where

$$\begin{aligned}
E &\equiv \frac{1}{2}mv^2, \quad \ell_j \equiv \frac{1}{v_{tj}}, \quad R_j \equiv \frac{n_j Z_j^2 \ell_j}{n_e \ell_e} \\
E_j(\xi) &\equiv v_{tj}\left[\frac{1+R_j+\xi}{2\epsilon(1+\xi)}\right]^{2/3} \leq E_j(0), \quad E_j(0) \equiv \frac{1}{2}mV_B^2 \\
H(x) &\equiv \frac{1}{x}\int_0^x \frac{du}{1+u^{3/2}} \\
&= \frac{2}{x}\left[\frac{1}{6}\ln\left(\frac{1-\sqrt{x}+x}{1+2\sqrt{x}+x}\right) + \frac{1}{\sqrt{3}}\left(\frac{\pi}{2} + \tan^{-1}\frac{2\sqrt{x}-1}{\sqrt{3}}\right)\right] \\
&\simeq 1 - \frac{2}{5}x^{3/2} + \frac{1}{4}x^3 - \frac{2}{11}x^{9/2} + \cdots, \quad |x| \ll 1 \\
&\simeq 2.4184x^{-1} - 2x^{-3/2} + \frac{1}{2}x^{-3} - \frac{2}{7}x^{-9/2} + \cdots, \quad |x| \gg 1
\end{aligned}$$

where the specific case of $n_T = 5 \cdot 10^{19}$ m^{-3}, $n_D = n_T/20$, $k_B T_e = k_B T_T = 4$ keV is used for the plot in Figure B.1 a).

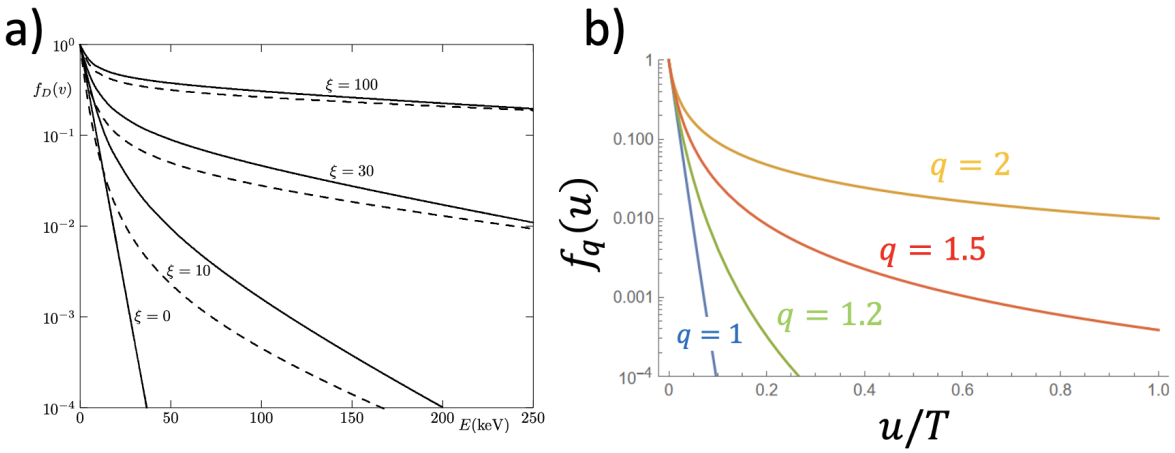

Figure B.1: (a) Figure 3.6 pg. 66 from [1] showing energy E (keV) distribution function with modifiable parameters ξ copied with permission. Solid lines are for $f_D(v)$ and dashed lines for $f_D(v_\perp)$. (b) q-energy distribution with energy normalized by temperature T and q values $1, 1.2, 1.5, 2$.

The dimensionless parameter ξ quantifies the strength of velocity-space diffusion and energy exchange in plasmas undergoing external power deposition. It is defined as

$$\xi \equiv \frac{2K}{\varepsilon C_e \ell_e} = \frac{2\pi^{3/2}\varepsilon_0^2 m\langle P\rangle v_{te}}{n_e n Z^2 e^4 \ln\Lambda}, \tag{B.0.2}$$

where $\langle P\rangle$ is the average power transferred to the electrons, v_{te} is the electron thermal speed, and $\ln\Lambda$ is the Coulomb logarithm. As shown in Figure B.1 a), increasing ξ enhances the deviation from a Maxwellian distribution, resulting in a power-law tail. In RF-heated plasmas, ξ acts as a control parameter for wave-particle interactions, particularly near the two-ion hybrid resonance, where it determines the extent of energy deposition and mode conversion. For instance, a transition to significant electron heating occurs near $\xi \approx 45$, as the resonance layer facilitates strong mode conversion and suppresses reflection. In essence, ξ captures how effective energy and momentum transfer via collisions is relative to the characteristic electron transport scales in the plasma. A larger ξ indicates stronger collisional effects or enhanced scattering due to plasma parameters (like higher density or energy exchange), while a small

ξ suggests near collisionless behavior. This is also what the parameter q does in the far simpler expression:

$$f_q(u) = A_q \left[1 - (1-q)\frac{u}{k_B T_q}\right]^{\frac{1}{1-q}}. \tag{B.0.3}$$

The exact relation between ξ and q is currently not known but, as can be seen in Figure B.1 b), the resulting energy distribution can be the same. While the energy distribution found for Figure B.1 a) is known, it required a lot of effort to reach the same solution, which can be done by starting with a collisional plasma based distribution Eq. B.0.3. While a graphical comparative mapping of the relation between ξ and q could be done, a theoretical derivation of how q depends on physical parameters and how it deviates or is similar to ξ would be very beneficial.

Appendix C

FLSM Code Suite Overview

Overview

To run all three major parameter combinations (s, c, ν) of the FLSM model across a 3D parameter space with several trials, averaged over instances of randomization, and after sufficiently long time-steps for asymptotic behavior to the following code suit using SLURM, Python, and MATLAB was used.

Parameter Grid Generation

First, Python is used to generate all combinations and create a CSV file and metadata text file:

```
import numpy as np
import itertools
import pandas as pd
import os, time

ss_list = np.round(np.arange(0.4, 1.26, 0.01), 4)
c_list = np.round(np.arange(0.0001, 0.0101, 0.001), 5)
ref_list = [50, 150]

combinations = list(itertools.product(ss_list, c_list, ref_list))
df = pd.DataFrame(combinations, columns=["s", "c", "reference"])

# Create timestamped job folder
folder_name = f"job_{time.strftime('%Y_%m_%d_%H%M%S')}"
```

```
output_dir = f"results/{folder_name}"
os.makedirs(output_dir, exist_ok=True)

df.to_csv(f"{output_dir}/params_grid.csv", index=False)
with open(f"{output_dir}/num_combinations.txt", "w") as f:
    f.write(str(len(df)))
```

SLURM Master Script (FLSM_Master.sh)

The SLURM master script dynamically detects the latest job folder and launches a job array over all parameter combinations:

```
#!/bin/bash
#SBATCH --job-name=FLSM_array
#SBATCH --partition=bigmem2,gpu2
#SBATCH --ntasks=1
#SBATCH --cpus-per-task=12
#SBATCH --mem=64G
#SBATCH --time=20-00:00:00
#SBATCH --output=results/%x_%A_%a.out
#SBATCH --error=results/%x_%A_%a.err

LATEST_JOB_FOLDER=$(ls -td results/job_* | head -1 | xargs basename)
export JOB_FOLDER="$LATEST_JOB_FOLDER"
NUM_COMBINATIONS=$(cat "results/$JOB_FOLDER/num_combinations.txt")

if [ -z "$SLURM_ARRAY_TASK_ID" ]; then
    sbatch --array=0-$(($NUM_COMBINATIONS - 1)) $0
    exit 0
fi

LINE=$(($SLURM_ARRAY_TASK_ID + 2))
```

```
PARAMS=$(sed -n "${LINE}p" results/$JOB_FOLDER/params_grid.csv | tr -d '\r
    \n')
IFS=',' read -r s_val c_val ref_val <<< "$PARAMS"

module load matlab/2022a
matlab -batch "run_FLSM(${s_val}, ${c_val}, ${ref_val}, '${JOB_FOLDER}')"
```

MATLAB Function Execution (run_FLSM.m)

This script is called with the individual parameters and:

- Logs start/end status to `progress.log`
- Calls `compute_FLSM.m, which is the primary script for calculating 2.4.6`
- Saves the result as `YY_s__c__r.mat in the job folder`

```
function run_FLSM(s, c, ref, job_folder)
    if isempty(gcp('nocreate'))
        parpool('local', 12);
    end

    [YY, Z] = compute_FLSM(s, 8000, c, 75, ref, 8);
    filename = sprintf('YY_s%.2f_c%.4f_r%d.mat', s, c, ref);
    save(fullfile('results', job_folder, filename), 'YY', 'Z');

    log_path = fullfile('results', job_folder, 'progress.log');
    fid = fopen(log_path, 'a');
    fprintf(fid, '[%s] Completed s=%.2f, c=%.4f, ref=%d\n', ...
        datestr(now), s, c, ref);
    fclose(fid);
end
```

Postprocessing

Each job folder contains:

- `params_grid.csv`
- `num_combinations.txt`
- `progress.log`
- Result files: `YY_s__c__r.mat`

This calculation can be done for up to 5,000 combinations and takes roughly one day on the Auburn University Easley Cluster. Afterwards, these are visualized using dynamic MATLAB plotting scripts that create parameter slices and contour plots over (s, c), (c, ν), or (s, ν). This large scale computational speed up to find the probability of transport at the last time-step for 55,000 parameter combinations between the fractional Laplacian nonlocality parameter s, the disorder of the system c, and the reference scale in Hilbert-space ν resulted in major progress for understanding 2.4.6, which was presented in chapter 5.

Appendix D

Ideal MHD Equations Derivation

A short derivation of Eq. is given. We will use the notation of $\hat{\phi}$ for the toroidal direction, $\hat{\theta}$ for the poloidal direction, and $\hat{r}$ for the radial direction located at the center of the circular poloidal cross section. This is shown in Figure D.1.

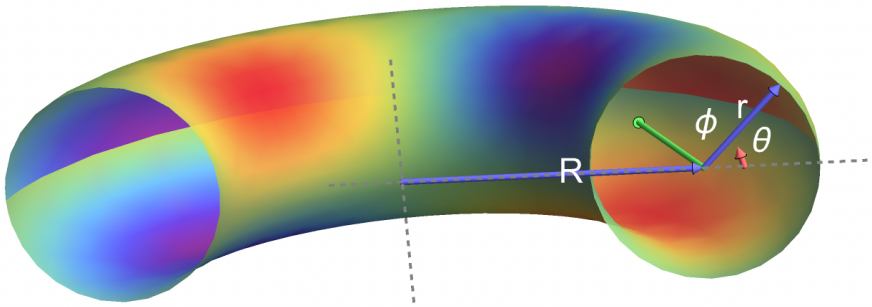

Figure D.1: Torus geometry showing the direction components. The changing colored surface is to help visualize toroidal and poloidal angles.

Consider the force balance in the $\hat{R}$ direction.

$$J_\phi B_Z - J_Z B_\phi = \frac{\partial P}{\partial R} \tag{D.0.1}$$

Using the following expressions for the magnetic field and current density:

$$\mathbf{B} = \frac{1}{R}\nabla\Psi \times \hat{\phi} + \frac{g(\Psi)}{R}\hat{\phi}, \qquad \mathbf{J} = \frac{1}{\mu_0}\nabla \times \mathbf{B}, \tag{D.0.2}$$

and substituting the following:

$$B_Z = \frac{1}{R}\frac{\partial \Psi}{\partial R}, \qquad g = RB_\phi, \qquad J_Z = \frac{1}{\mu_0 R}\frac{\partial g}{\partial R}. \tag{D.0.3}$$

where B_ϕ, B_Z, and J_Z are functions of (R, Z), we arrive at

$$J_\phi \frac{1}{R}\frac{\partial \Psi}{\partial R} - \frac{1}{\mu_0 R}\frac{\partial g}{\partial R}\cdot\frac{g}{R} = \frac{\partial P}{\partial R}. \tag{D.0.4}$$

Assuming the $P = P(\Psi)$ and $g = g(\Psi)$, Equation D.0.1 becomes:

$$J_\phi \frac{1}{R}\frac{\partial \Psi}{\partial R} - \frac{1}{\mu_0 R}\frac{dg}{d\Psi}\frac{\partial \Psi}{\partial R}\cdot\frac{g}{R} = \frac{dP}{d\Psi}\frac{\partial \Psi}{\partial R}. \tag{D.0.5}$$

which can be simplified to

$$J_\phi = R\frac{dP}{d\Psi} + \frac{1}{\mu_0 R}\frac{dg}{d\Psi}g, \tag{D.0.6}$$

which is the requirement of force balance along the major radius. Ampère's law indicates the toroidal current density J_ϕ is given by

$$\mu_0 J_\phi = \frac{\partial B_R}{\partial Z} - \frac{\partial B_Z}{\partial R} = -\frac{1}{R}\frac{\partial^2 \Psi}{\partial Z^2} - \frac{\partial}{\partial R}\left(\frac{1}{R}\frac{\partial \Psi}{\partial R}\right) \tag{D.0.7}$$

Where we have used the fact that

$$B_R = -\frac{1}{R}\frac{\partial \Psi}{\partial Z}, B_Z = \frac{1}{R}\frac{\partial \Psi}{\partial R}. \tag{D.0.8}$$

Define Δ^* by

$$\Delta^* \equiv \frac{\partial^2}{\partial Z^2} + R\frac{\partial}{\partial R}\left(\frac{1}{R}\frac{\partial}{\partial R}\right), \tag{D.0.9}$$

then Equation D.0.7 is written as

$$J_\phi = -\frac{1}{\mu_0 R}\Delta^* \Psi. \tag{D.0.10}$$

Which with a Green's function integration gives Eq. 6.4.2. We can also arrive at the Grad-Shafranov equation by combining equation D.0.10 with equation D.0.6 yielding

$$\frac{\partial^2 \Psi}{\partial Z^2} + R\frac{\partial}{\partial R}\left(\frac{1}{R}\frac{\partial \Psi}{\partial R}\right) = -\mu_0 R^2 \frac{dP}{d\Psi} - \frac{dg}{d\Psi}g. \tag{D.0.11}$$